

ABSTRACT

HARRIS, JOSHUA SIMON. Point Defects in AlN and Al-rich AlGaN from First Principles. (Under the direction of Douglas L. Irving.)

Point defects and defect complexes in AlN and Al-rich AlGaN have been investigated using *ab initio* density functional theory (DFT) in three separate but related projects. First, oxygen and silicon defects in $\text{Al}_{0.65}\text{Ga}_{0.35}\text{N}$ were examined using explicit random alloy simulations. The O_{N}^{-1} acceptor was found to relax into one of many DX configurations, with formation energies strongly dependent on local chemistry. Trends in the formation energies were identified and explained with simple arguments involving cation-oxygen bonds. O_{N}^{+1} and $\text{Si}_{\text{III}}^{+1}$ were found to relax into on-site configurations with little variation in formation energies. Second, DFT simulations were used to explain the experimentally observed “compensation knee” in Si-doped AlN (whereby the Si donor becomes an acceptor at high doping levels). $V_{\text{Al}} + n\text{Si}_{\text{Al}}$ complexes were demonstrated to be the key to a mechanistic understanding of the compensation knee. Using a Grand Canonical charge balance solver, the compensation knee was qualitatively reproduced from the results of DFT simulations. Additionally, a shift in optical emissions was predicted for the high and low doping limits, which was confirmed by photoluminescence measurements. Finally, phonon and thermal strain simulations were used to investigate the temperature-dependent properties of bulk AlN and common point defects in AlN (Si, O, C, and vacancies). A number of general trends were identified in finite-temperature properties which are common to all or many of the defects under study. It was demonstrated that finite-temperature effects can have an impact on defect formation energies and transition levels, depending on the defect and the temperature range of interest.

© Copyright 2019 by Joshua Simon Harris

All Rights Reserved

Point Defects in AlN and Al-rich AlGaN from First Principles

by
Joshua Simon Harris

A dissertation submitted to the Graduate Faculty of
North Carolina State University
in partial fulfillment of the
requirements for the degree of
Doctor of Philosophy

Materials Science & Engineering

Raleigh, North Carolina

2019

APPROVED BY:

Ramón Collazo

Elizabeth Dickey

Lubos Mitas

Douglas L. Irving
Chair of Advisory Committee

DEDICATION

To my parents,
who have always supported me in every way imaginable.

To Ashley and Luke,
whose love inspires and comforts me every day.

I love you all.

BIOGRAPHY

Josh Harris was born in Greensboro, North Carolina. He moved to Raleigh in 2005 to pursue a B.S. in Materials Science and Engineering (2009), a B.A. in English (2010), and a minor in Physics (2009) at North Carolina State University. After graduation, he continued to take courses in the undergraduate Physics curriculum, completed a novel (*Lemnos*) which is now for sale on Amazon, and began work translating Dante's *Inferno* into English *terza rima*. In 2011, he began the graduate program in Materials Science and Engineering at NCSU, and joined Professor Doug Irving's group. Since then, he has fervently pursued his research goals, maintained a keen interest in theoretical physics and materials science, and continued work on his translations when time avails. He met Ashley Bartlett, the woman who would become his wife, in 2014. They had a son, Luke, in 2016.

ACKNOWLEDGEMENTS

This work would not have been possible without the support of my advisor, my group members, my collaborators, my friends, and my family. Nor would I have survived graduate school without the staff in the MSE Department and the generous financial support from my funding sources.

First of all, I thank Professor Doug Irving for the endless advice and encouragement he has given me over the years. My thanks also go out to my group members, past and present, including Ben Gaddy, Carissa Lada, Changning Niu, Xiaoyin Ji, Jonathon Baker, Preston Bowes, Kelsey Mirrielees, Yifeng Wu, and Justin Taylor. My work has benefited immeasurably from their guidance, the tools many of them have developed, my conversations with them, and most importantly their friendship.

I have also benefited from close collaborations with Professors Ramón Collazo, Zlatko Sitar, and Jim LeBeau at NCSU; and their students Pramod Reddy, Zachary Bryan, Isaac Bryan, Dorian Alden, Houston Dycus, and Tim Eldred. I am grateful to have worked with such amazing people, and I think we have produced impactful work together. There are many other graduate students and professors at NCSU whom I have befriended, and who have taken so much of their own time to discuss my work and assist me in various ways. Thank you all.

I also want to acknowledge the staff in the Materials Science Department, who work so hard to make our lives as graduate students easier. I especially thank Edna Deas for always going above and beyond to help me with all sorts of issues throughout my undergraduate and graduate careers. Edna has never turned me away, even when I have come to her with small personal problems, and she always takes the time to listen and help, despite her busy schedule. She really is the glue holding the whole department together, and I'm not sure I would have made it this far without her.

My research has been funded at various times by the NCSU MSE Department, the National Science Foundation (NSF), the Air Force Office of Scientific Research (AFOSR), and the NCSU Graduate School's Dissertation Completion Grant. Computer time has been provided by the NCSU High Performance Computing (HPC) Center, the National Energy Research Scientific Computing (NERSC) Center, and the Department of Defense's High Performance Computing Modernization Program (HPCMP). I thank all of these generous organizations for making my work possible.

I thank everyone who read drafts of my dissertation, in whole or in part: Professor Doug Irving, Jonathon Baker, Preston Bowes, Kelsey Mirrielees, Yifeng Wu, and my committee members. Their edits and comments have tremendously improved my work.

I thank my committee members, Ramón Collazo, Elizabeth Dickey, Lubos Mitas and Douglas Irving, for agreeing to assess my graduate work, for generously taking time from their busy lives to read my thesis and listen to my presentations, and for providing valuable feedback and insight into my projects.

Finally, I thank my friends and family for their endless encouragement, support, and understanding throughout my graduate career and beyond. I especially thank my wife Ashley and my son Luke. None of this matters without the love of family and friends.

TABLE OF CONTENTS

LIST OF TABLES	viii
LIST OF FIGURES	x
Chapter 1 Introduction	1
Chapter 2 Literature Review	6
2.1 Si Doping in GaN and Ga-rich AlGaN	6
2.2 Si Doping in AlN and Al-rich AlGaN	8
2.3 Oxygen DX Transition in Al-rich AlGaN	11
Chapter 3 Methodology	13
3.1 Density Functional Theory	13
3.2 Point Defect Concentrations from Formation Energies	16
3.3 Point Defects in DFT	18
3.4 Random Alloys in Periodic DFT	20
3.5 Phonon Calculations	21
3.6 Temperature-dependent Defect Formation Energies	25
3.7 Defect Solver	27
3.8 Semi-automated Simulation Setup Tool	29
3.8.1 The poscar Module	29
3.8.2 The potcar Module	34
3.8.3 The kpoints Module	35
3.8.4 The incar Module	37
3.8.5 The system Module	39
3.8.6 Using the SSST for Defect Simulations	41
Chapter 4 Oxygen and Silicon Point Defects in Al_{0.65}Ga_{0.35}N	43
4.1 Introduction	44
4.1.1 Oxygen Defects in AlGaN	45
4.1.2 Silicon Defects in AlGaN	46
4.1.3 Overview	46
4.2 Methods	47
4.2.1 Computational Details	47
4.2.2 Defect Geometries in Al _{0.65} Ga _{0.35} N	49
4.3 Results and Discussion	51
4.3.1 Bulk Al _{0.65} Ga _{0.35} N Simulations	51
4.3.2 Oxygen in Al _{0.65} Ga _{0.35} N	52
4.3.3 Silicon in Al _{0.65} Ga _{0.35} N	60
4.4 Conclusion	63

4.5	Acknowledgements	64
Chapter 5	On Compensation in Si-doped AlN	65
Chapter 6	Finite-Temperature Point Defect Properties in AlN from First Principles	76
6.1	Introduction	77
6.1.1	Defect Formation Energies	78
6.1.2	Phonons in the Harmonic Approximation	80
6.1.3	Thermodynamics of Phonons	81
6.1.4	Connection to Defect Formation Energies	84
6.2	Methodology	85
6.2.1	Details of DFT Calculations	85
6.2.2	Thermal Strain Approximations	87
6.2.3	Temperature Dependence of Band Edges	87
6.3	Results and Discussion	91
6.3.1	Phonons and Thermodynamic Properties of Bulk AlN	91
6.3.2	Defect Formation Energies: Impurities	97
6.3.3	Defect Formation Energies: Vacancies	108
6.3.4	Defect Formation Energies: General Trends	115
6.4	Conclusions	116
6.5	Acknowledgements	117
Chapter 7	Conclusions and Future Work	119
BIBLIOGRAPHY		122
APPENDIX		132
Appendix A	Supplemental Material	133
A.1	Supplement for Chapter 5	133

LIST OF TABLES

Table 3.1	Variables of the <code>PoscarData</code> class. These variables constitute an abstract representation of a VASP POSCAR file.	30
Table 3.2	Methods of the <code>PoscarData</code> class. These functions are used to modify or analyze the information contained in a POSCAR file. Function inputs other than <code>self</code> are listed beneath each function, along with the variable type and a short description.	31
Table 3.3	Variables of the <code>PotcarData</code> class. These variables constitute an abstract representation of the header of a VASP POTCAR file.	34
Table 3.4	Variables of the <code>KpointsData</code> class. These variables constitute an abstract representation of the header of a VASP KPOINTS file.	36
Table 3.5	Methods of the <code>SystemData</code> class. These functions are used to modify or analyze the information contained in multiple VASP input files at once. Function inputs other than <code>self</code> are listed beneath each function, along with the variable type and a short description.	40
Table 4.1	Calculated bulk lattice parameters and bond lengths in GaN, AlN, and $\text{Al}_{0.65}\text{Ga}_{0.35}\text{N}$. Bond lengths are averaged over a 96-atom cell, which results in standard deviations smaller than 0.01 Å in all cases.	51
Table 4.2	O_N^{-1} formation energies for all SCs and FCs, relative to the most stable O_N^{-1} defect. Only the lowest formation energy is reported for locally degenerate configurations.	55
Table 4.3	Nearest-neighbor bond lengths for the most stable O_N^{-1} defect in AlN and in each SC in $\text{Al}_{0.65}\text{Ga}_{0.35}\text{N}$. All defects are in the DX-a configuration, and the three bond lengths in each case are the distances to the face-coordinated cations (ordered from shortest to longest, going down each column). Highlighted cells correspond to Al-O bonds, while the rest correspond to Ga-O bonds.	57
Table 4.4	Relative formation energies and DX transition levels for the most stable defect configuration in each SC. Formation energies are reported relative to the defect with the lowest formation energy. As in Figure 4.1, light gray and dark gray spheres represent Al and Ga sites, respectively; blue spheres represent nitrogen sites; and the red sphere represents a N-substitutional defect.	58
Table 4.5	Relative site density and O_N^{-1} occupation probability for nitrogen sites in $\text{Al}_{0.65}\text{Ga}_{0.35}\text{N}$ with different <i>site coordination</i> . Non-degenerate defect configurations have been taken into account in the calculation of the site occupancies. Thermodynamic transition levels corresponding to Table 4.4 have been reproduced here for easy reference.	59

Table 5.1	Calculated optical signatures and concentrations for all optically relevant defects in the low and high [Si] doping regimes (corresponding to the red circles in Figure 5.2). The predicted shift in defect populations corresponds to a shift in predicted emission energies which closely matches experiment.	73
Table 6.1	Phonon frequencies in cm^{-1} at $\mathbf{q} = \Gamma$ in bulk AlN, compared with recent theoretical predictions[Fu15] and experimental measurements[Bic05] from the literature.	92
Table A.1	List of simulated defects, the number of unique configurations simulated (does not include degenerate configurations), and the range of charge states simulated for the study in Chapter 5. The subscript indicates the site on which the defect substitutes, and the suffix -DX appearing in the subscript indicates an off-site (DX) configuration. . .	134

LIST OF FIGURES

Figure 2.1	Electron concentration versus silane flow in $\text{Al}_x\text{Ga}_{1-x}\text{N}$ films with various Al compositions (as labeled). Reproduced from <i>Solid-State Electronics</i> 42 , 4 (1998), with the permission of Elsevier.[Pol98] ©1998 Elsevier.	8
Figure 2.2	Carrier concentration and mobility of Si-doped $\text{Al}_{0.65}\text{Ga}_{0.35}\text{N}$ at room temperature as a function of Si concentration. Reproduced from <i>Japanese Journal of Applied Physics</i> 50 , 095502 (2011), with the permission of the Japan Society of Applied Physics.[Shi11] ©2011 The Japan Society of Applied Physics.	10
Figure 4.1	Nitrogen-substitutional defect configurations in AlGa _N . Light gray and dark gray spheres represent Al and Ga sites, respectively; blue spheres represent nitrogen sites; and the red sphere represents a N-substitutional defect.	50
Figure 4.2	Formation energy diagram for O_N in $\text{Al}_{0.65}\text{Ga}_{0.35}\text{N}$. Each of the different colors represents a unique <i>site coordination</i> , as labeled in the inset. All configurations of O_N^{-1} are represented on the plot. The Fermi level has been extended above bandgap (5.09 eV, marked by a vertical dashed line) to the bandgap of AlN (6.1 eV), for illustrative purposes. The markers in the inset indicate $\text{O}_\text{N}(+ -)$ transition levels associated with different O_N^{-1} configurations in each SC.	52
Figure 4.3	Formation energy diagram for Si_III , a silicon substitutional on a cation site, in $\text{Al}_{0.65}\text{Ga}_{0.35}\text{N}$. Each line corresponds to data from a simulation in a unique bulk environment (cation configuration). The Fermi level has been extended above bandgap (5.09 eV, marked by a vertical dashed line) to the bandgap of AlN (6.1 eV), for illustrative purposes.	61
Figure 5.1	Formation energy versus Fermi level for V_Al , Si_Al , and all geometrically inequivalent configurations of $\text{V}_\text{Al} + n\text{Si}_\text{Al}$ complexes.	68
Figure 5.2	Representative room temperature plot of n versus [Si]. The two red circles indicate points at which concentration profiles are reported in Table 5.1.	70
Figure 5.3	Formation energy versus Fermi level for V_Al , Si_Al , and most favorable configurations of $\text{V}_\text{Al} + n\text{Si}_\text{Al}$ complexes. The dotted lines and solid lines correspond to the low and high [Si] sides of the compensation knee, respectively.	71
Figure 5.4	Room temperature PL spectra for samples with [Si] at 2×10^{18} and $2 \times 10^{19} \text{ cm}^{-3}$ (below and above the compensation knee, respectively). Normalized by maximum intensity.	74

Figure 6.1	Calculated phonon density of states for AlN.	93
Figure 6.2	Enthalpy, entropy and Gibbs free energy of AlN as predicted from phonon calculations (solid curves), with experimental data from JANAF tables[CJ86] superimposed (points). The enthalpy has been set to zero at absolute zero.	93
Figure 6.3	Molar heat capacity of AlN at constant volume (C_v) as predicted from phonon calculations (solid curve), with experimental data at constant pressure (C_p) taken from JANAF tables[CJ86] superimposed (points). The dashed curve represents the phonon heat capacity plus the approximate heat capacity due to thermal strain.	94
Figure 6.4	Fermi levels corresponding to DX transitions for Si_{Al} and O_{N} , and TTLs for C_{N} , in AlN. Band edges are plotted as dotted lines. The smooth curves represent phonon contributions only, while the discrete states at 300 K and 1400 K include phonon and thermal strain contributions. The notches at 0 K represent the transition levels without ZPR. All energies are defined relative to the calculated VBM without ZPR, which we have set to 0 eV.	98
Figure 6.5	Formation energy diagrams for Si_{Al} in the vicinity of the CBM at different temperatures with (a) phonon contributions only and (b) phonon and thermal strain contributions. Vertical dashed lines correspond to the CBM at finite temperatures. Dash-dotted and dotted lines correspond to the DX-a and DX-Nc acceptor states, respectively.	100
Figure 6.6	Formation energy diagrams for O_{N} in the vicinity of the CBM at different temperatures with (a) phonon contributions only and (b) phonon and thermal strain contributions. Vertical dashed lines correspond to the CBM at finite temperatures. Dash-dotted lines correspond to the DX-a acceptor state.	103
Figure 6.7	Formation energy diagrams for C_{N} in the vicinity of the VBM at different temperatures with (a) phonon contributions only and (b) phonon and thermal strain contributions. Vertical dashed lines correspond to the VBM at finite temperatures.	106
Figure 6.8	Fermi levels corresponding to TTLs for native vacancies (v_{Al} and v_{N}) in AlN. Band edges are plotted as dotted lines. The smooth curves represent phonon contributions only, while the discrete states at 300 K and 1400 K include phonon and thermal strain contributions. The notches at 0 K represent the transition levels without ZPR. All energies are defined relative to the calculated VBM without ZPR, which we have set to 0 eV.	109

Figure 6.9	Formation energy diagrams for v_{Al} at different temperatures with (a) phonon contributions only and (b) phonon and thermal strain contributions. Vertical dashed lines correspond to the VBM and CBM at finite temperatures.	110
Figure 6.10	Formation energy diagrams for v_N at different temperatures with (a) phonon contributions only and (b) phonon and thermal strain contributions. Vertical dashed lines correspond to the VBM and CBM at finite temperatures.	113

CHAPTER

1

INTRODUCTION

Aluminum nitride (AlN) and aluminum gallium nitride (AlGaN) are important next-generation materials for high-power electronics and deep ultraviolet light sources (light emitting diodes and laser diodes).[Jon15; Xie13; Gra11c] Al-rich AlGaN is of particular interest because it can be grown on native AlN substrates with close lattice matching, which enables the growth of films with low dislocation density relative to AlGaN films on foreign substrates.[Dal11; Bic10] The realization of AlGaN devices with desirable optical and electronic properties requires strict control over doping in a wide range of doping regimes, as well as an understanding of the microscopic origin of these properties.

In a semiconductor, optical and electronic properties are mostly determined by the populations of point defects in the material. Point defects are local irregularities in the crystal structure with limited spatial extent in any dimension (e.g. a missing host atom, or a host atom which has been replaced by an atom of a different element). Point defects control electronic properties by introducing electronic states inside the bandgap, thereby modifying the energy required to promote electrons into the conduction band or holes into the valence band. Because electronic transitions to and from these defect states are

accompanied by optical emissions and absorptions, point defects can have a significant impact on optical properties as well. Control over the population of point defects introduced during doping, as well as an understanding of how a given population of point defects will influence the properties, is therefore crucial to controlling the properties of a material.

However, individual point defects can be very challenging to study experimentally. Depending on purity control, dozens or even hundreds of distinct types of point defect may exist in a given material; it is thermodynamically impossible to engineer a material with no point defects at all. To characterize the properties of a single type of point defect among all of those present takes many carefully designed experiments. Even then, some defects may be difficult to isolate from others, which introduces ambiguity into the assignment of a particular property (such as a photoluminescence band) to a particular defect.

These experimental difficulties, however, are exactly the strengths of simulation. With simulation, it is easy to isolate point defects: we simply simulate an otherwise pristine bulk with a single defect in the lattice. Simulation can be used to compute individual defect properties such as defect formation energies, optical emissions and absorptions, symmetries, multiple configurations, vibrational spectra, and more. Formation energies can even be used in post-processing to predict defect and carrier populations in a given set of doping conditions.

The goal of this dissertation is to further the understanding of point defects in AlN and Al-rich AlGa_N using state-of-the-art density functional theory (DFT) simulations of native and impurity point defects and defect complexes. This work is best interpreted as a complement to experiment; the ideal path to an understanding of physical phenomena and the mechanisms behind them involves a close collaboration between theory and experiment, in which information flows both ways. In addition to a literature review and a discussion of methodology, this dissertation will feature the results of three investigations involving point defects in AlN and Al-rich AlGa_N. The author has primary authorship on each of these three investigations, two of which are already published at the time of this writing (the third is being prepared for submission). [Har18; Har19] The author has also played important roles in a number of additional investigations, for which he has been listed as an author in other publications. [Sac15; Bak17; Tia17; Dyc15; Bow18a; Ald18; Bak18b; Bak19] Here, the contents of the subsequent chapters will be briefly outlined.

In Chapter 2, I will briefly review some of the literature on some of these point defects, with an emphasis on providing some of the background necessary for later chapters. The

literature review is meant to be supplemental rather than comprehensive. More detailed review of the relevant literature is provided in each chapter.

In Chapter 3, I will discuss methodology from a general perspective, including some topics which are useful to understand but which don't have a proper place in the subsequent chapters. This chapter is designed to initiate readers with the methods, not to provide detailed information such as simulation parameters. More detail-oriented methodologies particular to each chapter are included in the chapters themselves.

Each of Chapters 4-6 detail one of the three investigations which are the focus of this dissertation.

In Chapter 4 (originally published in *Physical Review Materials*), oxygen and silicon point defects in $\text{Al}_{0.65}\text{Ga}_{0.35}\text{N}$ are discussed.[Har19] In this study, the formation energies of O_{N} and Si_{Al} are computed in pseudorandom alloy simulations using hybrid exchange-correlation DFT, to examine the influence of local chemistry fluctuations on defect formation energies. Both O_{N} and Si_{Al} were initialized in on-site substitutional and off-site DX configurations in different charge states. As in the end-members AlN and GaN, the O_{N}^{+1} donor always relaxed into an on-site configuration, and its formation energy had little dependence on local chemistry. However, the O_{N}^{-1} acceptor almost always relaxed into a DX configuration, and its formation energy was strongly dependent on the configuration of first-nearest neighbor Al or Ga atoms around the N site. Two qualitative bonding trends were identified. These can best be understood by considering the cation-O bonds in the DX configuration versus an on-site configuration. In an on-site configuration, O_{N} is tetrahedrally coordinated to four cation sites (site coordination, SC); in the DX configuration, the oxygen atom moves closer to one of the faces of the coordination tetrahedron (face coordination, FC), strengthening three bonds at the expense of breaking the remaining one. The two bonding trends are: (1) In a given SC, O_{N}^{-1} prefers to maximize the number of Al atoms in its FC; (2) in a given FC, O_{N}^{-1} prefers to reduce the number of Al atoms in its initial SC. The two trends are understood by considering that the Al-O bond is much stronger than the Ga-O bond. In addition to these two trends, the lengths of Al-O bonds have a subtle influence on the stability of a given configuration. Second and higher-order nearest neighbors have a much less significant impact on the formation energies of distinct O_{N}^{-1} DX configurations. By contrast, Si_{III} was also examined. Only $\text{Si}_{\text{III}}^{+1}$ was found to be stable inside the bandgap at the alloy composition studied. Its formation energy was found to have little dependence on the composition of nearby cations, which is explained by the fact that its nearest neighbors are N atoms.

Therefore the trends in the energetics of O_N and Si_{III} in $Al_{0.65}Ga_{0.35}N$ are both determined by the chemistry of the four nearest-neighbor sites surrounding the defect site.

In Chapter 5 (originally published in *Physical Review Materials*), compensation in Si-doped AlN is discussed.[Har18] At low concentrations, Si behaves as an n-type donor in AlN, so that the free electron concentration increases proportionally to the Si concentration. However, with increasing Si concentration, this trend eventually reverses, so that further increasing the Si concentration actually reduces the free electron concentration; this is commonly called the compensation knee. The study in this chapter provides a mechanistic understanding of the compensation knee using hybrid exchange-correlation DFT simulations of a large variety of point defects and complexes in AlN. It is demonstrated that $V_{Al} + nSi_{Al}$ complexes are key to explaining the compensation knee. As Si doping levels are increased, so does the Si chemical potential, thereby reducing the formation energies of Si-containing defects. But in response to the changing Si chemical potential, the formation energies of $V_{Al} + nSi_{Al}$ complexes changes proportionally to the number of Si atoms in the complex. This means that increasing Si chemical potential stabilizes $V_{Al} + nSi_{Al}$ for $n > 1$ more rapidly than the Si_{Al}^{+1} donor. For Fermi levels near the conduction band minimum, $V_{Al} + nSi_{Al}$ complexes either neutral ($n = 3$) or acceptors ($n = 1, 2$). At low doping levels, Si_{Al}^{+1} is predicted to be the dominant Si-containing defect, so adding Si to the system increases the donor concentration (and hence the free electron concentration). At high doping levels, the $V_{Al} + nSi_{Al}$ complexes dominate, so adding Si to the system tends to increase the concentration of $V_{Al} + nSi_{Al}$ acceptors (hence reducing the free electron concentration). In addition to this mechanistic argument, defect and carrier concentrations were predicted using a numerical charge-balance solver (including known background impurities C and O), which qualitatively reproduced the Si compensation knee in AlN. The $V_{Al} + nSi_{Al}$ were demonstrated to be the key ingredient to reproducing the compensation knee with the charge-balance solver. Furthermore, optical emissions were calculated in low-Si doping and high-Si doping conditions for the dominant defects in each condition; these calculations predict a shift in the optical emissions from one doping condition to the other, which was confirmed with detailed photoluminescence measurements.

In Chapter 6, the influence of finite-temperature effects (vibrations and thermal strain) on defect formation energies in AlN is studied. A common misconception about DFT simulations is that they are only ever valid at 0 K, since most DFT studies report ground-state properties. We demonstrate methods to calculate the main contributions to the

temperature dependence of defect formation energies in semiconductors, namely vibrational contributions and thermal strain contributions. We use these methods to calculate temperature-dependent formation energies for common extrinsic (Si, O, and C impurities) and intrinsic (Al and N vacancies) point defects in AlN. The temperature dependence of formation energies and transition levels associated with each these defects is studied in detail, including the separate influences of vibrational and thermal strain contributions. General trends are identified which are common to all or many of these defects. Ultimately, while the results of simulations at absolute zero are found to be valid for qualitative models and quantitative predictions at low temperatures, it is concluded that finite-temperature effects can be significant depending on the defect and property of interest.

Chapter 7 concludes the dissertation. It includes a summary of conclusions from each of the three studies, as well as a discussion of future work. The work included in this dissertation has made important contributions to the understanding of defect-related phenomena in AlN and Al-rich AlGa_N, such as the Si-compensation knee. It also demonstrates valuable theoretical approaches which are rarely used in the literature to date, such as the modeling of defects in a pseudorandom bulk alloy, or the calculation of finite-temperature properties of defects. The author believes that these approaches, especially finite-temperature methods, will become commonplace in the future, as theorists race to understand and predict a wider swathe of physical phenomena in collaboration with experimenters. The tools and techniques developed here, as well as the large dataset (hundreds of defects in AlN in different charge states and configurations, including optical and vibrational information), will be fruitful for many avenues of research in the near future.

CHAPTER

2

LITERATURE REVIEW

In this chapter, I will briefly review some of the literature on Si and O point defect in AlN and AlGa_N. This literature review is meant to give some basic background information necessary to appreciate the content of Chapters 3-6. In each of those chapters, a more detailed review of the relevant literature is presented.

2.1 Si Doping in GaN and Ga-rich AlGa_N

Si is the most common dopant used for n-type doping in GaN. It is a substitutional impurity on the Ga site, where it acts as a single donor. Götz *et al.* used variable temperature Hall effect measurements to establish an activation energy for Si between 12 and 17 meV, and photoluminescence (PL) measurements revealed an optical Si donor level within about 22 meV of the conduction band. [Göt96] The low activation energy suggests that Si is a hydrogenic donor in GaN. Supporting this view, recent state-of-the-art DFT calculations by Gordon *et al.* predict that Si prefers to substitute for Ga in a singly ionized donor state for all Fermi levels within the bandgap. [Gor14]

In Ga-rich AlGaN, the situation is similar. Polyakov *et al.* studied Si donors in $\text{Al}_x\text{Ga}_{1-x}\text{N}$ films with composition $0 < x < 0.6$, and found the activation energy to increase from about 18 meV for $x < 0.1$, to about 50 meV for $x = 0.4$, to less than 90 meV for $x = 0.6$. [Pol98] We can do a back-of-the-envelope calculation to demonstrate that this trend is still consistent with Si being a hydrogenic donor. The ionization energy of a hydrogenic donor is given by the Bohr model:

$$E_{\text{ionization}} = \frac{m^* e^4}{8\epsilon^2 h^2} \quad (2.1)$$

where m^* is the electron effective mass, e is the electron charge, ϵ is the permittivity of the material, and h is Planck's constant. If we substitute $\epsilon = 9.79\epsilon_0$ [BJI73] and $m^* = 0.13m_e$ [Lev01] for GaN, we get an ionization energy of 18.5 meV. If we substitute $\epsilon = 9.14\epsilon_0$ [Col67] and $m^* = 0.40m_e$ [XC93] for AlN, we get an ionization energy of 65.1 meV. In the approximation that the permittivities and the effective masses follow Vegard's Law (linear interpolation with x), we get ionization energies of 35.6 meV and 45.0 meV for $x = 0.4$ and $x = 0.6$, respectively. Thus the activation energies reported by Polyakov *et al.* are close enough to the Bohr ionization energies to suggest that Si remains a hydrogenic donor in Ga-rich AlGaN.

Again the predictions of Gordon *et al.* are consistent with this conclusion, as they predict Si to be a singly ionized donor across the entire bandgap for Al contents up to $x = 0.94$. [Gor14] Gordon's results are based on an interpolation between DFT calculations for GaN and AlN, which takes the empirical band bowing parameter into account. Even if the interpolation is only approximately valid, it is reasonable to conclude that Si is a hydrogenic donor within the composition range explored by Polyakov. Indeed, Polyakov concludes that the increase in ionization energy with Al content is likely attributable to an increased effective mass and a lower permittivity, as opposed to the effects of DX centers (which I will address in the following section).

Figure 2.1 shows Polyakov's plot of electron concentration versus silane flow rate for different $\text{Al}_x\text{Ga}_{1-x}\text{N}$ compositions. Notice that, for every composition other than $x = 0.6$ (for which there are not enough data points to be conclusive), the electron concentration increases linearly (on a log scale) with silane flow above some threshold flow rate. Presumably, the nonlinear behavior below the threshold is due to compensating defects, which are eventually overcome with increased Si doping levels. This is exactly the behavior we would expect from an ideal hydrogenic donor. Even though the Si ionization energy increases with Al content, high carrier concentrations are still achievable via increased Si doping levels.

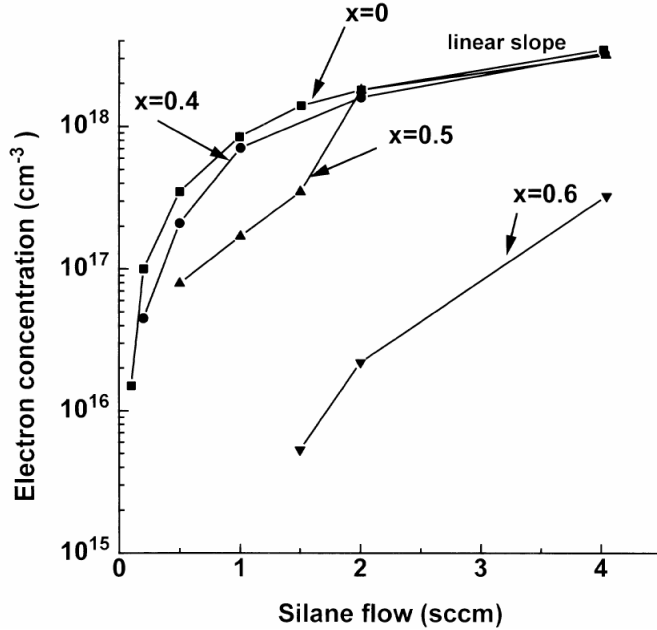


Figure 2.1 Electron concentration versus silane flow in $\text{Al}_x\text{Ga}_{1-x}\text{N}$ films with various Al compositions (as labeled). Reproduced from *Solid-State Electronics* **42**, 4 (1998), with the permission of Elsevier.[Pol98] ©1998 Elsevier.

2.2 Si Doping in AlN and Al-rich AlGaN

From the success of Si doping in Ga-rich AlGaN, it is reasonable to presume that Si doping may be likewise successful in Al-rich AlGaN. Although the ionization energy increases with Al content, in principle this can be overcome with higher doping levels; and therefore controllable, high carrier concentrations should be achievable even in Al-rich AlGaN.

One effect which may limit n-type doping in Al-rich AlGaN is the onset of so-called DX centers. This refers to a class of defects originally proposed by Lang and Logan to explain the observation of persistent photoconductivity in donor-doped AlGaAs. [Lan79] The original model for the DX center was a trap state associated with a defect complex consisting of the donor impurity and an unknown second defect (hence the name “DX center”, where “D” refers to the donor and “X” refers to the unknown defect). However, Morgan later demonstrated that the DX state was actually associated with a simple substitutional defect in which the donor impurity is displaced away from its normal on-site geometry. [Mor86] In this displaced configuration, the donor impurity instead behaves as a compensating acceptor, thereby limiting its effectiveness as an n-type dopant.

At high Fermi levels (near the conduction band edge), Si transitions to a DX state in AlN, but not in GaN, indicating an onset of DX behavior in $\text{Al}_x\text{Ga}_{1-x}\text{N}$ above some threshold Al content. Theoretical predictions of this onset Al content vary widely, including $x = 0.24$ [PC97], $x = 0.6$ [BB97], and $x = 0.94$ [Gor14]. Of these predictions, that of Gordon *et al.* ($x = 0.94$) is based on the most advanced level of theory and is most likely to be close to the true value. For instance, the observation by Collazo *et al.* of a sharp increase in donor activation energy for Si-doped $\text{Al}_x\text{Ga}_{1-x}\text{N}$ at $x = 0.8$ could be due to the onset of a DX transition. [Col11]

In any event, the Si DX transition remains shallow even in AlN. Gordon predicts the DX transition to be 150 meV below the conduction band minimum. [Gor14] Collazo *et al.* measured resistivities at different temperatures to calculate a donor activation energy of 250 meV in Si-doped AlN. [Col11] Similarly, Zeisel *et al.* obtained an activation energy of 320 meV from resistivity measurements [Zei00]; and Goennenwein *et al.* obtained an activation energy of about 345 meV from resistivity measurements, which they confirmed with observations of thermally activated generation-recombination noise. [Goe01] Son *et al.* used temperature-dependent electron paramagnetic resonance (EPR) to obtain an activation energy of about 140 meV for the Si DX state (relative to the CBM). [Son11]

Considering the DX transition as the only self-compensation mechanism, Si should remain a hydrogenic donor in AlGa_N below the Al concentration at which the DX onset occurs. Even above that concentration, the Fermi level should increase with Si doping until it pins near the DX transition level; which means that the carrier concentration should increase with Si doping up to some threshold doping level where the Fermi level is pinned, then level off with further doping. However, what is observed is markedly different behavior.

Shimahara *et al.* measured carrier concentration and mobility as a function of Si concentration in $\text{Al}_{0.65}\text{Ga}_{0.35}\text{N}$ at room temperature; their results are reproduced in Figure 2.2. [Shi11] Their Si concentrations were determined using secondary ion mass spectrometry (SIMS); the decrease in carrier mobility as a function of Si content is likewise consistent with Si incorporation. Whereas we might expect to see carrier concentration increase linearly as a function of Si content, or level off at high doping levels due to a DX transition, Shimahara observed a sharp decrease in carrier concentration at high doping levels. Note also that their samples have 65 percent Al, well below the best prediction for the onset of the DX transition, so it is unlikely that a DX transition plays a role in this behavior.

Shimahara simply ascribes the decrease in carrier concentration at high doping levels

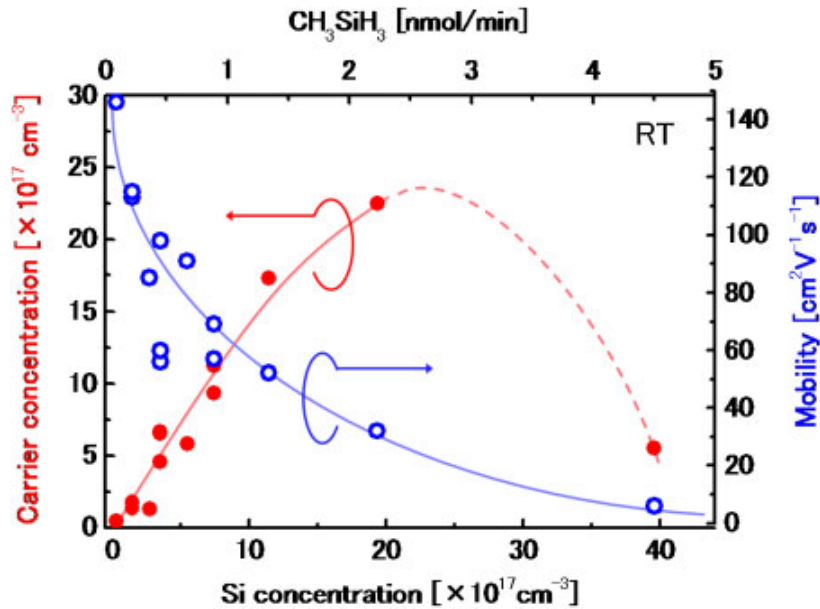


Figure 2.2 Carrier concentration and mobility of Si-doped $\text{Al}_{0.65}\text{Ga}_{0.35}\text{N}$ at room temperature as a function of Si concentration. Reproduced from *Japanese Journal of Applied Physics* **50**, 095502 (2011), with the permission of the Japan Society of Applied Physics.[Shi11] ©2011 The Japan Society of Applied Physics.

to “self-compensation”, and does not speculate as to what defects might contribute to the compensation. Mehnke *et al.* observed a similar trend in Si-doped AlGaN with Al content ranging from 82 to 95 percent. [Meh13] Mehnke attributes this behavior to “self-compensation effects” with a nod to the DX transition, but notes that “the origin of this behavior is still unclear”. Taniyasu *et al.* observed a reduction in carrier concentration with further doping in AlN doped with Si above $3 \times 10^{19} \text{ cm}^{-3}$. [Tan02] They suggest triply ionized cation vacancies as a possible compensating defect. They also note that their obtained donor concentration in highly Si-doped samples is lower than the actual Si concentration, and they suggest that perhaps an antisite Si defect is responsible (Si substituting on the N site, which would also play the role of a compensating acceptor). However, first principles calculations predict that antisite Si defects are never favorable for Fermi levels within the bandgap. [Gor14] Moreover, cation vacancies alone cannot account for the reduced carrier concentration, because increased Si doping would still push the Fermi level higher (and therefore increase the carrier concentration) if cation vacancies were the only compensating defects.

Chichibu *et al.* observed the same behavior, which they term “overcompensation”, in

Si-doped $\text{Al}_{0.6}\text{Ga}_{0.4}\text{N}$. [Chi13] They propose the existence of defect complexes consisting of cation vacancies and silicon as an explanation for the overcompensation as well as observed deep PL emission bands. Supporting this hypothesis, experiment and theory have previously shown that cation vacancies occur in high concentrations in n-type AlN and AlGaN. [Ued12; Ued09; SW02] This explanation also accounts for the observation of Taniyasu *et al.* that the calculated donor concentration is lower than the actual Si concentration in highly doped samples. In Chapter 5, we examine Chichibu's hypothesis in detail, and demonstrate using *ab initio* calculations that the proposed cation vacancy-silicon complexes can indeed account for the overcompensation of Si in AlN and Al-rich AlGaN.

2.3 Oxygen DX Transition in Al-rich AlGaN

Whereas Si is commonly used as an intentional n-type dopant in AlGaN, O is a commonly observed unintentional donor impurity. Like Si, O acts as a hydrogenic donor in GaN and Ga-rich AlGaN, but forms compensating DX centers at high Fermi levels in AlN and Al-rich AlGaN. [McC98] Unlike Si, O prefers to substitute on a N site. The DX transition level is also deeper in the bandgap for O than for Si. [McC99]

Many computational studies have been done on oxygen impurities in AlN. Most of them do not try to extend their results to AlGaN alloy, and simply conclude that O transitions to a deep acceptor level associated with a DX configuration. [SW98; Sta99; SW02; Sil12; MN97; Wal98b] Many of these studies suggest that oxygen self-compensation due to the DX transition level may be responsible for the observed decrease in carrier concentration in unintentionally doped AlGaN as the Al content is increased above 40 percent. However, they do not try to calculate the onset of the DX transition level as a function of Al content.

Park and Chadi calculated formation energies for O in GaN and AlN in an on-site configuration and two different DX configurations, and used linear interpolation to predict the onset of the DX transition level at 20 percent Al. [PC97] However, that study used functionals with the local density approximation, which is known to underestimate bandgaps, which in turn can affect the accuracy of formation energy calculations. Moreover, as Van de Walle points out [Wal98a], Park and Chadi omit important information about their calculations, such as whether the Ga 3d states were treated explicitly or approximated by a pseudopotential. The more recent study by Gordon *et al.* uses hybrid functionals (which can accurately reproduce the bandgaps of many materials, including GaN and AlN) to model O in GaN

and AlN. [Gor14] They use interpolation (including the effects of the bandgap bowing parameter) to predict the onset of the O DX transition level at 61 percent Al.

There is some disagreement in the literature over which DX configuration is the most stable for O in AlN. Earlier studies based on local density functionals conclude that the most stable configuration involves a displacement of the oxygen away from the N site along the c-axis, such that the axial bond is broken. [PC97; Wal98a] However, Gordon finds another configuration to be more stable, in which the O atom has been displaced such that one of the other three bonds is broken. [Gor14] Again, Gordon's findings are more reliable, since they are based on a higher level of theory.

I will finally note that none of these studies explicitly models the O defect in an AlGaN alloy environment. Those that draw conclusions about AlGaN do so by interpolating between results in GaN and AlN. In fact, only one study, by Bogusławski and Bernholc, does any explicit modeling of point defects in AlGaN alloy; but they model C, Si, and Ge, not O. [BB97] In Chapter 4, we will examine oxygen and silicon point defects in $\text{Al}_{0.65}\text{Ga}_{0.35}\text{N}$ via explicit modeling in pseudorandom configurations of the alloy. We will arrive at a number of interesting results that cannot be obtained by interpolation between AlN and GaN.

CHAPTER

3

METHODOLOGY

This chapter serves as a general introduction to the methodology used in this thesis. I will discuss the basics of DFT with some historical background; point defect concentrations and formation energies; how to use DFT to calculate point defect formation energies; how to simulate random alloys in DFT, along with some of the associated challenges and limitations; phonon calculations with DFT; how use phonon simulations to compute temperature-dependent defect formation energies with DFT; the charge-balance defect concentration solver, developed in-house by members of the Irving group; and finally, the Semi-automated Simulation Setup Tool (SSST), which I developed to facilitate the rapid setup of DFT simulations. The discussion here of the SSST is fairly comprehensive, and may serve as a manual for the software, to which future Irving group members may refer.

3.1 Density Functional Theory

The many-body Schrodinger equation is the fundamental equation used to describe a system of nonrelativistic electrons in an arbitrary potential, such as a crystal lattice of ions.

In principle, solutions to the many-body Schrodinger equation can be used to predict structural, electronic, optical, vibrational, and thermodynamic properties of molecules, surfaces and bulk materials. In practice, however, the many-body Schrodinger equation is intractable to solve for many important materials systems even with today's most powerful supercomputers. This intractability stems from the fact that the key quantity which is to be solved, the many-body wavefunction, is a function of coordinates in the configuration space of electrons. That is, for a system of N electrons, the wavefunction is a function of $3N$ variables.

In 1964, Hohenberg and Kohn demonstrated that the ground-state energy of an interacting electron gas in an external potential is a unique functional of the electron density $n(\mathbf{r})$. [HK64] This means that the problem of finding the ground-state energy for a many-body electron system can be mapped from solving a wavefunction of $3N$ variables to a functional of a density function of only 3 variables, since the electron density only depends on three spatial coordinates. However, the Hohenberg-Kohn theorem merely proves the existence of such a functional; it gives no prescription of its exact form.

In the following year, Kohn and Sham used the Hohenberg-Kohn theorem to derive an expression which replaces the many-electron Schrodinger equation with a (non-interacting) single-particle expression where electron-electron interactions are replaced by an interaction between the single-electron orbitals and an effective potential. [KS65] The key to the so-called Kohn-Sham equations is that the electron densities of the many-electron and single-electron systems are proven to be identical with an appropriate effective potential, and since the electron densities are identical, the Hohenberg-Kohn theorem implies that the ground-state energies will be the same.

These seminal papers are the basis of modern Density Functional Theory (DFT), which takes its name from the functional of electron density in the Hohenberg-Kohn theorem. Together, they have been cited over 43,000 times, which is all the more astonishing given that most DFT papers today do not directly cite them. Walter Kohn went on to win a Nobel prize for this work which has been the basis of an entire field of research.

Despite its success, there is an important shortcoming of the Kohn-Sham approach, namely, that the effective potential representing the many-body interaction includes a term for which no exact form is known except in the ideal case of a uniform electron gas. This term, known as the exchange-correlation functional, has been approximated in various ways. The simplest approach, known as the local density approximation (LDA),

assigns the exchange-correlation potential at a given point based on the local electron density at that point, from the known value of the potential for a uniform electron gas of the same density. A slightly more sophisticated approach, known as the generalized gradient approximation (GGA), assigns the exchange-correlation potential at a given point based on the local density as well as the local gradient of the density at that point. Some of the simulations in this thesis, particularly those used for computing phonon properties, make use of a popular GGA functional developed by Perdew, Burke, and Ernzerhof known as the PBE functional.[Per96] LDA and GGA functionals have the advantage of being local or semilocal functions of the electron density, so they can be computed very quickly as compared to a nonlocal functional. Both have been used successfully to calculate various properties of molecules and materials, such as atomic structure and formation enthalpies. However, LDA and GGA also have important limitations; for instance, these functionals are known to underestimate semiconductor bandgaps, and they have a tendency to delocalize wavefunction orbitals.

A number of functionals have been developed which go beyond the local and semilocal approximations. One of the most widely used, which is also used in this thesis, is the functional developed by Heyd, Scuseria, and Ernzerhof known as the HSE (or HSE06) functional.[Hey06; Hey03] The HSE functional mixes in a fraction of nonlocal Hartree-Fock exact exchange with a traditional GGA functional such as PBE. The fraction of exact exchange acts as an input parameter with which one can tune the electron-electron interaction until a parameter of interest matches a desired value (for instance, the bandgap of a semiconductor can be tuned to match an experimentally measured bandgap). HSE functionals with an appropriately tuned bandgap can significantly improve the accuracy of predicted point defect properties, such as formation energies.[Fre14] In this vein, HSE functionals have been used to make accurate predictions of defect formation energies and concentrations of point defects and complexes in InN, GaN, and AlN.[Gor14; Gad14; Gad13; Lyo14; Lyo10; Col12; Sil12; Har18].

All DFT calculations performed for this thesis use the Vienna *Ab initio* Simulation Package (VASP).[KF96a; KF96b; KH94; KH93] VASP is a popular electronic structure code because of its speed, scalability, and reliable pseudopotential library. Pseudopotentials replace core electrons (whose orbitals are rapidly oscillating and therefore slow to converge) with an effective screened potential around the nucleus. So long as the core electron orbitals are not significantly affected by the interactions present in materials and molecules, pseudopo-

tentials are a good approximation and drastically improve computational efficiency. The development of an accurate and robust pseudopotential is a difficult endeavor requiring lots of trial and error. Therefore, the value of a reliable and well-tested pseudopotential library such as that used by VASP cannot be overstated.

VASP uses a plane-wave basis to represent the Kohn-Sham orbitals, and all systems computed by VASP exist in a periodic space. A periodic structure is ideal for representing a perfect crystal, and isolated molecules can be accurately simulated by increasing the size of the periodic cell to eliminate interactions between images of the molecule across the periodic boundary. However, periodic cells present challenges for simulating alloys and point defects, which we will touch upon in subsequent sections.

For more detailed information on DFT in principle and in practice, I recommend a number of introductory treatments with varying levels of depth and technical detail.[BW13; PR10; Cap06; Fio03]

3.2 Point Defect Concentrations from Formation Energies

Point defects constitute the set of defects in an atomic structure which can be defined in a small, contained volume of space. A point defect in a crystal structure may be a vacancy (missing host atoms), substitutional (a host atom replaced by an atom of another element), or interstitial (a host or impurity atom sitting at some location between the lattice sites of the crystal). For practical purposes, we also consider defect complexes (arbitrary combinations of a small number of neighboring point defects) to be point defects, as well.

In semiconductors, point defects are used to control the populations of charge carriers (electrons, holes, and mobile ions) and thereby the electronic and optical properties of the material. Crucial to achieving the high level of control required for making devices is an understanding of the physics of point defects. The goal of this section is to demonstrate how DFT simulations can be used to predict point defect properties so they can be better understood and better controlled. While extended defects such as dislocations, grain boundaries and interfaces, and inclusions can also influence material properties, we will generally ignore them in this thesis, under the operating assumption that the materials of interest will consist of single crystals with low dislocation densities.

The most important property of a point defect is its free energy of formation, or the free energy of a crystal with a single point defect relative to the free energy of the same crystal

without the point defect. As we will demonstrate below, knowledge of the formation energy allows one to predict the concentration of a point defect in the crystal, provided that the concentration is sufficiently dilute. Suppose we know the formation energy E_D^f of some isolated point defect D (for instance, a vacancy on one of the crystal sites). The total free energy of a crystal with n_D such defects on N_D^{site} possible defect sites in the lattice is

$$G^f = n_D E_D^f - T S^{\text{conf}}(n_D, N_D^{\text{site}}) \quad (3.1)$$

where S^{conf} is the configurational entropy of the point defects in the crystal, given by

$$S^{\text{conf}}(n_D, N_D^{\text{site}}) = k \ln \left(\frac{N_D^{\text{site}}!}{n_D! (N_D^{\text{site}} - n_D)!} \right) \quad (3.2)$$

Expanding the logarithm and applying Stirling's approximation, S^{conf} becomes

$$S^{\text{conf}} = k \left(N_D^{\text{site}} (\ln N_D^{\text{site}} - 1) - n_D (\ln n_D - 1) - (N_D^{\text{site}} - n_D) (\ln (N_D^{\text{site}} - n_D) - 1) \right) \quad (3.3)$$

The number of defects n_d in the crystal is that which minimizes the free energy G^f . That is,

$$\begin{aligned} \frac{\partial}{\partial n_D} G^f &= E_D^f - T \frac{\partial}{\partial n_D} S^{\text{conf}}(n_D, N_D^{\text{site}}) \\ &= 0 \end{aligned} \quad (3.4)$$

It is easy enough to take the derivative of Equation 3.3, to obtain

$$\frac{\partial}{\partial n_D} S^{\text{conf}}(n_D, N_D^{\text{site}}) = -k \ln \left(\frac{n_D}{N_D^{\text{site}} - n_D} \right) \quad (3.5)$$

In the dilute limit ($n_D \ll N_D^{\text{site}}$), this is approximately

$$\frac{\partial}{\partial n_D} S^{\text{conf}}(n_D, N_D^{\text{site}}) \sim -k \ln \left(\frac{n_D}{N_D^{\text{site}}} \right) \quad (3.6)$$

Finally, substituting this result into Equation 3.4,

$$E_D^f + k T \ln \left(\frac{n_D}{N_D^{\text{site}}} \right) = 0 \quad (3.7)$$

Solving for n_D ,

$$n_D = N_D^{\text{site}} \exp\left(-\frac{E_D^f}{kT}\right) \quad (3.8)$$

The quantities n_D and N_D^{site} can be interpreted as defect and site concentrations by dividing both sides by the volume of the crystal.

Equation 3.8 is only strictly valid in the limit of dilute concentrations of defects, since we assumed $n_D \ll N_D^{\text{site}}$ as part of its derivation; furthermore, we assume that the average spacing between defects is far enough that any interactions between defects are negligible (or otherwise cancel out in the aggregate). For defect complexes, which may have multiple local configurations N_D^{conf} on a given site, it is a good approximation in the dilute limit to assume that the number of local configurations increases the number of possible sites as a multiplicative factor (that is, replace N_D^{site} by $N_D^{\text{conf}} N_D^{\text{site}}$ in Equation 3.8, an approximation which isn't strictly rigorous since a defect of a particular configuration on a given site restricts the possibility of another defect on the same site with a different configuration).

For a system of multiple defects in the dilute limit, Equation 3.8 is a good approximation for the concentration of each defect individually, since the presence of dilute concentrations of multiple defects has only a small effect on N_D^{site} (again, the interactions between defects must also be negligible or cancel out, if the isolated defect formation energy is valid to use). In a semiconductor with multiple defects in various charge states, the formation energy of charged defects depends upon the Fermi level of the system, and the requirement of charge neutrality allows one to solve for the Fermi level and defect populations under a specific set of environmental conditions. This will be discussed in detail in subsequent sections.

3.3 Point Defects in DFT

We have seen that defect concentrations are determined by their formation energies at a given temperature. In this section, we will discuss how to model an isolated point defect in a DFT simulation, and how to extract formation energies from such a model.

To model an isolated point defect in a periodic DFT simulation, one must embed the defect in a bulk supercell. The supercell must be large enough that the defect does not interact with its images across the periodic boundary. However, computational limitations prohibit arbitrarily large supercells, so various schemes have been developed to ensure that any such interactions are either negligible or corrected in post processing. For instance, a

typical practice is to lock atoms far from the defect into their ideal bulk positions, which ensures that the strain field of the defect does not extend past the periodic boundary (a good approximation if the strain surrounding the defect is not significantly altered).

Charged defects interact electrostatically across the periodic boundary over relatively large distances, depending on the charge and the permittivity of the bulk material. Because it is impractical to model defects in supercells large enough to mitigate this interaction, a popular approach is to subtract the interaction energy from the total energy of the defect cell. In this approach, one must build an electrostatic model representing the charged defect in the supercell, and the interaction energy is then calculated with classical electrostatics. The Madelung potential of a charged supercell is divergent, however, and it can only be made to converge at the cost of an unknown constant added to the electrostatic potential everywhere in the supercell. Therefore, an additional correction to the total energy of the supercell must be applied which accounts for the energy cost of aligning the potential in the defect supercell with the potential in a corresponding (neutral) bulk supercell. I wrote custom software which computes both of these electrostatic energy corrections using a method similar to one developed by Kumagai and Oba.[KO14]

Once we have modeled a defect supercell and a corresponding bulk supercell of the same size, we can compute the defect formation energy using the grand canonical formalism.[WN04; Fre14] In this formalism, the formation energy of a point defect D^q , where q is the charge state, is given by

$$E_{D^q}^f = E_{D^q}^{\text{tot}} - E_{\text{bulk}}^{\text{tot}} - \sum_i n_i \mu_i + q \mu_e + E_{D^q}^{\text{corr}} \quad (3.9)$$

In this expression, $E_{D^q}^{\text{tot}}$ and $E_{\text{bulk}}^{\text{tot}}$ are the total energies, respectively, of a supercell containing defect D^q and of the corresponding bulk supercell, as calculated with DFT simulations; μ_i is the chemical potential of species i , and n_i is the number of atoms of species i exchanged between the bulk and a chemical reservoir in order to create the defect; μ_e is the Fermi level, which is conventionally defined relative to the valence band maximum; and $E_{D^q}^{\text{corr}}$ is a *post-hoc* finite-size correction to the energy of the charged defect supercell (as described above). The chemical potentials reflect environmental conditions during doping (e.g. gas pressures, temperature, elemental abundance).

Data from defect formation energy calculations is typically represented with a formation energy diagram, in which defect formation energies are plotted as a function of the Fermi

level, which is treated as a free parameter that varies across the bandgap. In such a plot, the charge state of a defect is represented by the slope of the line representing its formation energy. Unfavorable charge states at a given Fermi level are often removed in order to reduce clutter (from Equation 3.8, defect concentration varies exponentially with formation energy, so unfavorable charge states at a given Fermi level are insignificant except near transition levels). The Fermi level at which two charge states of a given defect have equal formation energies (i.e. where the slope changes) is known as the thermodynamic transition level between those two states. The thermodynamic transition levels may be thought of as defect states as represented on a vertical band diagram.

Special challenges are presented by modeling defects in alloys and by extending formation energies to finite temperatures. These challenges will be discussed briefly in this chapter, and in depth in subsequent chapters. More detailed information can be found in the excellent review articles on this subject.[WN04; Fre14]

3.4 Random Alloys in Periodic DFT

It is impossible to represent a truly random alloy in a periodic space. Two approaches are commonly used to address the issue of representing a bulk random alloy: quasirandom models and pseudorandom models.

In the quasirandom approach, randomized elements are positioned in such a way as to minimize the statistical correlation between pairs of atoms. In a truly random alloy, the pair correlation should be zero, and the theory is that if the pair correlation is as close as possible to that of a truly random alloy, then the quasirandom model will optimally mimic the properties of the truly random alloy. This has been demonstrated as an effective approach for many random alloy systems, including high-entropy alloys.[]

In this thesis, however, the pseudorandom approach is used. In the pseudorandom approach, random elements are positioned by random sampling with proportions appropriate to the desired concentrations. That is, a given atomic site will be populated with one or another type of element with a probability determined by the alloy composition. This approach is simpler to apply than the quasirandom approach, but may require a larger number of simulations in order to achieve a representative sample size. We found that our pseudorandom simulations of AlGa_N alloy adequately represented key properties of the system (e.g. bandgap, formation enthalpy) with little variation across different samples.

Modeling defects in alloys is another challenge altogether. For instance, consider a defect substituting on a nitrogen site in AlGaN versus AlN. In AlN, the on-site defect only exists in a single configuration, and only one simulation is required to represent it. In AlGaN, by contrast, because the defect is tetrahedrally coordinated to four cation sites which may be randomly populated with either Al or Ga, there are sixteen different nearest neighbor configurations which may have an impact on the formation energy. Some of these configurations are symmetrically equivalent from a nearest neighbor perspective, but the configuration of cations beyond first-nearest neighbors will likely break the symmetry. So one must take pains to determine whether first-nearest neighbors play a role in the defect energetics; then second-nearest neighbors; and so on.

The higher the number of randomized atomic sites that affect the defect formation energy, the higher the number of simulations one must perform to accurately represent the defect. Furthermore, one must ensure that the randomized bulk configuration far from the defect does not significantly affect the formation energy. Clearly, there are many challenges to modeling a defect in an alloy environment. Chapter 4 is a case study of Si and O defects in AlGaN, in which many of these challenges are met and explored in detail.

3.5 Phonon Calculations

The harmonic approximation comes from writing a Taylor expansion of the energy of a system as a function of the positions of the ions in the system. The Taylor expansion of the energy about the equilibrium ion positions is given by

$$E(\mathbf{x}) = E(\mathbf{x}_0) + \frac{1}{2} \sum_{i,j} \Delta x_i \Delta x_j \frac{\partial^2 E(\mathbf{x}_0)}{\partial x_i \partial x_j} + O(\Delta x^3) \quad (3.10)$$

where \mathbf{x} is the configuration space of ions in the system, \mathbf{x}_0 is the equilibrium configuration, x_i indicates the i th component of \mathbf{x} , and Δx_i is a small displacement along component i . The first term, $E(\mathbf{x}_0)$, is the ground state energy of the system (as calculated by DFT, for example). The second term, which acts like a harmonic oscillator, represents the vibrational contribution to the total energy. All other terms are higher order in the small displacements Δx_i .

The basic procedure to compute vibrational properties is to calculate the dynamical

matrix D_{ij} , given by

$$D_{ij} = \frac{1}{\sqrt{M_i M_j}} \sum_l \left[\frac{\partial^2 E(\mathbf{x}_0)}{\partial x_i \partial x_j} e^{-i\mathbf{q}\cdot\mathbf{R}_l} \right] \quad (3.11)$$

where M_i is the mass of the ionic nucleus associated with index i ; \mathbf{R}_l is a lattice translation vector indexed by l (covering all linear combinations of lattice basis vectors); and \mathbf{q} is a reciprocal-space vector (phonon wavevector) within the first Brillouin zone. The exponential factor and the summation over l constitute a Fourier transformation of the matrix of second derivatives. Thus the dynamical matrix is the Fourier transform of a matrix of mass-weighted second derivatives of the system energy with respect to small displacements of the ions. The eigenvectors and eigenvalues of the dynamical matrix, given by

$$D\mathbf{w}_i = \omega_i^2 \mathbf{w}_i \quad (3.12)$$

correspond to displacement vectors \mathbf{w}_i and frequencies ω_i , respectively, where each index i indicates a normal vibrational mode.

The oscillations of the system are quantized by treating each normal vibrational mode as a quantum harmonic oscillator, and the excited states of these quantized oscillators are known as phonons. Thus each phonon mode i is imagined as an independent harmonic oscillator, where the positions of the ions oscillate about the equilibrium configuration \mathbf{x}_0 along the vector \mathbf{w}_i , with frequency ω_i . The energy E_i^{ph} of phonon mode i is given by the energy eigenvalues of the quantum harmonic oscillator with frequency ω_i , that is,

$$E_i^{\text{ph}} = \left(\frac{1}{2} + n_i \right) \hbar \omega_i \quad (3.13)$$

where n_i is the number of phonons in mode i . Note that ε_i is finite even when $n_i = 0$; the remaining energy, $\hbar\omega_i/2$, is known as the zero point energy of phonon mode i .

From Equation 3.11, one observes that the dynamical matrix is a function of the phonon wavevector \mathbf{q} . The phonon dispersion relation can be computed by solving for the eigenvalues of the dynamical matrix as a function of \mathbf{q} . Below, we omit explicit reference to \mathbf{q} for the sake of notational simplicity. In principle, the thermodynamic quantities derived below must be integrated with respect to \mathbf{q} over the first Brillouin zone; however, for large supercells, numerical integration over the first Brillouin zone is well-converged by sampling at the Γ -point ($\mathbf{q} = \mathbf{0}$).

Inasmuch as they are modeled by an infinite set of quantum harmonic oscillators,

phonons in an infinite crystal are bosons, and they follow Bose-Einstein statistics. I will briefly derive the most relevant results of such a distribution. The partition function Z_i for a harmonic oscillator with frequency ω_i is given by

$$Z_i = \sum_{n_i=0}^{\infty} \exp\left(-\frac{(\frac{1}{2} + n_i)\varepsilon_i}{kT}\right) \quad (3.14)$$

where $\varepsilon_i = \hbar\omega_i$ is the energy associated with adding or removing a single phonon, k is Boltzmann's constant, and T is temperature. This summation is a geometric series in $\exp(-\varepsilon_i/kT)$, which converges to

$$Z_i = \frac{\exp(-\varepsilon_i/2kT)}{1 - \exp(-\varepsilon_i/kT)} \quad (3.15)$$

The partition function for a set of independent (non-interacting) phonons is the product of their individual partition functions:

$$Z = \prod_i Z_i \quad (3.16)$$

Now that we have the partition function for a system of phonons, we are in a position to derive the free energy, internal energy, entropy, and heat capacity associated with them.

The phonon free energy F_{ph} may be obtained from the partition function via

$$\begin{aligned} F_{\text{ph}} &= -kT \ln Z \\ &= \frac{1}{2} \sum_i \varepsilon_i + kT \sum_i \ln\left(1 - \exp(-\varepsilon_i/kT)\right) \end{aligned} \quad (3.17)$$

Because the chemical potential of phonons is zero, the free energy given by this expression is equivalent to the grand potential of the phonon distribution. The first, temperature-independent term is the zero point energy associated with atomic vibrations, which remains even as the temperature approaches absolute zero.

The entropy S_{ph} is obtained by taking the derivative of the free energy with respect to

temperature:

$$\begin{aligned}
S_{\text{ph}} &= -\frac{\partial F_{\text{ph}}}{\partial T} \\
&= -k \sum_i \left[\ln(1 - \exp(-\epsilon_i/kT)) - \frac{\epsilon_i}{kT} \frac{1}{\exp(\epsilon_i/kT)} - 1 \right]
\end{aligned} \tag{3.18}$$

Note that, despite the zero point energy, the entropy approaches zero as T approaches 0 K, as it should.

To derive the total internal energy of the phonon distribution, we must first determine an expression for the average number of phonons. The average number of phonons N_i of frequency ω_i is given by

$$N_i = \sum_{n_i=0}^{\infty} n_i P(n_i) \tag{3.19}$$

where $P_i(n_i)$ is the probability that n_i phonons will occupy mode i . In terms of the partition function,

$$\begin{aligned}
N_i &= \frac{1}{Z_i} \sum_{n_i=0}^{\infty} n_i \exp\left(-\frac{(\frac{1}{2} + n_i)\epsilon_i}{kT}\right) \\
&= -\frac{1}{Z_i} \sum_{n_i=0}^{\infty} \left(\frac{1}{2} + kT \frac{\partial}{\partial \epsilon_i}\right) \exp\left(-\frac{(\frac{1}{2} + n_i)\epsilon_i}{kT}\right) \\
&= -\frac{1}{Z_i} \left(\frac{1}{2} + kT \frac{\partial}{\partial \epsilon_i}\right) \sum_{n_i=0}^{\infty} \exp\left(-\frac{(\frac{1}{2} + n_i)\epsilon_i}{kT}\right) \\
&= -\frac{1}{Z_i} \left(\frac{1}{2} + kT \frac{\partial}{\partial \epsilon_i}\right) Z_i \\
&= -\left(\frac{1}{2} + \frac{kT}{Z_i} \frac{\partial}{\partial \epsilon_i} Z_i\right)
\end{aligned} \tag{3.20}$$

Finally, evaluating the derivative and simplifying the result,

$$N_i = \frac{1}{\exp(\epsilon_i/kT)} - 1 \tag{3.21}$$

Now we can write the total internal energy U_i of the system of phonons as

$$\begin{aligned} U_{\text{ph}} &= \sum_i \left(\frac{1}{2} + N_i \right) \varepsilon_i \\ &= \frac{1}{2} \sum_i \varepsilon_i + \sum_i \frac{\varepsilon_i}{\exp(\varepsilon_i/kT) - 1} \end{aligned} \quad (3.22)$$

As a sanity check, note that the free energy, entropy and internal energy are related by

$$F_{\text{ph}} = U_{\text{ph}} - TS_{\text{ph}} \quad (3.23)$$

which is indeed true by substitution.

The heat capacity of the phonons is given by the temperature derivative of the internal energy,

$$\begin{aligned} C_{\text{ph}} &= \frac{\partial}{\partial T} U_{\text{ph}} \\ &= - \sum_i \left(\frac{\varepsilon_i^2}{kT^2} \right) \frac{\exp(\varepsilon_i/kT)}{\left(\exp(\varepsilon_i/kT) - 1 \right)^2} \end{aligned} \quad (3.24)$$

Equations 6.11-6.17, if computed for a phonon distribution from a finite supercell, express thermodynamic quantities in units per supercell. For instance, Equation 6.17 gives the heat capacity of the phonon distribution within the supercell, and would need to be divided by the supercell volume in order to be expressed as a volumetric heat capacity.

3.6 Temperature-dependent Defect Formation Energies

At finite temperatures, Equation 3.9 must be modified to include the temperature dependence of the bulk and defect system energies, as well as the temperature dependence of the chemical potentials. Under the assumption that the vibrational free energy is the predominant contribution to the free energy of a bulk semiconductor or an isolated point defect in

the semiconductor, Equation 3.9 becomes

$$\begin{aligned}
E_{D^q}^f(T, P) = & E_{D^q}^{\text{tot}}(V(T)) - E_{\text{bulk}}^{\text{tot}}(V(T)) \\
& + F_{D^q}^{\text{vib}}(T) - F_{\text{bulk}}^{\text{vib}}(T) \\
& - \sum_i n_i \mu_i(T, P) + q\mu_e + E_{D^q}^{\text{corr}}
\end{aligned} \tag{3.25}$$

The quantities in Equation 3.25 which are repeated from Equation 3.9 are defined in the exact same way, albeit with explicit dependencies on temperature (T), pressure (P), and supercell volume (V) included. As written, Equation 3.25 presumes that the vibrational free energies $F_{D^q}^{\text{vib}}(T)$ and $F_{\text{bulk}}^{\text{vib}}(T)$ are independent of thermal strain, which we have demonstrated to be a good approximation in AlN (see Chapter 6). Thermal strain contributions are only considered via the dependence of supercell energies on the temperature-dependent cell volume, $E_{D^q}^{\text{tot}}(V(T))$ and $E_{\text{bulk}}^{\text{tot}}(V(T))$. Thermal strain itself may be computed theoretically or taken from tabulated thermal expansion data.

The chemical potentials μ_i are ultimately determined by the doping environment, but it is possible to place upper and lower bounds on them by considering alternative phases into which the elements may segregate. The procedure for calculating bounds on the chemical potentials is described in the review articles by Van de Walle and Freysoldt.[WN04; Fre14] These upper and lower bounds are sensitive to temperature and pressure via the dependence of the free energies of the reference phases on temperature and pressure. Such dependencies of the reference phases may either be computed or taken from tabulated thermochemical data (readily available for most common bulk phases).

The vibrational free energies $F_{D^q}^{\text{vib}}(T)$ and $F_{\text{bulk}}^{\text{vib}}(T)$ from Equation 3.25 are simply the free energies of the phonon distributions of the defect and bulk supercells, respectively. Section 3.5 outlines the procedure for obtaining the vibrational free energy of a supercell, given a minimum-energy configuration of the ions in the supercell. Following that procedure, Equation 3.17 may be used to compute the vibrational contributions to the temperature dependence of the defect formation energy. Note that the zero-point energy contributes to the total energy of the supercell even at absolute zero. The zero-point energy contribution (which is usually small) is necessarily neglected if the phonon distribution is not computed.

For periodic systems, the dynamical matrix can be represented in reciprocal space, and key properties can be computed via integration over the Brillouin zone. This approach allows one to use relatively small supercells to compute the phonon distribution for a bulk

system, provided a suitably dense grid of reciprocal-space points is used to represent the variation of the phonon distribution over the Brillouin zone. For an isolated point defect, the supercell should be large enough that defect-associated vibrational interactions across the periodic boundary are negligible.

Finally, note that the harmonic model does not include the effects of thermal strain. In principle, one can include thermal strain either by considering anisotropic behavior explicitly (which goes beyond the harmonic approximation)[Gra09; Gra11a], or by applying the harmonic approximation to artificially strained supercells (the so-called quasi-harmonic approximation)[Gra07]. As a third alternative, we can assume that phonon and strain effects add orthogonally (i.e. the phonon density of states is not significantly affected by thermal strain). This third approach is tacitly assumed in Equation 3.25, and will be the approach taken in this thesis.

3.7 Defect Solver

As described in Section 3.2, defect concentrations may be obtained from Equation 3.8. However, for a set of charged defects in a semiconductor, Equation 3.9 (or for finite temperatures, Equation 3.25) shows an undetermined dependence of the defect formation energies (and therefore concentrations) on the Fermi level μ_e . We may solve for the Fermi level, and thereby obtain a consistent set of defect concentrations for a given set of defects and environmental conditions (temperature and chemical potentials), by imposing the condition of charge neutrality on the semiconductor as a whole. Charge neutrality is expressed by

$$p - n + \sum_{i,q} q[D_i^q] = 0 \quad (3.26)$$

where n and p are the electron and hole concentrations, and $[D_i^q]$ is the concentration of defect D_i in charge state q . For nondegenerate semiconductors (i.e. the Fermi level is within the bandgap), n and p are well approximated by

$$\begin{aligned} n &= N_c \exp\left(\frac{\mu_e - \epsilon_c}{kT}\right) \\ p &= N_v \exp\left(\frac{\epsilon_v - \mu_e}{kT}\right) \end{aligned} \quad (3.27)$$

where ϵ_c and ϵ_v are the CBM and VBM, respectively; and N_c and N_v are the effective densities of states of the conduction band and valence band, respectively, given by

$$\begin{aligned} N_c &= 2 \left[\frac{2\pi m_e^* k T}{h^2} \right]^{3/2} \\ N_v &= 2 \left[\frac{2\pi m_h^* k T}{h^2} \right]^{3/2} \end{aligned} \quad (3.28)$$

where m_e^* , m_h^* are the electron and hole density of states effective masses, respectively; and h is Planck's constant. Carrier concentrations can also be determined from a calculated density of states, by numerically integrating the product of the Fermi distribution and the density of states over the valence bands (for holes) and conduction bands (for electrons). In this latter approach, changes in the shapes of the bands as a function of temperature are often neglected due to computational necessity; and the change in the bandgap as a function of temperature must be taken into account (for example, by a rigid shift of the band edges). Both approaches yield consistent results for nondegenerate semiconductors.

The left-hand side of Equation 3.26 expresses the net charge of the crystal due to free electrons, free holes, and charged defects. By substituting Equations 3.27 and 3.9 into Equation 3.26 and taking the derivative with respect to the Fermi level, it is easy to demonstrate that the net charge is a monotonic function of the Fermi level. Therefore, a unique Fermi level exists which satisfies the charge balance condition (net charge equals zero).

Based on this principle, we developed a numerical charge balance solver to simulate doping at an elevated temperature followed by a quench to room temperature.[Bak17; Gad13] After the quench, defect concentrations are frozen in, but each defect is allowed to change its charge state in order to achieve charge balance. The code for the charge balance solver is designed to be modular, so it can be expanded upon and used in other codes. In addition to aiding in the design and implementation of it, I added the ability to include phonon free energies and thermal strain effects in the computation of defect formation energies from our data. This powerful tool can be used to predict defect concentrations from DFT simulation data in a wide variety of environmental conditions, determined by input variables such as temperature, chemical potentials, and elemental concentrations.

3.8 Semi-automated Simulation Setup Tool

For realistic doping and quenching simulations, the defect solver described in Section 3.7 can require data from hundreds of simulations of defects in different configurations and charge states. Generating and analyzing this amount of data by hand is tedious and time-consuming, not to mention error-prone. To this end, we have created separate but complementary toolsets for data generation and data management (storage and analysis). For data management, my colleague Jonathon Baker developed a database which automatically imports, stores, and processes useful data from our simulations. Information about this database may be found in Jonathon Baker's PhD Thesis.[Bak18a]

For data generation, I developed a Semi-automated Simulation Setup Tool (SSST) which can be used to import the input files from a VASP simulation, make scripted modifications to them, then export the modified input files. This tool dramatically speeds up the process of setting up simulations while simultaneously reducing the possibility of error. Although it was written as a data generation tool, it can also be used for many types of analysis. The SSST is written in Python 2.7, and consists of a modular library of general-purpose functions which is easy to build upon, in addition to a library of scripts written for specific applications (for instance, creating a defect simulation from a pre-existing bulk simulation). The modular library is split into modules pertaining to the four input files required by VASP (POSCAR, POTCAR, KPOINTS, INCAR), plus an additional module for system-level functions (i.e. functions which require or modify multiple input files at once).

In the following subsections, I will detail the structure and purpose of each module, including many of the classes and functions it contains. As an example of its utility, I will also discuss how the SSST is used to set up defect simulations with a relatively simple Python script.

3.8.1 The poscar Module

VASP uses the POSCAR file to define the geometry of a simulation. The POSCAR file includes a header, a lattice parameter which uniformly scales the crystal lattice, a set of lattice vectors which define the shape of the periodic cell, the number of atoms of each species (with optional labels, usually just the symbol for each element), and the positions of every atom in the crystal (optionally defined in either Cartesian or direct coordinates). The POSCAR file also includes an optional feature called "Selective Dynamics", which allows the user to

Table 3.1 Variables of the PoscarData class. These variables constitute an abstract representation of a VASP POSCAR file.

Variable	Example	Description
Name	'AlN'	POSCAR file header
LatticeParameter	3.09	Uniformly scales coordinates
LatticeVectors	[[0.5, -0.866, 0.0] [0.5, 0.866, 0.0] [0.0, 0.0, 1.6]]	Matrix of crystal lattice vectors
AtomSpecies	True	True if atomic species are labeled
AtomSpeciesList	['Al', 'N']	Labels for each atomic species
AtomNumbers	[2, 2]	Number of atoms of each species
CoordinateSystem	True	Direct (True) or Cartesian (False)
AtomCoordinates	[[[0.333, 0.667, 0.0], [0.667, 0.333, 0.5]], [[0.333, 0.667, 0.379], [0.667, 0.333, 0.879]]]	Atom positions indexed by [species][atom][component]
SelectiveDynamics	True	True if Selective Dynamics is on
AtomFreezeFlags	[[[True, True, True], [True, True, True]], [[True, True, True], [True, True, True]]]	True if atom coordinate is frozen (indices correspond to AtomCoordinates)
ExtraLines	-	Dummy variable for optional lines
PoscarList	-	List representation of POSCAR file

Table 3.2 Methods of the PoscarData class. These functions are used to modify or analyze the information contained in a POSCAR file. Function inputs other than `self` are listed beneath each function, along with the variable type and a short description.

Function	Description
<code>__init__</code> POSCAR (str)	Initialize PoscarData object from file Path to imported POSCAR file
<code>updatePoscarList</code> PREC (int)	Update PoscarList using class variables Number of decimal places to represent floats
<code>printPoscar</code> PREC (int)	Print PoscarList to screen in POSCAR format Number of decimal places to represent floats
<code>writePoscar</code> POSCARPATH_OUT (str) PREC (int)	Write PoscarList to file in POSCAR format Path to output POSCAR file Number of decimal places to represent floats
<code>addInterstitial</code> POSITION (list, float) SPECIES (str) FREEZE_FLAGS (list, bool)	Insert an interstitial defect Interstitial coordinate $[x_1, x_2, x_3]$ Interstitial species (element) AtomFreezeFlags for interstitial coordinate
<code>addSubstitutional</code> SITE (list, float) or (tuple, int) DX_SHIFT (list, float) SUBSTITUENT (str)	Insert a substitutional defect Site coordinate $[x_1, x_2, x_3]$ or index (species, atom) Displacement vector $[x_1, x_2, x_3]$ Substitutional species (element)
<code>addVacancy</code> SITE (list, float) or (tuple, int)	Insert a vacancy defect Site coordinate $[x_1, x_2, x_3]$ or index (species, atom)
<code>cartesianToDirect</code>	Convert from Cartesian to direct coordinates
<code>directToCartesian</code>	Convert from direct to Cartesian coordinates
<code>changeBasis</code> CHANGE_MATRIX (list, list, int)	Linearly combine basis vectors to reshape the cell Transformation matrix applied to lattice vectors
<code>extendLattice</code> INTEGER_LIST (list, int)	Extend the lattice by integer factors List of factors to extend each lattice vector
<code>relaxationSphere</code> RADIUS (float) CENTER (list, float) IgnoreCellBoundary (bool)	Define a sphere within which atoms may relax Radius of relaxation sphere (Å) Coordinate of center of relaxation sphere If True, let sphere overlap with periodic images
<code>displacementSphere</code> DRADIUS (float) DMAGNITUDE (float) RRADIUS (float) CENTER (list, float)	Define a sphere in which atoms are displaced Radius of displacement sphere (Å) Maximum displacement magnitude (Å) Relaxation sphere radius (Å) Coordinate of center of displacement sphere

Table 3.2 (continued).

IgnoreCellBoundary (bool)	If True, let sphere overlap with periodic images
MODE (str)	Defines how atoms will be displaced
relaxationVolume	Define a parallelepiped where atoms may relax
RANGE1 (tuple, float)	Range on (0, 1) for lattice vector a_1
RANGE2 (tuple, float)	Range on (0, 1) for lattice vector a_2
RANGE3 (tuple, float)	Range on (0, 1) for lattice vector a_3
rotateLatticeVectors	Apply rotation matrix to the system
ROTATION_MATRIX (list, list, float)	Rotation matrix applied to lattice vectors
rotateLatticeVectorsByAngle	Rotate about a specified lattice vector
AXIS_INDEX (int)	Axis of rotation (index of lattice vector)
ANGLE (float)	Rotation angle (radians)
scaleLattice	Scale the lattice along each lattice vector
SCALAR1 (float)	Scaling factor for lattice vector a_1
SCALAR2 (float)	Scaling factor for lattice vector a_2
SCALAR3 (float)	Scaling factor for lattice vector a_3
scaleLatticeVectors	Scale lattice vectors, inversely scale parameter
SCALAR (float)	Scaling factor
scaleLatticeParameter	Scale lattice parameter, inversely scale vectors
SCALAR (float)	Scaling factor
telescopeAtomCoordinates	Move atoms to positions inside the cell
translateAtomCoordinates	Translate all atoms by a vector
VECTOR_FROM (list, float)	Coordinate of tail of translation vector
VECTOR_TO (list, float)	Coordinate of head of translation vector
freezeAtoms	Set all freeze flags to False
unfreezeAtoms	Set all freeze flags to True
invertAtomFreezeFlags	Switch all freeze flag booleans
getAtomList	Return a list of objects representing each atom
getCellVolume	Return the volume of the cell
getCoordinateFromSite	Return atom coordinate from site indices
SITE (tuple, int)	Atomic site indexed by (species, atom)
getCoordinateList	Return all atom coordinates in a NumPy array
getInterstitialSites	Return array of possible interstitial sites
getMetric	Return the metric of the lattice vectors
getReciprocalLatticeVectors	Return the reciprocal lattice vectors
measureDistanceSquared	Measure distance squared with a metric
VECTOR1 (list, float) or (tuple, int)	Coordinate or site index
VECTOR2 (list, float) or (tuple, int)	Coordinate or site index
measureInterplanar . . .	
. . .DistanceSquared	Distance between (hkl) planes

Table 3.2 (continued).

PLANE (list, int)	Miller indices of crystallographic plane
measureLeastDistanceSquared	Shortest distance in periodic space
VECTOR1 (list, float) or (tuple, int)	Coordinate or site index
VECTOR2 (list, float) or (tuple, int)	Coordinate or site index
measureMinimumCell... ...WidthSquared	Smallest width of the cell
measureNearestNeighbor... ...DistanceSquared	Nearest neighbor distance to coordinate
COORDINATE (list, float)	Coordinate to find nearest neighbor of
getNearestNeighborIndex	Index of nearest neighbor to coordinate
COORDINATE (list, float)	Coordinate to find nearest neighbor of
getNearestNeighborList	List of N nearest neighbors to coordinate
COORDINATE (list, float)	Coordinate to find nearest neighbors of
NumberNeighbors (int)	The number of nearest neighbors to return
NumberShells (int)	Number of shells of periodic cells to consider

freeze any or all atomic coordinates in the configuration space of the system during atomic relaxations (for instance, for a surface simulation, one may desire to freeze one or more planes of atoms far from the surface, to simulate a “bulk-like” region).

The SSST `poscar` module is used to import and modify POSCAR files. It consists of five submodules: `readWrite`, `modify`, `analyze`, `common`, and `error`.

The `poscar.readWrite` submodule is the only one a typical user will directly interact with. It contains functions for importing a POSCAR file, printing it to the terminal, and writing it to a new file. Most importantly, it contains the `PoscarData` class, which is an abstract representation of the POSCAR file as a collection of Python objects. The variables of the `PoscarData` class are summarized in Table 3.1, and the methods of the class are summarized in Table 3.2. The class variables can be manipulated directly or via the class methods.

Aside from the initialization method and methods for printing and writing to a file, the methods fall into two general categories (separated by a blank line in the table): modification and analysis. The modification methods will alter the information in the `PoscarData` object; for instance, the coordinates of a system might be scaled or translated. These methods typically reference functions in the `modify` submodule. The analysis methods compute and return new information from the `PoscarData` object without changing the object itself; for instance, the distance between two atoms might be computed. These

Table 3.3 Variables of the PotcarData class. These variables constitute an abstract representation of the header of a VASP POTCAR file.

Variable	Example	Description
NElements	2	Number of elements in POTCAR
XCFunctionals	['PBE', 'PBE']	Exchange-correlation functionals
AtomLabels	['Al', 'N']	Pseudopotential labels
Dates	['04Jan2001', '08Apr2002']	Pseudopotential creation dates
NElectrons	[3.0, 5.0]	Number of valence electrons
Elements	['Al', 'N']	Element types (chemical symbols)
ValenceOrbitals	['s2p1', 's2p3']	Valence orbital configurations
ENMAX	[240.3, 400.0]	Default plane-wave energy cutoff
AtomicMass	[26.981, 14.001]	Atomic masses (g/mol)
PotcarList	-	List representation of POTCAR file

methods typically reference functions in the analyze submodule.

The common submodule contains a handful of general functions commonly used by both the modify and analyze submodules. The error submodule contains functions for checking the consistency of a PoscarData object (i.e. whether it will write a correctly formatted POSCAR file without errors such as overlapping atom coordinates). Errors specific to the poscar module will trigger a special error class, PoscarError, usually with a message pertaining to the nature of the error.

The poscar module allows a user to easily import an existing POSCAR file, obtain information from it, make modifications to it, and write a new POSCAR file to another location with the desired modifications. More importantly, the poscar module allows such modification and analysis to be performed by a Python script, and therefore may be used as a simple automation tool for setup and analysis.

3.8.2 The potcar Module

VASP uses the POTCAR file to define the pseudopotential used for each atomic species in a simulation. VASP includes a library of POTCAR files suitable for each element, and these may be concatenated together to create a POTCAR file for a simulation with more than one element type. The order of the files concatenated together to make a POTCAR file must

match the order of the atomic species index in the POSCAR file (VASP uses the order to assign a pseudopotential to each atom in the POSCAR file).

The `potcar` module contains two submodules, `readWrite` and `error`. The `error` submodule contains a special error class, `PotcarError`, which is triggered by errors specific to the `potcar` module. The `readWrite` module contains functions for importing and writing POTCAR files. It also contains the `PotcarData` class, which abstracts some of the information in the header of a POTCAR file as a collection of Python objects. The variables of the `PotcarData` class are summarized in Table 3.3.

Because of the large size of POTCAR files, `PotcarData` objects do not contain all of the information necessary to reproduce a POTCAR file. Therefore, the `writePotcar` method works by specifying a list of paths to POTCAR files, which are then concatenated together. By default, VASP contains a set of pseudopotential libraries with subdirectory names corresponding to `PoscarData.AtomLabels`, each of which contains a POTCAR file for the corresponding pseudopotential. For automation scripts, the simplest approach is to provide a path to the desired pseudopotential library, and use `AtomLabels` to define the rest of the path for each POTCAR file.

3.8.3 The `kpoints` Module

VASP uses the KPOINTS file to define a grid of weighted integration points in the reciprocal space representation of the cell. Integrals over the Brillouin zone are approximated by a weighted sum of values at these discrete gridpoints. It is possible to define unweighted k-points, where eigenvalues of the system are computed but do not contribute to reciprocal-space integration (for instance, a set of unweighted k-points may be used to define paths for a band structure calculation). The KPOINTS file can have a number of different formats depending on the input mode (defined in the file). Therefore, any abstract representation of a KPOINTS file must be flexible enough to account for the various formats.

The `kpoints` module is used to import, modify, and write KPOINTS files. It has four submodules: `readWrite`, `modify`, `common`, and `error`.

The `readWrite` submodule is the only one a typical user will interact with. It contains functions for importing, printing, and writing KPOINTS files. It also contains the `KpointsData` class, which is an abstract representation of a KPOINTS file as a collection of Python objects. Table 3.4 summarizes the variables of the `KpointsData` class. Note that some variables are undefined depending on the value of `KpointsData.CoordinateMode`.

Table 3.4 Variables of the KpointsData class. These variables constitute an abstract representation of the header of a VASP KPOINTS file.

Variable	Example	Description
Name	'Auto'	Header of KPOINTS file
NumberKpoints	32	Number of k-points
MeshGenerationMode	False	Automatic (True) or manual (False)
CoordinateMode	0	0=Explicit, 1=GammaCentered, 2=MonkhorstPack, 3=Auto, 4=LineMode
CoordinateSystem	True	Direct (True) or Cartesian (False)
MeshDensity	[2, 2, 2]	Number of k-points along each axis
MeshShift	[0.0, 0.0, 0.5]	Vector to shift origin of k-point grid
MeshLength	10	Sets MeshDensity for Auto mode
KpointCoordinates	[[0.0, 0.0, 0.0], [0.5, 0.5, 0.5]]	List of k-point coordinates
KpointWeights	[8.0, 1.0]	List of k-point weights
NormalizedKpointWeights	[0.5, 0.0625]	List of normalized k-point weights
NumberLines	3	Number of lines in LineMode
LineDensity	25	Number of k-points per line
LineVertices	[[0.0, 0.0, 0.0], [0.5, 0.5, 0.5], [0.0, 0.0, 0.5]]	Coordinates for line endpoints
KpointsList	-	List representation of KPOINTS file

Currently, the `KpointsData` class contains only one method aside from printing and writing files. The method is `scaleMeshDensity`, which allows the user to apply any scalar factor to a k-points mesh in Monkhorst-Pack mode; the method scales the density along each lattice vector to the nearest integer, odd integer, or even integer. As an example, this method might be used in conjunction with `PoscarData.extendLattice` in order to scale the k-point mesh density approximately inversely with the scaling of the lattice vectors.

The `scaleMeshDensity` method is called from the `modify` submodule. The `common` submodule contains a number of functions for generating an explicit k-point mesh from a corresponding automatic mesh generation scheme. These functions might be useful, for example, in a script which sets up a band structure calculation from an existing simulation with a KPOINTS file in Monkhorst-Pack mode. Finally, the `error` submodule contains various consistency checks to ensure that a given KPOINTS file is properly formatted, in addition to a special error class, `KpointsError`, which is raised by errors unique to the `kpoints` module.

3.8.4 The `incar` Module

VASP uses the INCAR file to define all simulation settings not found in the POSCAR, POTCAR, and KPOINTS files. Each of these settings is defined by a particular variable, whose value may be a different type (string, integer, etc.) depending on the setting it is used to define. In the INCAR file, exactly one variable may be defined per line in the following format: `VARIABLE = VALUE`. Blank lines and comments (with the symbol `#`) are ignored by VASP. Additionally, it is not necessary to include every possible variable in an INCAR file; a variable required for a particular simulation is set to a default value if it is not defined in the INCAR file.

The `incar` module is used to import, modify, and write INCAR files. It contains three submodules: `readWrite`, `common`, and `error`.

The `readWrite` module is the only one a typical user will interact with. It contains functions for importing, printing, and writing INCAR files, and it also contains the `IncarData` class, which is an abstract representation of an INCAR file. When an INCAR file is imported as an `IncarData` object, a class variable called `IncarDict` is created. `IncarDict` is a Python dictionary object, whose keys are strings of the INCAR variable names, and whose corresponding values are the values of the INCAR variables. For instance, `IncarDict['ENCUT']` gives the value of the plane-wave cutoff energy (defined by the `ENCUT` variable in the IN-

CAR file). Storing the INCAR variables as a Python dictionary is the most flexible way to handle an arbitrarily large set of variables of different types (many VASP INCAR variables are poorly documented, and new ones are regularly introduced as new features are added).

`IncarDict` is not intended to be interacted with directly. Instead, the user may use three methods to manipulate `IncarDict`. `getFlagValue` retrieves the value of an INCAR variable, `setFlagValue` sets or changes the value of an INCAR variable, and `removeFlag` removes the entry for an INCAR variable from `IncarDict`. The `writeIncar` method is used to write an INCAR file from an `IncarData` object. It includes optional formatting variables `VERBOSITY` and `DEPENDENCY`. `VERBOSITY` is an integer from 0 to 3 (1 by default), which specifies the following behavior when writing an INCAR file: (0) specified flags only; (1) include category headers relevant for specified flags; (2) include all category headers; (3) include common unspecified flags and all category headers. The `DEPENDENCY` option is a boolean which, if `True`, indents INCAR flags which are dependent on others (dependent flags are always written on the lines immediately below the flag they are dependent on). INCAR flags are always written in the same order, regardless of their order in the original imported INCAR file. Although it may seem like a minor feature, these formatting options ensure a consistent and readable INCAR file, which allows for easier comparison of settings between simulations and reduces the chance of error.

The `common` submodule contains variables used for formatting and error checking the INCAR files, including two dictionaries, `AllowedFlagValues` and `FlagDependencies`, and an ordered tuple, `FlagHeaders`. `FlagHeaders` contains the text for each header written for verbose INCAR files, along with the set of INCAR flags belonging to that header. Flags not categorized by `FlagHeaders` are written under a miscellaneous header at the bottom of the file. `FlagDependencies` is a dictionary of INCAR flags with dependent flags, which is used to determine the indenting when writing an INCAR file. Finally, `AllowedFlagValues` is a dictionary of all documented INCAR variables, the types (string, float, etc.) of their values, and a set of allowed values if applicable (set to `None` if any variable of the appropriate type is allowed). The `error` submodule uses the `AllowedFlagValues` dictionary to ensure that any change in the INCAR settings is valid for a VASP simulation, which protects against user error. The variables contained in the `common` submodule are formatted with human modification in mind, so they are easy to read, edit, and append to. If an INCAR flag is not found in the `AllowedFlagValues` dictionary, it is not subject to error checking; this allows the user to use new or obscure INCAR variables without having to modify the

SSST code.

The `incar` module makes it easy to import, modify, and write INCAR files using Python scripts. The difficult work of parsing, converting variables, and formatting output is all handled under the hood, so the user only has to import an INCAR file and add or remove variables as needed.

3.8.5 The system Module

The `system` module is the most generalized way of manipulating VASP input files with SSST. It contains three submodules: `readWrite`, `common`, and `error`. The `error` submodule contains a special error class, `SystemError`, which is used to raise an exception for errors specific to the `system` module. It also contains a function which checks the consistency of all four VASP input files together, including cross-consistency, to ensure that they are properly formatted and configured for VASP. The `common` submodule contains common functions used by the other submodules, such as a function which returns the SSST directory itself.

The `system.readWrite` submodule is the most useful module for the average user. It contains the `SystemData` class, which contains metadata about the input data for a VASP system (such as the system directory, POTCAR library directory, and an optional path for an associated job file for high-performance computing systems). The `SystemData` class may contain subclasses (`PoscarData`, `PotcarData`, `KpointsData`, and `IncarData`) for each input file, depending on what files are imported. All of the functionality of those subclasses is implicitly available to the `SystemData` class. In addition, the `SystemData` class has methods which analyze or modify multiple VASP input files at once. These methods are summarized in Table 3.5.

Each of these modules and submodules is written to be simple to update and build upon. Already, other group members have contributed to SSST: Preston Bowes and Brian Behrhorst have written new methods in the modules, as well as Python scripts which use the SSST library; and Jonathon Baker has also written Python scripts using the library. I have used the SSST for rapidly setting up defect simulations, band structure calculations, and sets of simulations for computing optical properties. I have also used the SSST to analyze the geometries of bulk and defect systems (nearest neighbor tables, average bond lengths, interstitial sites, etc.). It is easy to imagine new uses and additions which might be made in the future. For example, it would be relatively straightforward to write methods for

Table 3.5 Methods of the `SystemData` class. These functions are used to modify or analyze the information contained in multiple VASP input files at once. Function inputs other than `self` are listed beneath each function, along with the variable type and a short description.

Function	Description
<code>__init__</code>	Initialize <code>SystemData</code> object from files
<code>SYSTEM</code> (str)	Path to parent directory
<code>POTCAR_DIR</code> (str)	Path POTCAR library
<code>POSCAR</code> (str)	Relative path to imported POSCAR file
<code>POTCAR</code> (str)	Relative path to imported POTCAR file
<code>KPOINTS</code> (str)	Relative path to imported KPOINTS file
<code>INCAR</code> (str)	Relative path to imported INCAR file
<code>setJobFile</code>	Link a job submission script to the system
<code>JOBFILE_IN</code> (str)	Path to job submission script
<code>JOBFILE_OUT</code> (str)	Job file name when written with the system
<code>writeSystem</code>	Write system data to VASP input files
<code>WRITE_DIR</code> (str)	Path to output directory
<code>renameSystem</code>	Change POSCAR and INCAR headers
<code>NAME</code> (str)	String to be written in the headers
<code>labelAtomsWithPotcar</code>	Use POTCAR atom labels for POSCAR
<code>addDefect</code>	Insert a point defect
<code>TYPE</code> (int)	0=Vacancy, 1=Substitutional, 2=Interstitial
<code>SITE</code> (list, float) or (tuple, int)	Defect coordinate or site indices
<code>DX_SHIFT</code> (list, float)	Displacement vector for DX defects
<code>SPECIES</code> (str)	String specifying POTCAR subdirectory
<code>getNElect</code>	Return number of electrons of neutral system
<code>getSystemCharge</code>	Return the net system charge
<code>chargeSystem</code>	Set the net system charge
<code>CHARGE</code> (int)	Desired system charge (relative to neutral)
<code>setupBandStructureCalculation</code>	Set up a band structure simulation from bulk
<code>LineVertices</code> (list, list, float)	List of coordinates for path in k-space
<code>LineDensity</code> (int)	Number of points along paths in k-space
<code>NBANDS</code> (int)	Set NBANDS in <code>IncarDict</code> (optional)
<code>MODE</code> (str)	Use 'HSE' or 'PBE', depending on functional
<code>LORBIT</code> (int)	Set LORBIT in <code>IncarDict</code> (optional)
<code>ISMEAR</code> (float)	Set ISMEAR in <code>IncarDict</code> (optional)

constructing surface and interface simulations from existing bulk simulations, which could then be used in an automation script for rapid setup and analysis. The SSST has enabled us to automate setup tasks which are otherwise time-consuming, tedious, and error-prone. In

the next subsection, I will discuss how the SSST can be used with Python scripts in order to automate relatively complicated tasks, by way of an example commonly used in our group: setting up defect simulations.

3.8.6 Using the SSST for Defect Simulations

Finally, we will tie the functionality of the SSST together in an example script, called `addDefect.py`. Our group has used `addDefect.py` to rapidly set up hundreds of defect simulations with different geometries and charge states. Before I wrote the SSST, I would spend days of work setting up and verifying even just a few defect simulations. For each defect, one must identify a defect coordinate in the corresponding bulk cell, insert the defect coordinate (and remove atoms on substitutional sites, if necessary), update all of the formatting in the POSCAR file appropriately, generate a new POTCAR file from the appropriate library (if the defect is an impurity), and update the INCAR settings to ensure that relaxation is allowed and a local potential file will be output for the image charge correction (along with any other arbitrary settings one may wish to apply). For charged defects, one must determine the number of electrons in a neutral system by using information from the POSCAR and POTCAR files combined, and then charge the system by setting the appropriate number of electrons in the INCAR file. To define a relaxation sphere (a shell within which atoms are allowed to relax, and outside of which atoms are frozen), one must manually identify the coordinates of atoms within the relaxation sphere and set their selective dynamics flags to `True` in the POSCAR file (bearing in mind that distance computations are more complicated in periodic cells with arbitrary lattice vectors). For DX defects (i.e. defects which are slightly displaced from an ideal substitutional site), one must determine a displacement vector in direct coordinates and add it to the defect coordinate.

It is easy to see how tedious this process would be. Before the SSST, a number of setup errors were common to everyone in the group: accidentally using a POTCAR from the wrong library, forgetting to delete an atom from a substitutional site, forgetting to update the number of atoms or atom labels in the POSCAR file, forgetting to turn on ionic relaxation in the INCAR file (or any number of other desired settings), specifying the wrong number of electrons for a given charge state, and even inconsistent naming and organization. These errors are easy to make when setting up dozens of simulations by hand, and they are often difficult to diagnose (even worse, they may go unnoticed).

The `addDefect.py` script mitigates the error and speeds up the process of setting up

defect simulations. In a separate input file, the user specifies paths to a POTCAR library, a job file, a bulk simulation, and a parent directory for defect simulations. The defect type (vacancy, substitutional, interstitial, or polaron) is specified by an integer (or a list of integers for defect complexes), POTCAR files for impurities are specified by strings, and defect sites are specified by a coordinate vector or a pair of site indices. The user also specifies a DX displacement vector, a radius for a relaxation sphere, and a list of charge states for charged defects. Finally, any desired INCAR settings are specified by a list of tuples with `IncarDict` keys and values. When the `addDefect.py` script is run with the input file, it automatically creates the specified defect simulation from the corresponding bulk simulation, and writes it to the defect parent directory with simulations of different charge states as subdirectories. All of the file reading, data manipulation, and file writing is handled under the hood by SSST modules. Thanks to the SSST library, the `addDefect.py` script itself is very minimal (under 100 lines, half of which are comments and blank spaces; most of the code is devoted to parsing different input options).

Most of the settings don't change, so the user only needs to minimally edit the input file to create new defects. For instance, once a Si_{Al} defect has been set up in a range of charge states, one only has to change the defect species in the input file and run the script again to create any Al-substitutional defect. The process of creating arbitrarily many substitutional defects in arbitrarily many charge states has been reduced from days to minutes.

Although this semi-automated approach allows for the most flexibility, it is possible to automate this process even further with additional scripts. Thus the SSST opens the possibility of any number of automation scripts for VASP setup and analysis. This in combination with our defects database has allowed our group to focus less on technical details and human error, and more on the physics and chemistry of the materials we simulate.

CHAPTER

4

OXYGEN AND SILICON POINT DEFECTS IN $\text{Al}_{0.65}\text{Ga}_{0.35}\text{N}$

Reproduced from *Physical Review Materials* **3**, 054604 (2019), with the permission of the American Physical Society.[Har19] Contributing authors: Joshua S. Harris, Benjamin E. Gaddy, Ramón Collazo, Zlatko Sitar, and Douglas L. Irving. ©2019 American Physical Society.

The formation energies of oxygen and silicon impurities have been examined explicitly in $\text{Al}_{0.65}\text{Ga}_{0.35}\text{N}$ using hybrid exchange-correlation density functional theory simulations. Both impurities were initialized in on-site substitutional and off-site DX configurations in a range of charge states. The O_{N}^{+1} donor was found to always relax into an on-site configuration, and its formation energy is relatively independent of local chemistry (the configuration of Al and Ga atoms surrounding the defect). By contrast, the O_{N}^{-1} acceptor almost always relaxes into a DX configuration, with a formation energy that is strongly dependent on local chemistry. The differences in formation energy of distinct O_{N}^{-1} defect configurations are understood through the interplay of two qualitative trends in the types of nearest-neighbor

bonds (O-Al or O-Ga), as well as the subtler influence of the lengths of the O-Al bonds. Knowledge of O_N^{-1} formation energies as well as the relative frequencies of sites with different local chemistry allows one to compute the relative site occupancies of O_N^{-1} . Because the thermodynamic transition levels associated with different defect configurations are unique, the O_N DX transition is associated with multiple defect levels. Si_{III} , where III represents the group III cation of Al or Ga, provides an interesting counterexample. Si_{III}^{+1} is predicted to be the dominant charge state across the entire bandgap of $Al_{0.65}Ga_{0.35}N$, and little dependence of the formation energy on the composition of nearby cation sites was found. This is explained by the fact that the first-nearest neighbors are all of the same species (N), so the local environment is similar to a bulk III-nitride, in which on-site Si_{III}^{+1} is stable across the same Fermi level range (i.e. below the bandgap of $Al_{0.65}Ga_{0.35}N$). Thus, the trends in the energetics of O_N and Si_{III} in $Al_{0.65}Ga_{0.35}N$ are both determined by the chemistry of the four nearest-neighbor sites surrounding the defect site.

4.1 Introduction

Due to its direct tunable bandgap, aluminum gallium nitride ($Al_xGa_{1-x}N$) is an attractive material for deep ultraviolet light sources such as light emitting diodes and laser diodes, with applications ranging from sterilization to photolithography.[Gra11c; Xie13] In addition to its applications in optoelectronics, $Al_xGa_{1-x}N$ is also a candidate material for next-generation power electronics because of its substantial Baliga figure of merit.[Tsa17] Al-rich AlGaN is of particular interest due to its low lattice mismatch and dislocation density when grown on AlN single crystal substrates versus heterogenous growth on non-native substrates.[Dal11; Bic10] Such high quality films are essential for achieving the conductivities and optical efficiencies necessary for UVC optoelectronic devices.[Bry18] Equally essential is the control of electrical properties via doping. The distribution of point defects can be engineered during growth via various routes, such as chemical potential control[Red17] or Fermi level control[Bry14; Red16]. Each of these routes requires a detailed understanding of the energetics of relevant point defects, which ultimately determines how defect populations will respond when a control parameter is varied. This study uses the hybrid exchange-correlation functionals within the first principles density functional theory (DFT) framework to understand the defect energetics of oxygen (a common unintentional impurity) and silicon (a common intentional dopant) in Al-rich AlGaN. Rather than interpolating the behavior of the defects

from the end members, explicit modeling of point defects in a pseudorandom $\text{Al}_{0.65}\text{Ga}_{0.35}\text{N}$ alloy supercell is performed and compared to previous work. Before the findings are addressed, we will briefly review previous experimental and computational work on oxygen and silicon impurities in AlN, GaN, and AlGaN alloys in the following two subsections.

4.1.1 Oxygen Defects in AlGaN

Oxygen is a commonly observed unintentional impurity in GaN, AlN, and AlGaN. In GaN and Ga-rich AlGaN, O substitutes directly on the N site and acts as a hydrogenic donor at all Fermi levels below the conduction band minimum (CBM). However, at high Fermi levels in AlN and Al-rich AlGaN, O forms compensating DX centers.[McC98; McC99; Sol10; Sol11b] A DX center is a substitutional defect in which the impurity is displaced away from the regular on-site geometry while at the same time localizing additional electrons at the defect site.[Mor86] In this displaced configuration, O_N behaves as a compensating acceptor rather than a donor, thereby limiting its effectiveness as an n-type dopant.

Many computational studies have explored the properties of oxygen impurities in AlN.[SW98; Sta99; SW02; Sil12; MN97; Wal98b; PC97; Wal98a; Gor14; Har18] Park and Chadi calculated formation energies for O in GaN and AlN in an on-site configuration and two different DX configurations, and used linear interpolation to predict the onset of the DX transition level at 20 at% Al in the alloy.[PC97] That study used functionals with the local density approximation (LDA), which is known to underestimate bandgaps and, in turn, can affect the accuracy of formation energy calculations. The more recent study by Gordon *et al.* uses hybrid functionals (which more accurately reproduce the bandgaps of many materials, including GaN and AlN) to model O in GaN and AlN.[Gor14] It was found that O is solely a donor in GaN, but it forms a DX defect in AlN. Through interpolation (including the effects of bandgap bowing), the authors predict the onset of the O DX transition in the alloy at a composition of 61 at% Al.

There is some disagreement in the literature over which DX configuration is the most stable for O in AlN. Earlier studies based on LDA functionals conclude that the most stable configuration involves a displacement of the oxygen away from the N site along the c-axis, such that the axial bond is broken.[PC97; Wal98a] However, Gordon's work, based on hybrid functionals, finds another configuration to be more stable, in which the O atom has been displaced such that one of the three non-axial bonds is broken.[Gor14]

Note that none of these studies explicitly models the O defect in an AlGaN alloy envi-

ronment. Those that draw conclusions about AlGa_xN do so by interpolating between results in GaN and AlN. In fact, only one study, by Bogusławski and Bernholc, does any explicit modeling of point defects in AlGa_xN alloy; but they model C, Si, and Ge.[BB97]

4.1.2 Silicon Defects in AlGa_xN

Silicon is commonly used as an intentional n-type dopant in AlN, GaN, and AlGa_xN alloys. Although it substitutes on the cation site, the silicon impurity has many characteristics which make it an interesting parallel to the oxygen impurity in AlGa_xN. Like O, Si acts as a hydrogenic donor in GaN and Ga-rich AlGa_xN.[Gor14] Also like O, Si transitions to a DX configuration at high Fermi levels in AlN, but not in GaN, indicating that the onset of DX behavior in Al_xGa_{1-x}N is above some threshold Al content.[Gor14] This is supported by experimental measurements of a deeper donor level in Si-doped samples, which has been associated with the DX transition.[Col11; Zei00; Goe01; Son11; Ski99; McC99] However, this DX transition is shallower in the bandgap of AlN for Si than for O.[McC99] Theoretical predictions of this onset Al content vary widely, including $x = 0.24$ [PC97], $x = 0.6$ [BB97], and $x = 0.94$ [Gor14]. Of these predictions, that of Gordon *et al.* ($x = 0.94$) is based on hybrid functionals, which have demonstrated increased accuracy in predicting these properties as compared to traditional functionals. Experimentally, Collazo *et al.* observed a sharp increase in donor activation energy for Si-doped Al_xGa_{1-x}N at $x = 0.8$, which could, in part, be due to the onset of a DX transition.[Col11]

4.1.3 Overview

In this paper, the nature of oxygen and silicon point defects in Al_{0.65}Ga_{0.35}N are examined via explicit modeling of their properties in various configurations in pseudorandom alloy supercells of the alloy. A number of interesting results are revealed that were only elucidated upon explicit simulation of the alloy.

The O_N⁺¹ donor is always found to relax into an on-site configuration, with a formation energy which is relatively independent of local chemistry (the configuration of Al and Ga atoms surrounding the defects). By contrast, O_N⁻¹ has multiple minima in different off-site DX configurations. The formation energies associated with distinct configurations of O_N⁻¹ are principally determined by local chemistry, through the interplay of qualitative trends in nearest-neighbor bonding. These differences in formation energy also lead to multiple

thermodynamic transition levels associated with different configurations of O_N^{-1} and its nearest-neighbor cations. However, it is demonstrated that only two of these thermodynamic transition levels are relevant in realistic situations, owing to the relative populations of O_N^{-1} defects in different configurations.

Si_{III} is predicted to be a singly ionized donor across the entire bandgap for this alloy composition, with little dependence on the composition of nearby cation sites. This is because the first-nearest neighbors of Si_{III} are all the same species (N), so the local chemical environment is similar to a bulk III-nitride (with lattice constants between those of AlN and GaN), in which on-site Si_{III}^{+1} is stable. Therefore the energetics of O_N and Si_{III} in $Al_{0.65}Ga_{0.35}N$ are both determined by the chemistry of the four nearest-neighbor sites surrounding the defect site.

4.2 Methods

4.2.1 Computational Details

All DFT calculations were carried out within the Vienna *Ab initio* Simulation Package (VASP 5.3).[KF96a; KF96b; KH94; KH93] The hybrid exchange-correlation functional of Heyd, Scuseria, and Ernzerhof (HSE), which includes a fraction of short-range exact Hartree-Fock exchange, was used in the calculations of defect properties in $Al_{0.65}Ga_{0.35}N$. [Hey06; Hey03] Owing to the high Al content of the AlGaN alloys studied here, the fraction of exact exchange was set to $\alpha = 0.32$, which reproduced the bandgap of AlN from experiment while simultaneously improving structural parameters and thermodynamic quantities.[Col12] In previous studies, HSE functionals have been used to predict the defect formation energies and concentrations of point defects and complexes in InN, GaN, and AlN.[Gor14; Gad14; Gad13; Lyo14; Lyo10; Col12; Sil12; Har18].

To approximate a random solid solution, 31 Al and 17 Ga atoms were pseudorandomly distributed on the cation sublattice of a wurtzite cell to create five unique 96-atom AlGaN supercells. Note that this actually corresponds to $Al_{0.646}Ga_{0.354}N$, but we will continue to refer to the composition as $Al_{0.65}Ga_{0.35}N$ throughout this paper. A $2 \times 2 \times 2$ k-point mesh and a kinetic energy cutoff of 500 eV were used for all defect calculations. Pseudopotentials were used to represent Al, Ga, N, O, and Si with 3, 3, 5, 6, and 4 explicitly modeled electrons, respectively.

Formation energies were calculated using the grand canonical formalism.[WN04; Fre14] In this formalism, the formation energy of a point defect D^q , where q is the charge state, is given by

$$E_{D^q}^f = E_{D^q}^{\text{tot}} - E_{\text{bulk}}^{\text{tot}} - \sum_i n_i \mu_i + q [\mu_e + E_v] + E_{D^q}^{\text{corr}} \quad (4.1)$$

In this expression, $E_{D^q}^{\text{tot}}$ and $E_{\text{bulk}}^{\text{tot}}$ are the total energies, respectively, of a supercell containing defect D^q and of the corresponding bulk supercell, as calculated with DFT simulations. $E_{D^q}^{\text{corr}}$ is a post-processing correction to the energy of the defect cell, which accounts for finite-size effects in charged supercells (including image charge interactions and a potential alignment with the bulk); here, a custom variation on the method of Kumagai and Oba has been used to obtain the correction.[KO14] For the correction, a relative permittivity of 9.34 was used, being an interpolation between experimental permittivities of 9.70 and 9.14 for GaN and AlN, respectively.[Lev01; Col67] μ_i is the chemical potential of species i , and n_i is the number of atoms of species i exchanged between the bulk and a chemical reservoir in order to create the defect. E_v is the valence band maximum (VBM), and μ_e is the Fermi level relative to the VBM.

Data from defect formation energy calculations is typically represented with a formation energy diagram, in which defect formation energies are plotted as a function of the Fermi level. For plotting purposes, the Fermi level is treated as a free parameter which varies across the bandgap. In such a plot, the charge state of a defect is represented by the slope of the line representing its formation energy. Higher-energy charge states at a given Fermi level do not occur in appreciable concentrations; thus they are often omitted from the figure in order to reduce clutter. The Fermi level at which two charge states of a given defect have equal formation energies (i.e. where the slope changes) is known as the thermodynamic transition level between those two states. Thermodynamic transition levels may be thought of as defect states as represented on a vertical band diagram.

The concentration of a defect D^q is related to its defect formation energy via

$$[D^q] = N_{D^q}^{\text{conf}} N_{D^q}^{\text{site}} \exp\left(-\frac{E_{D^q}^f}{kT}\right) \quad (4.2)$$

such that a lower formation energy results in an exponentially higher defect concentration. In this expression, $N_{D^q}^{\text{conf}}$ is the number of configurations of defect D^q , $N_{D^q}^{\text{site}}$ is the site density of the site on which D^q sits, k is Boltzmann's constant, and T is temperature. In principle,

one can solve for the concentrations of all defects in a system (in a given environment) by solving for the Fermi level at which the charge balance condition is satisfied.[Gad13; Bak17; Bow18a; Bak18c; Sac15]

4.2.2 Defect Geometries in $\text{Al}_{0.65}\text{Ga}_{0.35}\text{N}$

In a wurtzite crystal, an impurity can sit on either sublattice substitutionally or it can be displaced off the sublattice site. Figure 4.1 illustrates each of these possible configurations in the alloy with visualizations produced with VESTA.[MI11] An on-site defect sits directly on the site of the atom for which it substitutes, which is tetrahedrally coordinated to four atoms of the opposite type of the removed atom. A DX defect is displaced slightly off-site towards one of the faces of the tetrahedron, so that it sits approximately between the three atoms defining that face. In a DX-c configuration, the defect is displaced along the c-axis and sits on the tetrahedron face that is normal to the c-axis. In a DX-a configuration, the defect is displaced roughly perpendicular to the c-axis (approximately in the a-plane) and sits on one of the other three faces of the tetrahedron. In a pure wurtzite crystal of the end members, the cation sites are identical, which makes the three DX- a_i configurations symmetrically equivalent.

Substitutional defects in AlGaN are complicated by the fact that the alloy chemistry destroys the wurtzite symmetry because of the random cation site occupancy. For N-site defects in particular, the three DX- a_i configurations are no longer necessarily equivalent when looking at first-nearest neighbor chemistry, depending on which cations occupy the surrounding sites. However, this does not mean that there are no symmetrical configurations from a first-nearest neighbor perspective in the alloy. For instance, in Figure 4.1, one can observe that the DX- a_2 and DX- a_3 configurations are equivalent because in both cases the defect is displaced away from a Ga atom and towards a tetrahedron face containing 2 Al atoms and 1 Ga atom; but the DX- a_1 configuration is not equivalent to these two, since the defect is displaced away from an Al atom and towards the face containing 1 Al atom and 2 Ga atoms. As a result, discussion of defects and their distortions in an alloy requires keeping track of the local chemical configurations. To facilitate this discussion and analysis, we have established a shorthand language to capture aspects of the local chemistry in these systems.

For this purpose, the term *site coordination* (SC) will be used to denote the chemistry of the 4 atoms comprising the coordination tetrahedron around the nitrogen substitutional

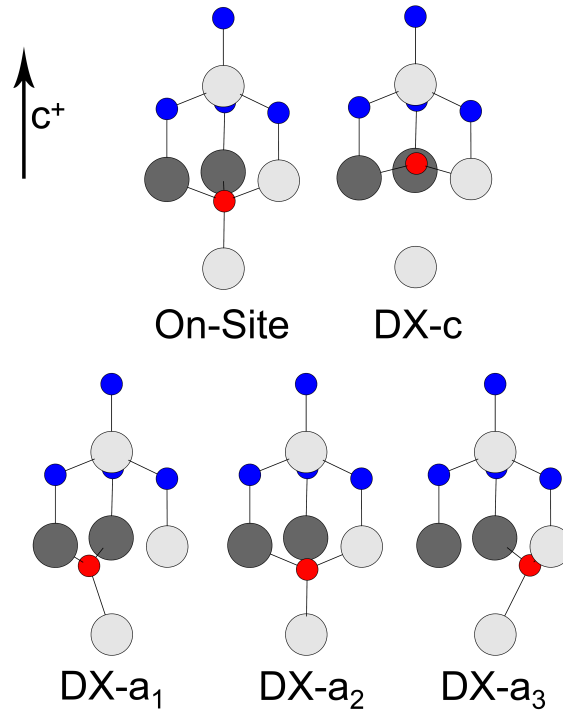


Figure 4.1 Nitrogen-substitutional defect configurations in AlGaN. Light gray and dark gray spheres represent Al and Ga sites, respectively; blue spheres represent nitrogen sites; and the red sphere represents a N-substitutional defect.

site. For instance, each defect configuration shown in Figure 4.1 is in a 2-Al SC (or 2-SC), because the coordination tetrahedron is made of 2 Al and 2 Ga atoms. The term *face coordination* (FC) will be used to denote the chemistry of the 3 atoms comprising the tetrahedron face onto which a DX defect relaxes. For instance, in Figure 4.1, the defects in the DX-c and DX-a₁ configurations are in a 1-Al FC (or 1-FC), because they sit on a face containing 1 Al and 2 Ga atoms; whereas the defects in the DX-a₂ and DX-a₃ configurations are in a 2-FC, because they sit on a face containing 2 Al and 1 Ga atoms. Furthermore, as in the examples given above, both the *site coordination* and the *face coordination* will always be specified by the number of Al atoms, with the remaining atoms being Ga. This terminology will aid the discussion of trends in the alloy, as the influence of defect configuration and local chemistry on the formation energies of O and Si defects in Al_{0.65}Ga_{0.35}N is examined.

4.3 Results and Discussion

4.3.1 Bulk $\text{Al}_{0.65}\text{Ga}_{0.35}\text{N}$ Simulations

To justify the use of pseudorandomly distributed cations in a 96-atom cell, a few key bulk properties were calculated for each of the five bulk configurations. The 0 K formation enthalpy of $\text{Al}_{0.65}\text{Ga}_{0.35}\text{N}$ was found to be -2.66 eV on average with a standard deviation of only 0.03 eV. The average bandgap was 5.09 eV with a standard deviation of 0.03 eV, and the standard deviation in the energy of the valence band maximum was 0.01 eV. The a and c lattice parameters were 3.13 Å and 5.05 Å, respectively, with standard deviations less than 0.001 Å. The small amount of scatter in these bulk properties suggests that the different configurations are representative of the properties of the same random alloy. Furthermore, the small scatter in the enthalpy demonstrates an invariance of the energy to different chemical configurations, which is consistent with the formation of a random solid solution, as is found experimentally in this alloy.

Table 4.1 Calculated bulk lattice parameters and bond lengths in GaN, AlN, and $\text{Al}_{0.65}\text{Ga}_{0.35}\text{N}$. Bond lengths are averaged over a 96-atom cell, which results in standard deviations smaller than 0.01 Å in all cases.

	GaN	AlN	$\text{Al}_{0.65}\text{Ga}_{0.35}\text{N}$
a (Å)	3.18	3.10	3.13
c (Å)	5.16	4.96	5.05
N-Ga Bond (Å)	1.94	–	1.95
N-Al Bond (Å)	–	1.89	1.89

Table 4.1 presents bulk lattice parameters and bond lengths as calculated in GaN, AlN, and $\text{Al}_{0.65}\text{Ga}_{0.35}\text{N}$. Bond lengths have been averaged over a 96-atom cell, resulting in standard deviations smaller than 0.01 Å in all cases. The a and c lattice parameters for $\text{Al}_{0.65}\text{Ga}_{0.35}\text{N}$ are close to the values one would expect by linearly interpolating between the a and c lattice parameters for GaN and AlN (i.e. the lattice parameters follow Vegard's Law, as expected).

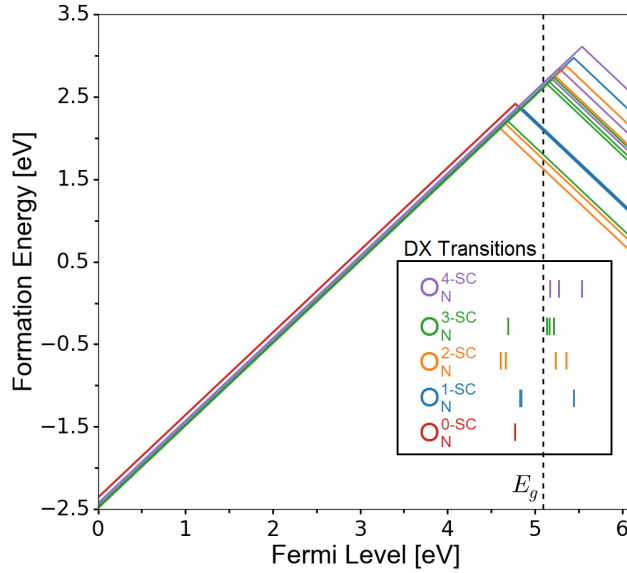


Figure 4.2 Formation energy diagram for O_N in $Al_{0.65}Ga_{0.35}N$. Each of the different colors represents a unique *site coordination*, as labeled in the inset. All configurations of O_N^{-1} are represented on the plot. The Fermi level has been extended above bandgap (5.09 eV, marked by a vertical dashed line) to the bandgap of AlN (6.1 eV), for illustrative purposes. The markers in the inset indicate $O_N(+|-)$ transition levels associated with different O_N^{-1} configurations in each SC.

4.3.2 Oxygen in $Al_{0.65}Ga_{0.35}N$

A N-site substitutional defect in $Al_{0.65}Ga_{0.35}N$ is tetrahedrally coordinated to four cation sites, and may therefore exist in one of five *site coordinations* (0-SC to 4-SC). In each SC, each of the five configurations (on-site, DX-c, DX- a_i) shown in Figure 4.1 must be explored. Thus, each charge state of O_N was modeled in five starting configurations in five SCs, for a total of 25 simulations per charge state. Although the computational expense is clearly high for defect simulations in an alloy environment, such explicit simulations allow a level of physical insight that is otherwise unavailable.

Figure 6.6 is a plot of O_N formation energies versus Fermi level. Note that the Fermi level in the plot extends above the bandgap of $Al_{0.65}Ga_{0.35}N$ (5.09 eV), up to the bandgap of AlN (6.1 eV). Each line color represents a unique SC. The formation energies of neutral O_N^0 in a given SC were found to be roughly independent of configuration (within about 0.1 eV). However, in all SCs and Fermi levels within the bandgap, every configuration of O_N^0 was found to be unstable relative to other charge states, so they have been omitted from the

plot.

Regardless of the initial configuration, the O_N^{+1} donor defect always relaxes to an on-site configuration in all SCs (that is, the DX configurations are not local minima of the total energy for O_N^{+1}). This is reflected in Figure 6.6, where one observes a single line for the formation energy of (on-site) O_N^{+1} for each SC. Furthermore, the formation energy of O_N^{+1} is nearly independent of the SC, so that the five plotted lines for O_N^{+1} in Figure 6.6 almost coincide (the standard deviation is only 0.03 eV).

By contrast, the on-site configuration of the O_N^{-1} acceptor defect is a local minimum only in the 4-SC. Additionally, each of the four possible DX configurations depicted in Figure 4.1 exhibit minima for O_N^{-1} in all SCs and FCs. In Figure 6.6, the formation energies of all configurations of O_N^{-1} that exhibit a minimum are represented, in order to showcase the high variability of their formation energies. Additionally, the $O_N(+|-)$ thermodynamic (DX) transition levels associated with each O_N^{-1} configuration have been marked on the plot within the inset.

In the subsections below, we will identify the mechanisms behind the observed variability of formation energies and DX transition levels. First, we will discuss 4-SC O_N^{-1} as a special case; then we will discuss the influence of bonding and local chemistry variations on the formation energy of O_N^{-1} ; then the influence of bond lengths; and finally, we will discuss the impact of this variability on thermodynamic transition levels and fractional occupancies of different sites. We will find that the formation energy of O_N^{-1} in $Al_{0.65}Ga_{0.35}N$ is mostly determined by the local chemical environment, i.e. the chemical constituency of the four nearest-neighbor cation sites surrounding the N site on which O_N^{-1} substitutes.

4.3.2.1 4-SC O_N^{-1}

A 4-SC N-site defect is completely surrounded by Al, so it is reasonable to expect it to behave similarly to a corresponding defect in AlN. As we will elucidate momentarily, the defect energetics of 4-SC O_N^{-1} support this expectation.

In Figure 6.6, one observes three distinct formation energies (and correspondingly, three distinct DX transition levels) associated with 4-SC O_N^{-1} . The most stable (lowest formation energy) is associated with the three DX- a_i configurations, which have roughly identical formation energies. This degeneracy highlights the importance of local chemistry: although the chemical constituencies of cation sites beyond the first nearest neighbors of the defect are randomized and unique for each of the three DX- a_i configurations, the formation

energies are the same, indicating that local chemistry and bonding effects in the FC prevail over any influence from long-range disorder.

The DX-c configuration is higher in formation energy than the DX- a_i configurations by about 0.2 eV. This accords with previous calculations by Gordon *et al.*, who showed that O_N^{-1} in pure AlN preferentially relaxes to a DX- a_i configuration, which has a lower formation energy than the DX-c configuration by approximately 0.2 eV in AlN.[Gor14] Our own calculations of O_N^{-1} formation energies in pure AlN are also in agreement with those of Gordon. Thus the relative energetics of 4-SC O_N^{-1} behave similarly to those in pure AlN; in other words, the local chemistry here dominates the energetics. We will demonstrate that this is true for other SCs and FCs as well.

The on-site configuration of O_N^{-1} is unique to the 4-SC (i.e. it is not a local minimum in other SCs). Just as in AlN, it is less stable than either of the DX configurations. However, the formation energy of the on-site configuration is higher than that of the DX- a_i configurations by about 0.7 eV in $Al_{0.65}Ga_{0.35}N$, whereas the difference is about 0.5 eV in AlN, according to our calculations. Despite the slight difference, this again demonstrates that the local AlN-like environment dominates the relative energetics of 4-SC O_N^{-1} .

Finally, it should be emphasized that while all DX configurations of 4-SC O_N^{-1} exhibit a minimum, none of their associated DX transition levels are within the bandgap (see Figure 6.6). Although this seems to differ from AlN, in which the corresponding defect levels are within the bandgap, the difference is due to the movement of the band edges as a function of Ga content rather than any effect of the local environment on the defect energetics.

4.3.2.2 0-SC to 3-SC O_N^{-1} : Bonding and Local Chemistry

Local chemistry also dominates the energetics of O_N^{-1} in the 0-SC to the 3-SC, but more details are necessary to extract trends due to the local chemistry variations. In Figure 6.6, for 1-SC, 2-SC and 3-SC O_N^{-1} , one observes two distinct groups of formation energies; one group has a DX transition within the bandgap, while in the other group the DX transition occurs above the CBM. The distinct groups correspond to O_N^{-1} configurations in different FCs. The formation energies of 0-SC O_N^{-1} fall into a single degenerate group, because 0-FC is the only possible *face coordination* for the 0-SC. Notably, the DX- a_i and DX-c configurations are degenerate in the 0-SC, which was not the case in the 4-SC.

Table 4.2 contains O_N^{-1} formation energies in different SCs and FCs. The values in the table are all taken relative to the most stable O_N^{-1} defect (2-SC, 2-FC). For locally degenerate

Table 4.2 O_N^{-1} formation energies for all SCs and FCs, relative to the most stable O_N^{-1} defect. Only the lowest formation energy is reported for locally degenerate configurations.

		O_N^{-1} Formation Energies (eV)				
		Site Coordination (n-Al SC)				
		0	1	2	3	4
Face Coordination (n-Al FC)	0	0.47	1.70			
	1		0.46	1.26		
	2			0.00	1.07	
	3				0.17	1.19

configurations (same SC and FC), only the lowest formation energy is given. The values in red text represent higher energy configurations, which incidentally correspond to DX configurations that exhibit thermodynamic transition levels above the CBM. Notice that a given FC (rows) may originate from one of two possible SCs (columns); whereas the 0-SC and 4-SC (columns) only have one possible FC (row).

Two trends in the formation energies are observed in Table 4.2: (1) in a given SC, O_N^{-1} prefers to maximize the number of Al atoms in its FC (i.e. in a given column, the lowest row has the lowest formation energy); and (2) in a given FC, O_N^{-1} prefers to reduce the number of Al atoms in its initial SC (i.e. in a given row, the leftmost column has the lowest formation energy).

These two trends may be qualitatively understood by appealing to a relatively simple bonding picture. To evaluate the energies of the various O_N^{-1} configurations within this model, consider the energy difference between a given DX configuration and its (higher energy) on-site configuration. In the on-site configuration, the defect sits within a tetrahedron of 4 cations, approximately equidistant from each of them with a local chemistry defined by the SC. In a DX configuration, the defect sits approximately on one face of the tetrahedron with a local chemistry defined by the FC. Relative to the on-site configuration, we may say that the DX configuration has strengthened (shortened) three bonds (with the ions forming the tetrahedron face) and broken one bond (with the ion in the remaining

corner of the tetrahedron).

The dissociation energy of Al-O bonds is almost twice that of Ga-O bonds.[Dar70] Therefore, it is reasonable to expect that the energy of a given DX configuration is lower when the three bonds that are strengthened consist of as many Al-O bonds as possible (i.e. it is energetically preferable to form stronger bonds). This expectation corresponds to the first trend: in a given SC, the formation energy of O_N^{-1} is lower when the FC maximizes the number of Al atoms. Likewise, it is reasonable to expect that the energy of a given DX configuration is lower when the broken bond is a Ga-O bond (i.e. it is energetically preferable to break a weaker bond). This second expectation corresponds to the second trend: in a given FC, the formation energy of O_N^{-1} is lower when the SC minimizes the number of Al atoms, i.e. when the atom on the far corner of the coordination tetrahedron is Ga rather than Al.

The interplay of these two trends mostly determines the relative energetics of O_N^{-1} in $Al_{0.65}Ga_{0.35}N$. However, following the trends to their logical conclusion would lead one to predict the most stable defect to be in the 3-SC and 3-FC, which in fact is the second most stable defect (see Table 4.2). Clearly, the two bonding trends alone are not sufficient in themselves to describe the predicted formation energies. In 4.3.2.3, we will discuss the more subtle influence of bond lengths on the defect energetics of O_N^{-1} , and we will demonstrate that the most stable defect represents the best compromise between all three influences.

4.3.2.3 0-SC to 3-SC O_N^{-1} : Bond Lengths and Strengths

The bonding trends discussed in section 4.3.2.2 rely on the assumption that the strengths of Al-O and Ga-O bonds are independent of the local bonding environment (SC and FC). However, an examination of the lengths of these bonds suggests that the bond strength may in fact vary with the SC and FC. Table 4.3 gives the bond lengths between oxygen and its three nearest-neighbor cations for the most stable O_N^{-1} defect in AlN and each SC in $Al_{0.65}Ga_{0.35}N$. All defects represented in the table are in a DX-a configuration, and the three bond lengths in each case are the distances to the FC cations. In the table, highlighted cells correspond to Al-O bonds, while the rest correspond to Ga-O bonds.

In our calculations of O_N^{-1} in the DX-a configuration in AlN, we find the corresponding Al-O bond lengths to be 1.74, 1.82, and 1.82 Å. In experiment, the Al-O tetrahedral bond length averaged over 32 aluminosilicate structures was found to be 1.76 Å with a standard deviation of 0.001 Å [Jon68], and Al-O distances of 1.75 Å were recently measured in ultrathin oxide

Table 4.3 Nearest-neighbor bond lengths for the most stable O_N^{-1} defect in AlN and in each SC in $Al_{0.65}Ga_{0.35}N$. All defects are in the DX-a configuration, and the three bond lengths in each case are the distances to the face-coordinated cations (ordered from shortest to longest, going down each column). Highlighted cells correspond to Al-O bonds, while the rest correspond to Ga-O bonds.

(Ga,Al)-O Bond Lengths (Å) for O_N^{-1}					
AlN	$Al_{0.65}Ga_{0.35}N$ (n-Al SC)				
	0	1	2	3	4
1.74	1.86	1.74	1.75	1.78	1.75
1.82	1.89	1.87	1.78	1.83	1.84
1.82	1.92	1.94	1.99	1.83	1.85

films on on AlN substrates [Dyc18]. The implication is that O_N^{-1} in the DX-a configuration in AlN has one Al-O bond with a nearly ideal length, and two Al-O bonds with longer than ideal lengths. These bond lengths in AlN are comparable to the Al-O bond lengths for 4-SC and 3-SC O_N^{-1} in $Al_{0.65}Ga_{0.35}N$ (the two rightmost columns in Table 4.3), which also feature one bond close to the ideal Al-O bond length and two longer bonds.

By contrast, the Al-O bond lengths for 2-SC (2-FC) O_N^{-1} are both close to the ideal Al-O bond length. As a rule of thumb, shorter bonds are stronger bonds, indicating that the 2-SC has two strong Al-O bonds as opposed to one in the 3-SC. The strengthening of an Al-O bond comes at the expense of weakening the already weaker Ga-O bond. This bond strengthening effect is enough to perturb the bonding trends identified in Section 4.3.2.2, making O_N^{-1} more stable in the 2-SC than in the 3-SC, despite the corresponding change in FC.

4.3.2.4 Thermodynamic Transitions and Fractional Occupancy

In Figure 6.6, one observes many different thermodynamic transitions associated with the varying local chemistry around O_N^{-1} . Because of the low variability in the O_N^{+1} formation energies, differences between the $O_N(+|-)$ thermodynamic (DX) transition levels largely correlate with differences in the O_N^{-1} formation energies. Table 4.4 provides the relative

Table 4.4 Relative formation energies and DX transition levels for the most stable defect configuration in each SC. Formation energies are reported relative to the defect with the lowest formation energy. As in Figure 4.1, light gray and dark gray spheres represent Al and Ga sites, respectively; blue spheres represent nitrogen sites; and the red sphere represents a N-substitutional defect.

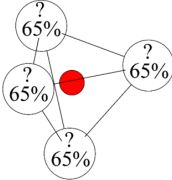
Site Coordination	0	1	2	3	4
ΔH_f^{rel} (eV)	0.47	0.46	0.00	0.17	1.19
E_{therm} (eV)	4.77	4.83	4.60	4.69	5.17

formation energies and DX transition levels for the most stable defect configuration in each SC. Each formation energy in Table 4.4 has a corresponding entry in Table 4.2. Each image in the first row of the table shows the O_N^{-1} defect configuration associated with the data below it. The entries in red (for the 4-SC) indicate that the defect does not exhibit a DX transition level within the bandgap; it is above the CBM (5.09 eV).

In Table 4.4, we can observe the interplay of the two qualitative bonding trends and the bond strengthening effect discussed in the previous two sections. In each SC (table column), the most stable defect has maximized the number of aluminum atoms in its FC, and the remaining (unbonded) corner of the coordination tetrahedron is always a Ga ion where the SC allows it. The most stable defect is found in the 2-SC and 2-FC, representing the best compromise between the two bonding trends and the bond strengthening effect.

It is interesting that all three trends are determined by the local chemistry around the defect site. The composition of the alloy beyond the four nearest-neighbor cation sites seems to play only a second order role in the defect energetics, causing variations of at most 0.1 eV in the formation energies of locally degenerate defect configurations (which is smaller than the thermal energy at typical growth temperatures). In a given SC, only one configuration or set of degenerate configurations is stable. Thus it makes sense to consider the proportion of O_N^{-1} defects in each SC, i.e. the fractional occupancy of sites with different SCs. Fractional site occupancies at a given temperature can be computed with Equation

Table 4.5 Relative site density and O_N^{-1} occupation probability for nitrogen sites in $Al_{0.65}Ga_{0.35}N$ with different *site coordination*. Non-degenerate defect configurations have been taken into account in the calculation of the site occupancies. Thermodynamic transition levels corresponding to Table 4.4 have been reproduced here for easy reference.

Site Coordination (n-Al SC)	Relative Site Density	O_N^{-1} Occupancy at 1400 K	E_{therm} (eV)
	0	0.016	4.77
	1	0.115	4.83
	2	0.800	4.60
	3	0.184	4.69
	4	0.000	5.17

4.2 in conjunction with our data.

Table 4.5 summarizes the results of such a calculation. Here, site density has been defined as the likelihood of choosing a N site with a given SC, if a N site is chosen at random; it is calculated probabilistically, based on the cation stoichiometry. On a site with a given SC, O_N^{-1} may take on multiple configurations, as described above. These configurations have been taken into account in the calculation of fractional site occupancies, but the formation energies of locally degenerate configurations (same SC and FC) have been averaged over the available data in order to minimize the influence of second-order effects.

Table 4.5 reveals that at 1400 K (a common temperature for epitaxial growth by MOCVD [Bry18]) O_N^{-1} will mostly occupy sites with 3-SC or 2-SC. Although sites with 3-SC are more ubiquitous for this composition, O_N^{-1} is more likely to occupy sites with 2-SC because its formation energy is lower in the latter. After quenching to a low temperature, the relative populations of O_N on these sites may remain at their high temperature values if the oxygen ions are kinetically hindered from diffusing to other sites. The thermodynamic transition levels associated with 3-SC and 2-SC are close but not identical (approximately 90 meV apart). We may therefore expect to observe multiple defect levels in the bandgap associated with an $O_N(+|-)$ DX transition, separated by about 90 meV assuming no other defects or defect complexes interfere. This conclusion is uniquely the result of the locally random

environment, and could not have been reached by interpolating between the results of simulations in AlN and GaN.

The relative site densities given in Table 4.5 apply regardless of the total concentration of O_N^{-1} defects, but they may not be measurable unless this concentration is above detection levels. Depending on experimental conditions (chemical potentials and Fermi level), the on-site and DX configurations may not be the only possibilities for oxygen. For example, on-site O_N^{+1} will predominate if the Fermi level and concentration of oxygen are low. The presence of $V_{III}+nO_N$ complexes [Yan14] may also compete with the formation of O_N^{-1} and push it to low concentrations, depending on the Fermi level and chemical potentials. Multi-member complexes would be expected to be more likely when impurity concentrations are high due to their stronger dependence on the chemical potential as compared to the singular defects, as was shown for multi-member silicon-vacancy complexes in AlN. [Har18] With this caveat in mind, the results given in Table 4.5 are relevant to measurement when a significant population of O_N^{-1} defects is present.

4.3.3 Silicon in $Al_{0.65}Ga_{0.35}N$

In AlN, oxygen forms an anion-site substitutional donor which exhibits a DX transition approximately 550 meV below the CBM. Silicon in AlN forms a cation-site substitutional donor which exhibits a DX transition approximately 200 meV below the CBM. Such a comparison of these two defects reveals that Si_{III} provides an interesting counterexample to O_N in AlGaN, where III refers to the general cation site (Al or Ga).

Figure 4.3 is a formation energy diagram for Si_{III} in $Al_{0.65}Ga_{0.35}N$. As in Figure 6.6, the Fermi level in the plot extends above the bandgap of $Al_{0.65}Ga_{0.35}N$ (5.09 eV), up to the bandgap of AlN (6.1 eV). Both cation-site substitutional defects, Si_{Ga} and Si_{Al} , exhibit the same type of behavior and have a dependence on the Al or Ga chemical potentials. For simplicity, we have defined the cation chemical potentials such that Si_{Ga} and Si_{Al} are on equal footing, and we label the (Al or Ga) cation substitutional defect Si_{III} . Each line in Figure 4.3 corresponds to data from a simulation in a unique bulk environment. Because the first nearest neighbors of cation sites are all N atoms, changing the bulk configuration around a cation-site defect only affects the chemistry of second nearest neighbors and beyond.

With all of this in mind, some details in Figure 4.3 are immediately of note. First, there is no DX transition inside the bandgap: Si_{III} is a hydrogenic donor across the entire bandgap

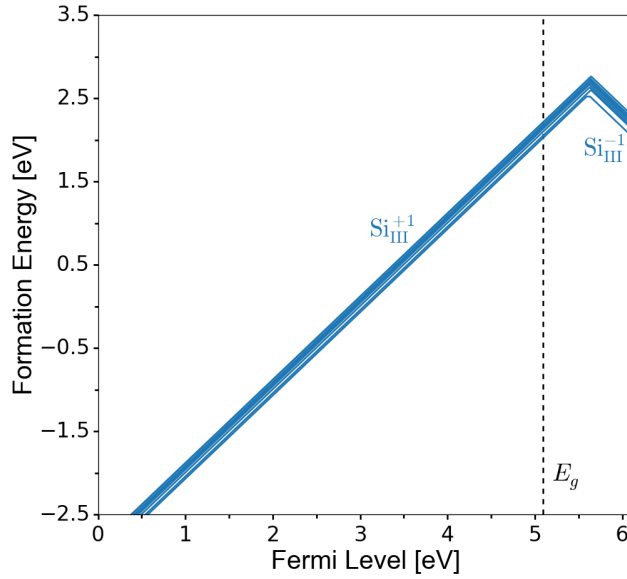


Figure 4.3 Formation energy diagram for Si_{III} , a silicon substitutional on a cation site, in $\text{Al}_{0.65}\text{Ga}_{0.35}\text{N}$. Each line corresponds to data from a simulation in a unique bulk environment (cation configuration). The Fermi level has been extended above bandgap (5.09 eV, marked by a vertical dashed line) to the bandgap of AlN (6.1 eV), for illustrative purposes.

in $\text{Al}_{0.65}\text{Ga}_{0.35}\text{N}$. This agrees with a recent theoretical prediction by Gordon *et al.* (discussed in the introduction) and obtained via interpolation.[Gor14]

The second noteworthy feature is that the formation energies of $\text{Si}_{\text{III}}^{+1}$ and $\text{Si}_{\text{III}}^{-1}$ with different cation configurations are tightly clustered together (they each vary within a range of about 0.25 eV). This is because both charge states energetically prefer an on-site substitutional configuration regardless of the bulk cation configuration. For $\text{Si}_{\text{III}}^{+1}$, the DX- a_i and DX-c configurations are not local minima in the total energy landscape (the same is true of $\text{Si}_{\text{Al}}^{+1}$ in AlN). For $\text{Si}_{\text{III}}^{-1}$, the DX- a_i configurations exhibit minima, but they have higher formation energies than the on-site configurations with the same bulk cation configuration. In AlN, the DX-a configuration of $\text{Si}_{\text{III}}^{-1}$ is actually more energetically favorable than the on-site configuration; however, in GaN, the on-site configuration is more favorable (although neither configuration is stable, nor leads to a thermodynamic transition state, within the bandgap in GaN). This suggests that there is some Al concentration (higher than 65 percent) above which the DX- a_i configurations become favorable, and below which the on-site configuration is favorable. The DX- a_i configurations of $\text{Si}_{\text{III}}^{-1}$ are not represented

in Figure 4.3, since they are unfavorable relative to the on-site configuration. The DX-c configuration of $\text{Si}_{\text{III}}^{-1}$ was not found to exhibit a minimum in GaN, AlN, or $\text{Al}_{0.65}\text{Ga}_{0.35}\text{N}$.

Finally, unlike O_{N} , the (above bandgap) transition levels of Si_{III} exhibit little variability as a function of cation configuration. In fact, because the $\text{Si}_{\text{III}}^{+1}$ and $\text{Si}_{\text{III}}^{-1}$ formation energies exhibit roughly the same variation with cation configuration, the variation of the (+|−) transition levels is about an order of magnitude smaller than the variation in the formation energies. The $\text{Si}_{\text{III}}(+|−)$ transition levels vary within a range of about 0.02 eV, with an average of 5.63 eV. The lone outlier (the configuration with the lowest $\text{Si}_{\text{III}}^{-1}$ formation energy, which features a narrow range of stability for the neutral Si_{III}^0 defect) exhibits a (+|0) transition at 5.59 eV and a (0|−) transition at 5.63 eV.

Above, we have shown that the formation energy for the comparable O_{N}^{-1} defect is predominantly influenced by first-nearest neighbor chemistry, whereas second and higher nearest neighbors play a second-order role. Similarly, the defect energetics of $\text{Si}_{\text{III}}^{+1}$ are also dominated by first nearest neighbors, but because it sits on the cation site, all of the first nearest neighbors are the same species (nitrogen). As a result, the configuration of the surrounding bulk material has little effect on the formation energy of $\text{Si}_{\text{III}}^{+1}$. This helps to illustrate the key role played by local chemistry in the energetics of defects in AlGaN.

It is worth mentioning that second-nearest neighbor chemistry has been found to play a role in the energetics of $\text{Si}_{\text{III}}^{-1}$ in previous work. There is an additional DX configuration of $\text{Si}_{\text{III}}^{-1}$ that exhibits a minimum in which the Si atom sits substitutionally on the cation site, but a N atom is displaced away from its site along the c-axis so that it sits between three cation sites. Bogusławski and Bernholc used explicit alloy modeling to demonstrate that the formation energy of this configuration of $\text{Si}_{\text{III}}^{-1}$ varies within a range of about 0.4 eV depending on whether those cation sites are occupied by Al, Ga, or some combination.[BB97] In our calculations, the formation energies of $\text{Si}_{\text{III}}^{-1}$ in the DX- a_i configurations vary within a range of about 0.14 eV with different cation configurations. In AlN, we found the Bogusławski and Bernholc configuration to be unfavorable relative to the DX-a configuration when simulated with hybrid functionals. Due to the extensive computational cost for the current simulations, as well as the fact that the $\text{Si}_{\text{III}}^{-1}$ configurations are above bandgap for our alloy composition, we did not simulate this DX configuration.

With that said, based on our analysis of oxygen and its dependence on local chemistry, we hypothesize that the configuration of Bogusławski and Bernholc could be more susceptible to second-nearest neighbor chemistry variations. The Al-N and Ga-N bond strengths are

different, and would influence the energy required to displace the N atom. There is already a change in the favorable site for the ionized acceptor going from GaN (on-site) to AlN (DX- a_i) and, without explicit simulation, there is no reason to eliminate this configuration from consideration in Al-rich alloys. If present, the DX configuration of Bogusławski and Bernholc could lead to an increased variation in the formation energies of the favorable acceptor and the associated DX thermodynamic transition levels, possibly on the same order as the variation in O_N formation energies and DX transition levels (0.1-0.2 eV). We would expect this to be most important for Si_{III}^{-1} in AlGaN at higher Al concentrations (above 85 %Al), where the various Si_{III}^{-1} configurations become favorable and the variability of these states may be evident from experimental measurements.

4.4 Conclusion

The point defect energetics of a substitutional oxygen impurity in $Al_{0.65}Ga_{0.35}N$ have been examined in great detail using explicit DFT simulations of O_N in a set of 96-atom pseudorandom alloy supercells. We found that O_N^{+1} always relaxes to an on-site configuration with a formation energy that is relatively independent of the local alloy chemistry around the defect site. O_N^0 can relax into multiple configurations in a given *site coordination* (SC), but they all have similar formation energies and none of them are stable relative to other charge states.

O_N^{-1} generally relaxes into a DX configuration in a given SC, and the relative formation energies of the various possible DX configurations depend on the chemistry of the four nearest-neighbor cation sites. The influence of local chemistry on the formation energy of O_N^{-1} is evident via three qualitative trends: maximizing the number of Al ions in the defect's FC, minimizing the number of Al ions in its SC, and strengthening Al-O bonds over Ga-O bonds in each FC. However, these qualitative rules of thumb are not mutually exclusive, and it is the interplay of all three effects which ultimately determines the favorability of a given O_N^{-1} defect. Second nearest neighbors and beyond play a second-order role in the defect energetics of O_N^{-1} .

Relative site occupancies were calculated based on relative site densities and formation energies of O_N^{-1} in all possible configurations (SCs and FCs). O_N^{-1} was found to preferentially occupy sites with 2-SC, with some probability of occupying sites with 3-SC at reasonable growth temperatures. Because the thermodynamic transition levels associated with these

SCs and FCs are not identical, this leads to the possibility that multiple defect levels associated with an $O_N(+|-)$ DX transition may be observed within the bandgap when this defect is above detection limits.

Finally, we examined Si_{III} as an interesting counterexample. Si_{III}^{+1} was found to be the only stable charge state, with no DX transition predicted inside the bandgap in $Al_{0.65}Ga_{0.35}N$. Si_{III}^{+1} always relaxes to an on-site configuration, regardless of its initial configuration, with little variation of the formation energy as a function of the distribution of second-nearest neighbor cations.

This too is explained by the local chemistry surrounding the defect sites. The defect energetics of O_N^{-1} are dominated by the chemistry of the first-nearest neighbor cations, which can be either Al or Ga. By contrast, the first-nearest neighbors of Si_{III}^{+1} are all N atoms, and therefore the defect behaves as it would in AlN or GaN. Therefore, first-nearest neighbor chemistry dominates the behavior of both of these defects in $Al_{0.65}Ga_{0.35}N$.

4.5 Acknowledgements

The authors acknowledge financial support from the AFOSR grant FA9550-17-1-0225, and computer time from the DoD HPCMP. Dr. Jonathon Baker and Preston Bowes of NCSU, and Dr. Pramod Reddy of Adroit Materials Inc. are thanked for their comments and discussion on the paper.

CHAPTER

5

ON COMPENSATION IN Si-DOPED AlN

Reproduced from *Physical Review Materials* **3**, 054604 (2019), with the permission of AIP publishing.[Har18] Contributing authors: Jonathon N. Baker, Benjamin E. Gaddy, Isaac Bryan, Zachary Bryan, Kelsey J. Mirrielees, Pramod Reddy, Ramón Collazo, Zlatko Sitar, and Douglas L. Irving. ©2019 AIP Publishing LLC.

Controllable n-type doping over wide ranges of carrier concentrations in AlN, or Al-rich AlGa_N, is critical to realizing next generation applications in high-power electronics and deep UV light sources. Silicon is not a hydrogenic donor in AlN as it is in GaN; despite this, carrier concentration should be controllable, albeit less efficiently, by increasing the donor concentration during growth. At low doping levels an increase in Si content leads to a commensurate increase in free electrons. Problematically, this trend does not persist to higher doping levels. In fact, further increases in Si concentration leads to a *decrease* in free electron concentrations; this is commonly referred to as the compensation knee. While the nature of this decrease has been attributed to a variety of compensating defects, the mechanism and identity of the predominant defects associated with the knee have not been

conclusively determined. Density functional theory calculations using hybrid exchange-correlation functionals have identified $V_{\text{Al}} + n\text{Si}_{\text{Al}}$ complexes as central to mechanistically understanding compensation in the high Si limit in AlN while secondary impurities and vacancies tend to dominate compensation in the low Si limit. The formation energies and optical signatures of these defects in AlN are calculated and utilized in a Grand Canonical charge balance solver to identify carrier concentrations as a function of Si content. The results were found to qualitatively reproduce the experimentally observed compensation knee. Furthermore, these calculations predict a shift in the optical emissions present in the high and low doping limits, which is confirmed with detailed photoluminescence measurements.

Aluminum nitride (AlN) and aluminum gallium nitride (AlGaN) are important next-generation materials for high-power electronics and deep UV light sources (light emitting and laser diodes).[Jon15; Xie13; Gra11c; Tsa18] Realization of these applications centers on the ability to controllably dope over a wide range of doping regimes. For example, drift regions in power electronics require low doping ($\sim 10^{15} \text{ cm}^{-3}$) while opto-electronics typically require higher dopant concentrations ($\sim 10^{19} \text{ cm}^{-3}$). Silicon is often preferred for donor doping applications due its hydrogenic nature in gallium nitride (GaN) and Ga-rich AlGaN, enabling well controlled electron populations over a very wide doping regime.[Göt96; Wag03; Pol98; Gor14] Similar behavior might be expected for Si doping in Al-rich AlGaN and AlN. Nevertheless, two issues arise in translating Si to these systems.

First, while Si still prefers the cation site (i.e. $\text{Si}_{\text{Al/Ga}}$), it is no longer a shallow dopant, due to the emergence of a DX transition near the conduction band (CB) edge with increasing Al content. Experimentally, the DX transition has been assigned a wide range of activation energies ranging between 78-345 meV.[Son11; Col11; Zei00; Goe01] First principles methods using hybrid exchange-correlation functionals predict the transition as 150 meV (Gordon[Gor14]) and 200 meV (this work) below the CB edge in AlN. In principle, it should be possible to overcome the higher DX activation energy by doping with more Si, at the cost of lower mobility.

The second issue, however, is that additional doping only yields more carriers in the low doping regime. The carrier concentration actually decreases with additional Si in the high doping regime. The increase and subsequent decrease in carrier concentration as a function of Si content is often referred to as a compensation knee. Several studies have observed a compensation knee in AlGaN with Al content ranging from 60-100 percent.[Chi13; Meh13;

Shi11; Tan02; Bry14; Bry15; Bry18] The mechanism of this knee has been attributed to many factors, which include the DX transition[Meh13], cation vacancies[Tan02], Si_N [Tan02], and cation vacancy-silicon complexes[Chi13; Bry18].

The true knee mechanism, whatever its origin, is deeply tied to how the system achieves charge neutrality. There are many routes to charge neutrality in a wide bandgap material like AlN, and the dominant mechanism depends on the position of the Fermi level and the availability of each species in the growth environment. Many possibilities for defect-related compensation have been explored computationally, including native defects (vacancies, interstitials, etc.), common impurities (C, O, Si-DX), and first-nearest neighbor complexes between Si and C, and between O and cation vacancies.[Gad14; Yan14; Gad13; Gor14; SW02] However, the second-nearest neighbor complexes between Si donors and cation vacancies proposed by Chichibu[Chi13] and more recently by Bryan[Bry18] have not been explored computationally, and the roles played by any of these defects in the compensation knee have not been definitively determined.

We have used state-of-the-art density functional theory (DFT) calculations utilizing hybrid exchange-correlation functionals to develop a model which predicts that $V_{\text{Al}} + n\text{Si}_{\text{Al}}$ complexes are central to forming the compensation knee and to a mechanistic understanding of compensation in the high doping limit of Si in AlN. These defects are consistent with previous experiments that measured high concentrations of cation vacancies observed in n-type AlN and AlGaN,[Ued12; Ued09; SW02] as well as the observation by Taniyasu that the calculated donor concentration is lower than the actual Si concentration in highly doped samples.[Tan02] Furthermore, our DFT calculations predict that the main compensating defect should change in the low and high Si-doping limits and that this should lead to an observable shift in the optical emissions. Detailed photoluminescence (PL) measurements on MOCVD grown AlN samples confirm such a luminescence shift for low and highly Si-doped samples and the DFT predictions are in good agreement with these measurements.

All DFT calculations were carried out in the Vienna *Ab initio* Simulation Package (VASP 5.3.4).[KF96a; KF96b; KH94; KH93] All calculations used the hybrid exchange-correlation functional of Heyd, Scuseria, and Ernzerhof (HSE), with an exact exchange amount of $\alpha = 0.32$, yielding a bandgap of 6.1 eV.[Hey06; Hey03] All defect calculations were carried out in 96-atom supercells with a $2 \times 2 \times 2$ k-point mesh and a 500 eV kinetic energy cutoff.

Formation energies were calculated using the grand canonical formalism.[WN04; Fre14] In this formalism, the formation energy of a point defect D^q , where q is the charge state, is

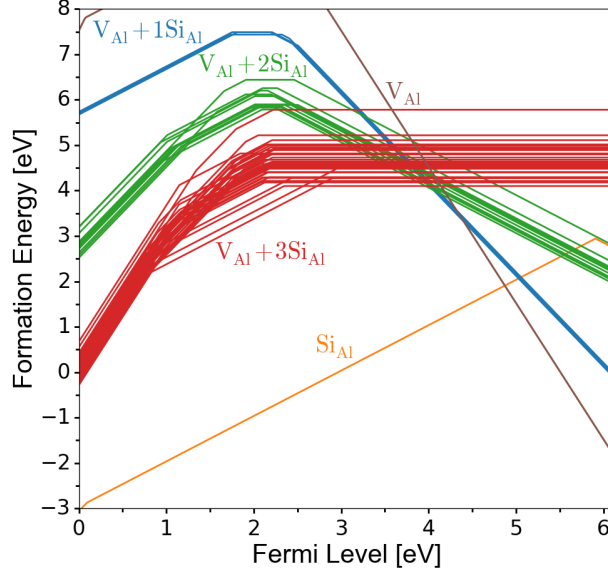


Figure 5.1 Formation energy versus Fermi level for V_{Al} , Si_{Al} , and all geometrically inequivalent configurations of $V_{\text{Al}} + n\text{Si}_{\text{Al}}$ complexes.

given by

$$E_{D^q}^f = E_{D^q}^{\text{tot}} - E_{\text{bulk}}^{\text{tot}} - \sum_i n_i \mu_i + q [\mu_e + E_v] + E_{D^q}^{\text{corr}} \quad (5.1)$$

In this expression, $E_{D^q}^{\text{tot}}$ and $E_{\text{bulk}}^{\text{tot}}$ are the total energies, respectively, of a supercell containing defect D^q and of the corresponding bulk supercell. μ_i is the chemical potential of species i , and n_i is the number of atoms of species i exchanged between the bulk and a chemical reservoir to create the defect. μ_e is the Fermi level relative to the valence band maximum (E_v). $E_{D^q}^{\text{corr}}$ is a *post-hoc* finite-size correction to the energy of the charged defect supercell based on the method of Kumagai,[KO14] using an experimental relative permittivity of 9.14.[Col67] Convergence of the formation energies was found to be on the order of 0.2 eV. The formation energies and optical transitions were calculated for native vacancies; on-site and DX configurations of Si, O, and C impurities; first nearest neighbor (1-NN) complexes for all pairs of defects on their dominant sites; $V_{\text{Al}} + n\text{O}_{\text{N}}$ 1-NN complexes with $n = 1-4$ O atoms surrounding an Al vacancy; $V_{\text{N}} + \text{C}_{\text{N}}$ 2-NN complexes; and $V_{\text{Al}} + n\text{Si}_{\text{Al}}$ 2-NN complexes with $n = 1-3$.

Figure 5.1 is a plot of formation energy versus Fermi level for V_{Al} , Si_{Al} , and $V_{\text{Al}} + n\text{Si}_{\text{Al}}$ complexes. For each defect at each Fermi level, only the most stable charge state is plotted.

The slope on the formation energy plot gives the charge state of the defect. A change of slope in Figure 5.1 corresponds to the Fermi level at which two charge states of a defect are equally stable (i.e. a thermodynamic transition level).

In the silicon-vacancy complexes, the Si impurities sit on Al second nearest neighbor (2-NN) sites to the Al vacancy; there are 12 such 2-NN sites. Thus the $V_{\text{Al}} + 1\text{Si}_{\text{Al}}$ complex has 12 total configurations, 3 of which are unique due to symmetry; $V_{\text{Al}} + 2\text{Si}_{\text{Al}}$ has 66 total configurations, 13 of which are unique; and $V_{\text{Al}} + 3\text{Si}_{\text{Al}}$ has 220 configurations, 42 of which are unique. All symmetrically inequivalent configurations of these complexes were explicitly modeled in all relevant charge states. It is clear from Figure 5.1 that there is a wide spread in formation energies for different configurations of $V_{\text{Al}} + n\text{Si}_{\text{Al}}$ especially as the number of Si atoms in the complex increases. This dispersion in energy is due to electrostatic interactions between the Si impurities in each complex. For instance, the formation energy of neutral $V_{\text{Al}} + 3\text{Si}_{\text{Al}}$ increases approximately linearly as the average Si-Si distance decreases in the configuration. The binding energy of each $V_{\text{Al}} + n\text{Si}_{\text{Al}}$ complex at relevant Fermi levels (relative to V_{Al}^{-3} and $\text{Si}_{\text{Al}}^{+1}$) is greater than 1.5 eV. Regardless of binding energy, the concentration of all species is governed by the formation energy.[WN04; Fre14]

Formation energies provide a route to determine the concentration of impurities, native defects, and complexes for various growth conditions (Al-rich to N-rich). In Figure 5.1, the Fermi level is taken as a free parameter, but its exact position is determined by conditions of charge neutrality (i.e. $n - p = \sum_{i,q} q[D_i^q]$) and is influenced by all defects present in the system. Based on this principle, we utilize a numerical charge balance solver[Gad13; Bak17; Bow18b] to simulate doping at an elevated temperature followed by a quench to room temperature. After the quench, high temperature defect concentrations are frozen in, but each defect is allowed to change its charge state in order to achieve charge balance. Electron and hole concentrations are calculated using an effective density of states from experiment.

Figure 5.2 is a representative plot of $\log n$ versus $\log[\text{Si}]$, where $[\text{C}] = 3 \times 10^{16} \text{ cm}^{-3}$, $[\text{O}] = 4 \times 10^{17} \text{ cm}^{-3}$, the doping temperature is representative of MOCVD growth (1400 K), and the native chemical potentials are 0.2 eV from the Al-rich limit. Impurity chemical potentials are determined by imposing fixed concentrations on each impurity. Thus μ_{O} and μ_{C} vary with Si concentration in order to maintain constant levels of O and C. Chemical potentials are compared to stability-limiting phases in post-processing. The knee maximum n in this plot is consistent with carrier concentrations common in Si-doped AlN (order of 10^{15} cm^{-3}),

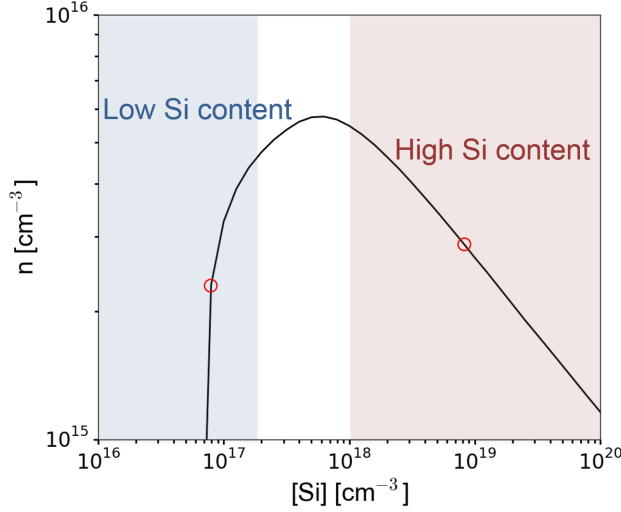


Figure 5.2 Representative room temperature plot of n versus $[\text{Si}]$. The two red circles indicate points at which concentration profiles are reported in Table 5.1.

but the Si concentration where it occurs is predicted to be too low (experimentally, the peak is close to 10^{19} cm^{-3}). [Bry15; Bry18] We therefore examined how the predicted knee responds to changes in processing conditions and background impurities, as well as the effect of defect vibrational energies. In all cases, we obtained a compensation knee from the results of charge balance solutions when vacancy-silicon complexes were included in the defect set.

The shape of the knee and the location of the knee maximum depend on the model parameters. The predicted Si concentration and carrier concentration at the knee maximum both increase as the growth conditions vary from N-rich to Al-rich. Common background impurities (C and O) typically compensate the free carriers. As a result, increasing their concentration reduces the maximum carrier concentration and shifts the knee maximum to higher Si concentrations. Quantitative predictions of the knee are highly sensitive to the Fermi level, so even small contributions to the formation energies, including vibrational energies, may be relevant. Due to the use of hybrid functionals and the large number of defects and configurations, it is a substantial undertaking to compute vibrational contributions. We have explored the sensitivity to vibrational energies in Si-containing defects by assuming a constant vibrational contribution per Si atom in each defect, which alters the relative energies of complexes with different numbers of constituent defects. In this approximation, vibrational energies shift the knee maximum to higher Si concentrations, more consistent

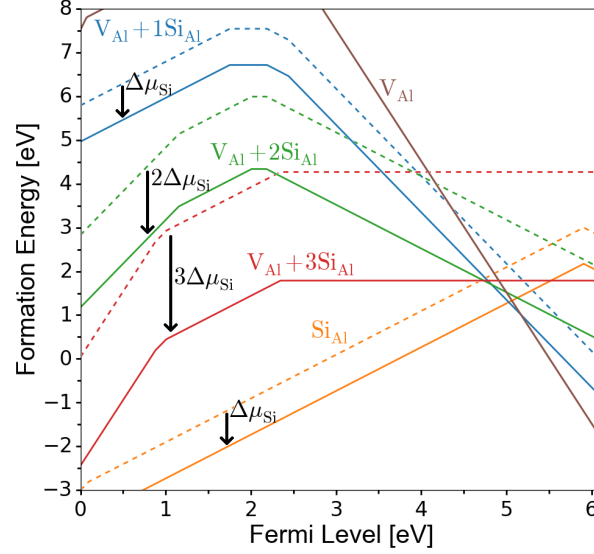


Figure 5.3 Formation energy versus Fermi level for V_{Al} , Si_{Al} , and most favorable configurations of $V_{Al} + nSi_{Al}$ complexes. The dotted lines and solid lines correspond to the low and high [Si] sides of the compensation knee, respectively.

with experiment. This does not contradict the convention that vibrational energies tend to be similar for single-site defects. Rather, it points to the potential importance of including vibrational energies when complexes are considered.

We now turn to understanding the mechanism of compensation in Si-doped AlN. Si is added to the system by increasing its availability in the growth environment, which is equivalent to increasing the Si chemical potential. Figure 5.3 plots the formation energy of the most energetically favorable configuration of each $V_{Al} + nSi_{Al}$ complex for low (dotted) and high (solid) Si concentrations, corresponding to either side of the knee. As can be seen, the change in formation energy is equal to $n\Delta\mu_{Si}$, where n is the number of Si atoms in the complex. That is, higher- n $V_{Al} + nSi_{Al}$ complexes are more strongly affected by changes in Si availability than low- n $V_{Al} + nSi_{Al}$ complexes and Si_{Al} .

Thus, the formation of the knee can be understood in terms of equilibrium concepts. In the low [Si] regime, Si_{Al} and V_{Al} dominate and thus control the equilibrium Fermi level. In this regime, Fermi level increases with Si doping. But in the high [Si] regime, the favorability of higher- n complexes is enhanced, and the Fermi level is controlled by the intersection of $E_{Si_{Al}}^f$ and $E_{(V_{Al}+nSi_{Al})}^f$. Because $E_{(V_{Al}+nSi_{Al})}^f$ shifts down more rapidly than $E_{Si_{Al}}^f$ for $n = 2$ and $n = 3$, the equilibrium Fermi level decreases. That is, the Fermi level (carrier concentration)

decreases with Si doping in the high [Si] regime.

Our predictions point to the following observations. Second nearest neighbor defects in AlN are possible and stable in certain conditions. These defects are central to the formation of the compensation knee and are expected to be in their highest concentrations when Si is most available in the growth environment. This change in compensating defects between the high and low doping regimes motivates exploration of predicted optical signatures to see if these predictions can be further tested by experimental measurements. We focus this analysis on midgap emissions (2.5-4.5 eV) of compensating defects in high concentration.

Two points that have roughly the same carrier concentration on opposite sides of the compensation knee were selected for this and are indicated in Figure 5.2. Table 5.1 summarizes the concentrations of all optically relevant defects above 10^{15} cm^{-3} , as well as their absorption and emission energies, which were calculated using the Franck-Condon approximation.[WN04; Fre14] Optical absorptions and emissions of V_{Al} and $(V_{\text{Al}} + nO_{\text{N}})$ complexes have recently been studied in detail by Yan *et al.*[Yan14] and the energies in Table 5.1 are in line with their results.

At low Si concentration, the dominant defects with emissions in the midgap range are $(V_{\text{Al}} + 3O_{\text{N}})^0$ and C_{N}^{-1} , which are predicted to emit between 3.6 and 3.7 eV. The 3.6 eV emission prediction for C_{N}^{-1} underpredicts the experimental measurement of 3.9 eV as it may emit before it fully relaxes in the excited state.[Col12] There is also a small concentration of vacancy-oxygen complexes which are expected to emit at 3.0 and 3.3 eV in the low Si doping limit.

By contrast, the dominant defects in the high [Si] regime are vacancy-silicon complexes, which emit in the range from 2.9 to 3.4 eV, depending on configuration. Oxygen now forms $(V_{\text{Al}} + 1O_{\text{N}})^{-2}$ and $(V_{\text{Al}} + 2O_{\text{N}})^{-1}$, so oxygen-related emissions shift to lower values around 3.0 and 3.3 eV. Although its concentration is small relative to other defects, V_{Al}^{-3} , with an emission at 2.7 eV, may also contribute to the PL peak at high [Si]. The intensities of the emission peaks due to $(V_{\text{Al}} + n\text{Si}_{\text{Al}})$ in this doping regime are expected to increase relative to the $(V_{\text{Al}} + nO_{\text{N}})$ and C_{N}^{-1} peaks, since [O] and [C] are fixed while [Si] is higher relative to the low doping regime.

Thus in the low [Si] regime we predict an optical emission peak around 3.6 or 3.7 eV due to $(V_{\text{Al}} + 3O_{\text{N}})^0$, perhaps with a shoulder near 3.3 eV due to $(V_{\text{Al}} + 2O_{\text{N}})^{-1}$. C_{N}^{-1} should also contribute with an emission peak at or above 3.9 eV based on experimental assignment. In the high [Si] regime, we predict a peak centered closer to 3.2 eV, with some broadening due

Table 5.1 Calculated optical signatures and concentrations for all optically relevant defects in the low and high [Si] doping regimes (corresponding to the red circles in Figure 5.2). The predicted shift in defect populations corresponds to a shift in predicted emission energies which closely matches experiment.

Defect	Transitions (eV)		Concentration (cm ⁻³)	
	Absorption	Emission	Low [Si]	High [Si]
C_N^{-1}	4.8	3.6	3×10^{16}	1×10^{16}
V_{Al}^{-3}	3.6	2.7	–	8×10^{15}
$(V_{Al} + 1O_N)^{-2}$	4.0-4.1	3.0	1×10^{15}	2×10^{17}
$(V_{Al} + 2O_N)^{-1}$	4.3-4.5	3.3	4×10^{16}	1×10^{17}
$(V_{Al} + 3O_N)^0$	5.0-5.1	3.6-3.7	1×10^{17}	–
$(V_{Al} + 1Si_{Al})^{-2}$	4.0-4.1	2.9-3.0	–	8×10^{17}
$(V_{Al} + 2Si_{Al})^{-1}$	4.1-4.5	3.0-3.4	–	1×10^{18}
$(V_{Al} + 3Si_{Al})^0$	4.5-4.7	3.0-3.4	–	3×10^{17}

to the ensemble of defects emitting at various energies in range of the peak.

To test these predictions, AlN films with low and high Si concentrations (2×10^{18} and 2×10^{19} cm⁻³, respectively) were grown on single crystal AlN substrates using an rf-heated low-pressure MOCVD reactor equipped with an open showerhead.[Ric10] The growth temperature was 1373 K. PL spectra were acquired using a pulsed ArF excimer laser ($\lambda = 193$ nm) together with a Princeton Instruments Acton SP2750 0.75 m high-resolution monochromator and a PIXIS: 2KBUV cooled charge-coupled device camera. Room temperature PL spectra from the low and high Si content samples are shown in Figure 5.4. The sample with low Si content corresponds to a doping level below the onset of the compensation knee, while the sample with high Si content corresponds to a doping level above the compensation knee. A clear shift is observed in the peak PL value from about 3.7 eV in the low [Si] doping regime, to about 3.2 eV in the high [Si] doping regime. In the low [Si] regime, we also observe a shoulder around 3.2 eV. These observations are consistent with the theoretical model proposed above and provide further support for our defect model. In a recent study

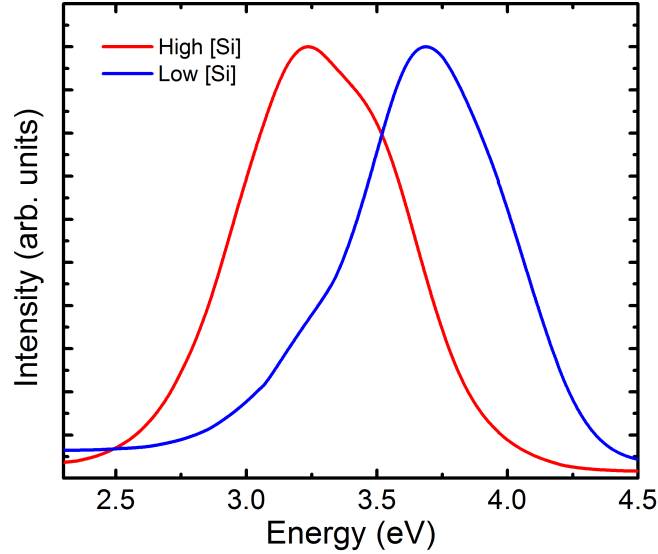


Figure 5.4 Room temperature PL spectra for samples with [Si] at 2×10^{18} and $2 \times 10^{19} \text{ cm}^{-3}$ (below and above the compensation knee, respectively). Normalized by maximum intensity.

of AlGaIn grown on different substrates, a corresponding PL peak transition was observed at high Si doping levels.[Bry18] The peak shift was found to depend only on Si concentration, despite the observation that samples grown on different substrates had different dislocation densities, and hence different strain states. This rules out the possibility that the PL peak shift could be due to differences in strain associated with low and high Si doping conditions. Further experimental details, including deconvolution of the PL, can be found in Bryan *et al.*[Bry15; Bry18]

In conclusion, $V_{\text{Al}} + n\text{Si}_{\text{Al}}$ complexes are crucial to explaining the compensation knee observed in Si doping experiments in AlN. The basic mechanism behind the compensation knee can be explained using simple arguments with a formation energy diagram, together with the fact that the formation energies of $V_{\text{Al}} + n\text{Si}_{\text{Al}}$ vary with Si chemical potential at different rates depending on n . Finally, predicted optical emission peaks for relevant defects on either side of the compensation knee correspond well with experimental PL measurements, suggesting that our defect model appropriately represents the physics of Si doping in AlN.

See Appendix A for supplemental information, including a table of all defects and charge states simulated.

The authors would like to acknowledge partial financial support from NSF (DMR-

1151568, ECCS-1508854, ECCS-1610992, ECCS-1653383), DOE (DE-SC0011883), ARO (W911NF-15-2-0068, W911NF-16-C-0101), and AFOSR (FA9550-14-1-0264, FA9550-17-1-0225). Computer time was provided by NERSC and DoD HPCMP.

CHAPTER

6

FINITE-TEMPERATURE POINT DEFECT PROPERTIES IN AlN FROM FIRST PRINCIPLES

Reproduced from an unpublished manuscript pending submission for publication. Contributing authors: Jonathon N. Baker, Preston C. Bowes, and Douglas L. Irving.

Defect formation energies are routinely computed using ground-state electronic structure methods such as density functional theory. Although these formation energies are calculated at 0 K, they are often used to draw conclusions about finite-temperature systems and processes, such as doping in semiconductors. While prescriptions exist to include finite-temperature contributions in these formation energies, there are few examples in the literature where they are explicitly calculated and included. For that reason, we assess how the inclusion of vibrational and thermal strain contributions influences the temperature dependence of point defects in aluminum nitride. This is done for common extrinsic (Si,

O, and C impurities) as well as intrinsic (Al and N vacancies) point defects. For each of these defects, the temperature dependence of formation energies and transition levels is examined in detail, including the separate influences of vibrational and thermal strain contributions. A number of general trends in finite-temperature properties are identified, which are common to all or many of these defects. The results of simulations at absolute zero are found to be valid for qualitative models that can guide the intuition, and for quantitative predictions of low-temperature measurement data such as photoluminescence. Situations in which finite-temperature effects are found to be significant, depending on the defects and properties of interest, are also discussed.

6.1 Introduction

The electronic and optical properties of a semiconductor are largely determined by native point defects as well as intentional or unintentional impurities introduced into the material during growth. Defect populations are commonly controlled through the growth parameters, which directly tie to the availability of each species and its chemical potential. Precise control, however, requires an intimate understanding of the formation energies of defects, which determine equilibrium defect concentrations, and how the formation energies change with chemical potentials and temperature. For this reason, point defect formation energies obtained by Density Functional Theory (DFT) simulations have provided valuable insight into efforts seeking to controllably dope a wide range of semiconducting materials. And yet, while doping typically occurs at elevated temperatures, the formation energies from DFT studies, which have been valuable qualitative guides, are usually determined at zero Kelvin.

It is, therefore, clearly of interest to assess how defect formation energies and associated properties calculated at 0 K change when finite-temperature effects are included. For this evaluation, we begin with an existing data set of point defect formation energies in aluminum nitride (AlN) which were calculated using the established 0 K prescription.[Col12; Gad13; Gad14; Ald16; Har18; Har19] This data set is then extended to include dominant factors that determine the free energy in semiconductors as the temperature approaches common growth temperatures. These factors include vibration (zero point energy and finite temperature), thermal strain, and movement of the band edges. Contributions of vibration and thermal strain are added separately so that the impact of each can be evaluated.

The two most common avenues to obtaining vibrational contributions from DFT results are density-functional perturbation theory[Bar01] and finite differences[DK03; DK04]. Thermal strain effects are usually incorporated via the quasi-harmonic approach.[Gra07; Gra09; Gra11a; Gle14] Phonon-phonon interactions, which arise from anharmonic contributions to the vibrational free energy, can be included via an explicit anharmonic approach.[Gra09; Gra11a; Gle14] In a recent study, anharmonic contributions were shown to be negligible in AlN for temperatures below about 1500 K.[Shu16] Despite the availability of theoretical methods for computing vibrational and thermal strain contributions to point defect formation energies, the computational cost of such calculations has been prohibitively high. As such, only a handful of DFT studies have explicitly examined the properties of point defects as a function of temperature in metals[Gra09; Gra11b; Gle14; LS09; Zha18] or semiconductors[Wic18; Est09; AMN03]. We employ strained supercell calculations and finite-difference phonon calculations in the harmonic approximation to estimate the effects of temperature on bulk thermodynamic properties, defect formation energies, and transition levels.

6.1.1 Defect Formation Energies

Defect formation energies in semiconductors are calculated within the grand canonical formalism, as detailed in the review papers by Van de Walle and Freysoldt.[WN04; Fre14] In this formalism, the formation energy of a point defect D^q , where q is the charge state, is given by

$$E_{D^q}^f = E_{D^q}^{\text{tot}} - E_{\text{bulk}}^{\text{tot}} - \sum_i n_i \mu_i + q \mu_e + E_{D^q}^{\text{corr}} \quad (6.1)$$

$E_{D^q}^{\text{tot}}$ and $E_{\text{bulk}}^{\text{tot}}$ are the total energies of a supercell containing defect D^q and of the corresponding bulk supercell, respectively. μ_i is the chemical potential of species i in the bulk relative to the relevant chemical reservoir to create the defect, and n_i is the number of atoms of species i exchanged between the bulk and its reservoir. μ_e is the electron chemical potential (i.e. the Fermi level), which is often defined relative to the valence band maximum. $E_{D^q}^{\text{corr}}$ is a *post-hoc* finite-size correction to the energy of a charged defect supercell.

The review article by Freysoldt discusses how to extend Equation 6.1 to finite temperatures and pressures (cf. Equation 23 in that work).[Fre14] In the present work, we will make the following simplifying assumptions: (1) the vibrational and thermal strain contributions are independent (i.e. vibrational free energies are not significantly affected by thermal strain); (2) electronic entropy and the energy associated with the finite-temperature Fermi

distribution of the electrons are not significant; (3) anharmonic effects are not significant up to 1500 K in AlN.

These simplifying assumptions may lead to some degree of error in the results, which we will briefly address here, as well as throughout the paper where possible. Assumption (1) was tested for bulk AlN by computing phonon distributions in supercells with varying lattice parameters; strain was not found to significantly affect the free energy of the bulk phonon distribution, as will be discussed later in the manuscript. Assumption (2) is valid in nondegenerate semiconductors, but becomes less valid as the Fermi level approaches either band edge at high temperatures. To illustrate this, in AlN at 1500 K, even with high carrier concentrations (10^{19} cm^{-3} free electrons), we estimate the electronic entropy to contribute less than 5 meV per 96-atom supercell (less than 0.01 kJ/mol); with 10^{18} cm^{-3} free electrons, the electronic entropy contribution is almost an order of magnitude lower. Assumption (3) has been shown to be valid for bulk AlN at temperatures up to about 1500 K.[Shu16] Indeed, we have demonstrated that the bulk free energy of AlN can be accurately predicted up to 1500 K without anharmonic effects (see Section 6.3.1). On this basis, we anticipate that anharmonic effects are not necessary to compute accurate defect formation energies in the same temperature range. However, without a rigorous accounting of anharmonic effects (which would come at great computational expense), it is unknown whether they are important for computing the formation energy of any particular defect. Vacancy defects, around which atomic displacements are highly asymmetrical, may be particularly susceptible to anharmonic effects, as has been demonstrated in metallic systems at temperatures approaching the melting point.[Gle14]

With these approximations, Equation 6.1 becomes

$$\begin{aligned}
 E_{D^q}^f(T, P) = & E_{D^q}^{\text{tot}}(V(T)) - E_{\text{bulk}}^{\text{tot}}(V(T)) \\
 & + F_{D^q}^{\text{vib}}(T) - F_{\text{bulk}}^{\text{vib}}(T) \\
 & - \sum_i n_i \mu_i(T, P) + q\mu_e + E_{D^q}^{\text{corr}}
 \end{aligned} \tag{6.2}$$

at finite temperatures and pressures, where $E_{D^q}^{\text{tot}}(V(T))$ and $E_{\text{bulk}}^{\text{tot}}(V(T))$ are the total energies of the defect and bulk systems, respectively, in strained supercells with lattice parameters corresponding to thermal expansion at the given temperature; and $F_{D^q}^{\text{vib}}(T)$ and $F_{\text{bulk}}^{\text{vib}}(T)$ are the vibrational free energies of the defect and bulk systems, respectively, in the unstrained (0 K) supercells, per assumption (1) above. The chemical potentials μ_i are determined by

the parameters of a given experiment. However, upper and lower bounds may be placed on μ_i , and the temperature and pressure dependence of these bounds may be approximated from thermochemical tables.[Bak18b] The free energies of most crystalline solids may also be determined from theory if thermochemical tables are unavailable, by computing vibrational and thermal strain contributions (see Section 6.3.1). In general, the electrostatic correction term E_D^{corr} is also dependent on thermal strain, since periodic images of charged defects move farther away from each other as the lattice thermally expands.

In the following subsections, we discuss how the vibrational free energy contribution to the defect formation energy is obtained from calculations of phonons in the harmonic approximation.

6.1.2 Phonons in the Harmonic Approximation

The harmonic approximation comes from writing a Taylor expansion of the energy of a system as a function of the positions of the ions in the system. The Taylor expansion of the energy about the equilibrium ion positions is given by

$$E(\mathbf{x}) = E(\mathbf{x}_0) + \frac{1}{2} \sum_{i,j} \Delta x_i \Delta x_j \frac{\partial^2 E(\mathbf{x}_0)}{\partial x_i \partial x_j} + \mathcal{O}(\Delta x^3) \quad (6.3)$$

where \mathbf{x} is the configuration space of ions in the system, \mathbf{x}_0 is the equilibrium configuration, x_i indicates the i th component of \mathbf{x} , and Δx_i is a small displacement along component i . The first term, $E(\mathbf{x}_0)$, is the ground state energy of the system (as calculated by DFT, for example). The second term, which acts like a harmonic oscillator, represents the vibrational contribution to the total energy. All other terms are of order $\mathcal{O}(\Delta x^3)$ and higher in the small displacements Δx_i .

The basic procedure to compute vibrational properties is to calculate the dynamical matrix D_{ij} , given by

$$D_{ij} = \frac{1}{\sqrt{M_i M_j}} \sum_l \left[\frac{\partial^2 E(\mathbf{x}_0)}{\partial x_i \partial x_j} e^{-i\mathbf{q}\cdot\mathbf{R}_l} \right] \quad (6.4)$$

where M_i is the mass of the ionic nucleus associated with index i ; \mathbf{R}_l is a lattice translation vector indexed by l (covering all linear combinations of lattice basis vectors); and \mathbf{q} is a reciprocal-space vector (phonon wavevector) within the first Brillouin zone. The exponential factor and the summation over l constitute a Fourier transformation of the matrix

of second derivatives. Thus the dynamical matrix is the Fourier transform of a matrix of mass-weighted second derivatives of the system energy with respect to small displacements of the ions. The eigenvectors and eigenvalues of the dynamical matrix, given by

$$D\mathbf{w}_i = \omega_i^2 \mathbf{w}_i \quad (6.5)$$

correspond to displacement vectors \mathbf{w}_i and frequencies ω_i , respectively, where each index i indicates a normal vibrational mode.

The oscillations of the system are quantized by treating each normal vibrational mode as a quantum harmonic oscillator, and the excited states of these quantized oscillators are known as phonons. Thus each phonon mode i is treated as an independent harmonic oscillator, where the positions of the ions oscillate about the equilibrium configuration \mathbf{x}_0 along the vector \mathbf{w}_i , with frequency ω_i . The energy E_i^{ph} of phonon mode i is given by the energy eigenvalues of the quantum harmonic oscillator with frequency ω_i , that is,

$$E_i^{\text{ph}} = \left(\frac{1}{2} + n_i \right) \hbar \omega_i \quad (6.6)$$

where n_i is the number of phonons in mode i . Note that ε_i is finite even when $n_i = 0$; the remaining energy, $\hbar \omega_i / 2$, is known as the zero point energy of phonon mode i .

From Equation 6.4, one observes that the dynamical matrix is a function of the phonon wavevector \mathbf{q} . The phonon dispersion relation can be computed by solving for the eigenvalues of the dynamical matrix as a function of \mathbf{q} . In Section 6.1.3 below, we omit explicit reference to \mathbf{q} for the sake of notational simplicity. In principle, the thermodynamic quantities derived below must be integrated with respect to \mathbf{q} over the first Brillouin zone; however, for large supercells, numerical integration over the first Brillouin zone is well-converged by sampling at the Γ -point ($\mathbf{q} = \mathbf{0}$).

6.1.3 Thermodynamics of Phonons

Inasmuch as they are modeled by an infinite set of quantum harmonic oscillators, phonons in an infinite crystal are bosons, and they follow Bose-Einstein statistics. This section will briefly derive the most relevant results of such a distribution. The partition function Z_i for

a harmonic oscillator with frequency ω_i is given by

$$Z_i = \sum_{n_i=0}^{\infty} e^{-\left(\frac{1}{2} + n_i\right) \frac{\varepsilon_i}{kT}} \quad (6.7)$$

where $\varepsilon_i = \hbar\omega_i$ is the energy associated with adding or removing a single phonon, k is Boltzmann's constant, and T is temperature. This summation is a geometric series in $e^{(-\varepsilon_i/kT)}$, which converges to

$$Z_i = \frac{e^{(-\varepsilon_i/2kT)}}{1 - e^{(-\varepsilon_i/kT)}} \quad (6.8)$$

The partition function for a set of independent (non-interacting) phonons is the product of their individual partition functions:

$$Z = \prod_i Z_i \quad (6.9)$$

With the partition function for a system of phonons, the free energy, internal energy, entropy, and heat capacity associated with them can be derived.

The phonon free energy F_{ph} is obtained from the partition function via

$$\begin{aligned} F_{\text{ph}} &= -kT \ln Z \\ &= \frac{1}{2} \sum_i \varepsilon_i + kT \sum_i \ln(1 - e^{(-\varepsilon_i/kT)}) \end{aligned} \quad (6.10)$$

The chemical potential of phonons is zero (since they are created and destroyed within the system rather than exchanged with an external reservoir), so the free energy given by this expression is equivalent to the grand potential of the phonon distribution. The first, temperature-independent term is the zero-point energy (ZPE) associated with atomic vibrations, which remains even as the temperature approaches absolute zero.

The entropy S_{ph} is obtained by taking the derivative of the free energy with respect to

temperature:

$$\begin{aligned}
S_{\text{ph}} &= -\frac{\partial F_{\text{ph}}}{\partial T} \\
&= -k \sum_i \left[\ln \left(1 - e^{(-\varepsilon_i/kT)} \right) \right. \\
&\quad \left. - \frac{\varepsilon_i}{kT} \frac{1}{e^{(\varepsilon_i/kT)} - 1} \right]
\end{aligned} \tag{6.11}$$

Note that, despite the zero point energy, the entropy approaches zero as T approaches 0 K, as it should by the Third Law of Thermodynamics.

To derive the total internal energy of the phonon distribution, we must first determine an expression for the average number of phonons. The average number of phonons N_i of frequency ω_i is given by

$$N_i = \sum_{n_i=0}^{\infty} n_i P(n_i) \tag{6.12}$$

where $P_i(n_i)$ is the probability that n_i phonons will occupy mode i . In terms of the partition function,

$$\begin{aligned}
N_i &= \frac{1}{Z_i} \sum_{n_i=0}^{\infty} n_i e^{\left(-\frac{(\frac{1}{2}+n_i)\varepsilon_i}{kT} \right)} \\
&= -\frac{1}{Z_i} \sum_{n_i=0}^{\infty} \left(\frac{1}{2} + kT \frac{\partial}{\partial \varepsilon_i} \right) e^{\left(-\frac{(\frac{1}{2}+n_i)\varepsilon_i}{kT} \right)} \\
&= -\frac{1}{Z_i} \left(\frac{1}{2} + kT \frac{\partial}{\partial \varepsilon_i} \right) \sum_{n_i=0}^{\infty} e^{\left(-\frac{(\frac{1}{2}+n_i)\varepsilon_i}{kT} \right)} \\
&= -\frac{1}{Z_i} \left(\frac{1}{2} + kT \frac{\partial}{\partial \varepsilon_i} \right) Z_i \\
&= -\left(\frac{1}{2} + \frac{kT}{Z_i} \frac{\partial}{\partial \varepsilon_i} Z_i \right)
\end{aligned} \tag{6.13}$$

Finally, evaluating the derivative and simplifying the result,

$$N_i = \frac{1}{e^{(\varepsilon_i/kT)} - 1} \tag{6.14}$$

Now we can write the total internal energy U_i of the system of phonons as

$$\begin{aligned} U_{\text{ph}} &= \sum_i \left(\frac{1}{2} + N_i \right) \varepsilon_i \\ &= \frac{1}{2} \sum_i \varepsilon_i + \sum_i \frac{\varepsilon_i}{e^{(\varepsilon_i/kT)} - 1} \end{aligned} \quad (6.15)$$

As a sanity check, note that the free energy, entropy and internal energy are related by

$$F_{\text{ph}} = U_{\text{ph}} - T S_{\text{ph}} \quad (6.16)$$

which is indeed true by substitution.

The heat capacity of the phonons is given by the temperature derivative of the internal energy,

$$\begin{aligned} C_{\text{ph}} &= \frac{\partial}{\partial T} U_{\text{ph}} \\ &= - \sum_i \left(\frac{\varepsilon_i^2}{kT^2} \right) \frac{e^{(\varepsilon_i/kT)}}{\left(e^{(\varepsilon_i/kT)} - 1 \right)^2} \end{aligned} \quad (6.17)$$

Equations 6.11-6.17, if computed for a phonon distribution from a finite supercell, express thermodynamic quantities in units per supercell. For instance, Equation 6.17 gives the heat capacity of the phonon distribution within the supercell, and would need to be divided by the supercell volume in order to be expressed as a volumetric heat capacity.

6.1.4 Connection to Defect Formation Energies

The vibrational free energies $F_{D^q}^{\text{vib}}(T)$ and $F_{\text{bulk}}^{\text{vib}}(T)$ from Equation 6.2 are simply the free energies of the phonon distributions of the defect and bulk supercells, respectively. Section 6.1.3 outlines the procedure for obtaining the vibrational free energy of a supercell, given a minimum-energy configuration of the ions in the supercell. Following that procedure, Equation 6.10 may be used to compute the vibrational contributions to the temperature dependence of the defect formation energy. Note that the ZPE contributes to the total energy of the supercell even at absolute zero. The ZPE contribution (which is usually small) is necessarily neglected if the phonon distribution is not computed.

Keep in mind that the harmonic model does not include the effects of thermal strain. In

principle, one can include thermal strain either by considering anisotropic behavior explicitly (which goes beyond the harmonic approximation)[Gra09; Gra11a], or by applying the harmonic approximation to artificially strained supercells (the so-called quasi-harmonic approximation)[Gra07]. As a third alternative, in this paper we assume that phonon and strain effects add orthogonally, an assumption which we will explore in Section 6.3.1.

6.2 Methodology

6.2.1 Details of DFT Calculations

All DFT calculations were performed using the Vienna *Ab initio* Simulation Package (VASP 5.3).[KF96a; KF96b; KH94; KH93] All defects were modeled using a 96-atom cell with a 2x2x2 k-point mesh. Pseudopotentials were used to represent Al, N, Si, O, and C with 3, 5, 4, 6, and 4 explicitly modeled electrons, respectively.

DFT total energies for defect and bulk cells were computed using the hybrid exchange-correlation functional of Heyd, Scuseria, and Ernzerhof (HSE), which includes a fraction of short-range exact Hartree-Fock exchange set to $\alpha = 0.32$, resulting in a bandgap of about 6.1 eV at absolute zero without phonon contributions, as is conventional for 0 K formation energy calculations.[Hey06; Hey03] HSE functionals have been used in previous studies to predict the defect formation energies of point defects and complexes in InN, GaN, and AlN.[Gor14; Gad14; Gad13; Lyo14; Lyo10; Col12; Sil12; Har18; Har19] For all HSE calculations, normal precision settings were used with a plane-wave energy cutoff of 520 eV. In addition to total energy calculations, all defect relaxations were performed using the HSE functional. To correct for image-charge interactions and electrostatic potential alignment for charged defect cells, we used a custom finite-size correction scheme based on the method of Kumagai and Oba,[KO14] using an experimental relative permittivity of 9.14.[Col67] The Asphalt point defect informatics framework was utilized for analysis and error checking of the data generated for this manuscript.[Bak19]

Phonon calculations were performed using the generalized gradient approximation (GGA) functional of Perdew, Burke, and Ernzerhoff (PBE).[Per96] For these calculations, accurate precision settings were used with a plane-wave energy cutoff of 700 eV. Prior to performing phonon calculations, the lattice parameters were optimized separately for these new settings, and all defects were allowed to relax with the new settings as well. Phonons

were calculated using VASP's built-in finite-difference method with a finite displacement of 0.025 Å.

Only Γ -centered phonons were used to compute thermodynamic quantities associated with the phonon distributions in bulk and defect cells, such as free energy. In principle, thermodynamic quantities should be averaged over all phonon wavevectors in the first Brillouin zone. In practice, such an average is approximated by numerical integration over a finite grid of wavevectors (q-points), and the numerical integral converges with increasing density of q-points. However, for larger supercells, the Brillouin zone is smaller and the numerical integral converges more rapidly with respect to q-point density. For large enough supercells, the numerical integral is sufficiently converged by a single q-point at Γ . In our 96-atom supercells, we tested convergence of thermodynamic properties computed at Γ with respect to a well-converged 5x5x5 q-point grid. At 1500 K, bulk enthalpy and heat capacity at Γ were converged to within about 1 percent, bulk entropy to within 2 percent, and bulk free energy to within 3 percent.

We also tested convergence of the Γ -point phonon free energy contribution to defect formation energies for a subset of defects, and found them to be converged within about 0.1 eV at 1500 K with respect to a 5x5x5 q-point grid (we highlight 1500 K because the convergence is worse at higher temperatures). Wickramaratne *et al.* similarly used Γ -centered phonon distributions to compute vibrational contributions to the free energies of point defects in GaN.[Wic18] In the supplement to their paper, Wickramaratne *et al.* detail very careful convergence tests using PBE functionals, with which they demonstrate that the vibrational contributions to defect formation energies computed from 96-atom cells are converged to within 0.01 eV of values obtained from 216-atom cells at temperatures up to 600 K.

We use HSE simulations to compute defect formation energies at 0 K and in supercells with thermally strained lattice parameters. We use PBE simulations only to compute the *change* in defect formation energies due to vibrational contributions, which is then added to the HSE formation energies. Because the computational expense of an HSE simulation can be more than ten times the cost of a PBE simulation of the same system, it is unfeasible to calculate phonon distributions with the HSE functional for a large number of defects in different charge states. However, convergence testing revealed very little difference in the free energies of bulk phonon distributions computed with PBE versus HSE. Likewise, in the supplement to their paper, Wickramaratne *et al.* found differences only on the order of 0.01

eV at 600 K between PBE and HSE results.[Wic18] For these reasons, we believe the choice of the PBE functional for phonon calculations is justified.

6.2.2 Thermal Strain Approximations

Phonons for the bulk and defect supercells used in this study were only computed with a single set of lattice parameters (corresponding to the lattice parameters at absolute zero with no phonon contributions). Thus any dependence of the phonon distribution on thermal expansion of the lattice is unaccounted for. However, strain-dependent phonon calculations were performed for bulk supercells, and we found only a small change in phonon-dependent properties (such as free energy and band energies) even at high temperatures. Likewise, phonon-dependent bulk properties exhibited little dependence on the choice of functional (PBE versus HSE).

The effects of thermal expansion on defect formation energies have been included in an *ad hoc* manner at 300 K and 1400 K by straining the HSE bulk cells according to experimental thermal expansion data.[Fig09] 1400 K was chosen as it is within the range of typical MOCVD growth temperatures for AlN.[Bry18; Har18] All defects were allowed to relax with the HSE functional in these strained supercells. To include thermal strain effects at 300 K and 1400 K, total energies from the defect and bulk calculations in the corresponding strained supercells are used for $E_{Dq}^{\text{tot}}(V(T))$ and $E_{\text{bulk}}^{\text{tot}}(V(T))$, respectively, in Equation 6.2. We emphasize that this approach is not entirely *ab initio*, since we use experimental thermal expansion data.

6.2.3 Temperature Dependence of Band Edges

To obtain the temperature dependence of the valence band maximum (VBM) and conduction band minimum (CBM) up to 1500 K, we used a combination of experimental and theoretical data. First, we simulated electron-phonon coupling using an adiabatic technique similar to a method employed by Han and Bester.[HB13] When compared to a Bose-Einstein fit from experimental measurements, the bandgap predicted from our electron-phonon coupling simulations was accurate at low temperatures but not at temperatures approaching 1500 K.[Nam04] For this reason, we used the theoretical prediction only to determine the zero-point renormalization (ZPR) of the VBM and CBM due to electron-phonon coupling. Aside from the ZPR, we obtained the temperature dependence of the

VBM and CBM from an empirical model, which we derive below.

The temperature dependence of an experimentally measured bandgap is typically fit to a Bose-Einstein expression of the following form:

$$\begin{aligned} E_g(T) &= \varepsilon_c(T) - \varepsilon_v(T) \\ &= E_g(0) - \frac{2a_B}{e^{(\theta/T)} - 1} \end{aligned} \quad (6.18)$$

where $2a_B$ is an effective electron-phonon interaction constant and $k\theta$ is an effective phonon energy; and ε_v and ε_c are the VBM and CBM, respectively. It will be useful in the following derivation to express the bandgap change $\Delta E_g(T)$ relative to absolute zero,

$$\begin{aligned} \Delta E_g(T) &= E_g(T) - E_g(0) \\ &= \Delta \varepsilon_c(T) - \Delta \varepsilon_v(T) \end{aligned} \quad (6.19)$$

Each band edge (ε_v and ε_c) can be individually modeled by a Bose-Einstein expression as follows.

$$\Delta \varepsilon_v(T) = \frac{a_v}{e^{(\theta/T)} - 1} \quad (6.20)$$

$$\Delta \varepsilon_c(T) = \frac{a_c}{e^{(\theta/T)} - 1} \quad (6.21)$$

where a_v and a_c are unknown effective electron-phonon interaction constants for the VBM and CBM, respectively. The effective phonon energy $k\theta$ is a property of the phonon distribution, and is therefore the same for each band. Comparison with Equations 6.18 and 6.19 reveals the relationship

$$a_c - a_v = -2a_B \quad (6.22)$$

Next, we will derive another expression involving $\Delta \varepsilon_v(T)$ and $\Delta \varepsilon_c(T)$ by a completely different approach. Begin by writing the charge balance expression for an intrinsic semiconductor.

$$n = p \quad (6.23)$$

For a nondegenerate semiconductor, we can substitute

$$N_c \exp\left(\frac{E_i - \varepsilon_c}{kT}\right) = N_v \exp\left(\frac{\varepsilon_v - E_i}{kT}\right) \quad (6.24)$$

where E_i is the intrinsic Fermi level and N_v and N_c are the effective densities of states of

the valence and conduction bands, respectively, given by

$$N_v = 2 \left[\frac{2\pi m_h^* k T}{h^2} \right]^{3/2} \quad (6.25)$$

$$N_c = 2 \left[\frac{2\pi m_e^* k T}{h^2} \right]^{3/2} \quad (6.26)$$

where m_e^* , m_h^* are the electron and hole density of states effective masses, respectively; and h is Planck's constant.

In the typical approach, one solves for the Fermi level relative to one of the band edges as a function of temperature, since only the relative position of the Fermi level is relevant for computing carrier concentrations. However, we instead solve for the sum of the band edges. Taking the logarithm of both sides and rearranging terms,

$$\varepsilon_c(T) + \varepsilon_v(T) = 2E_i(T) + kT \ln \left(\frac{N_c}{N_v} \right) \quad (6.27)$$

Expressing this as a change relative to absolute zero,

$$\Delta\varepsilon_c(T) + \Delta\varepsilon_v(T) = 2\Delta E_i(T) + kT \ln \left(\frac{N_c}{N_v} \right) \quad (6.28)$$

Substituting Equations 6.20 and 6.21 into Equation 6.28,

$$\frac{a_c + a_v}{e^{(\theta/T)} - 1} = 2\Delta E_i(T) + kT \ln \left(\frac{N_c}{N_v} \right) \quad (6.29)$$

In the limit of high temperatures ($T \rightarrow \infty$), the left-hand side of Equation 6.29 approaches a straight line with slope $(a_c + a_v)/\theta$. Since the Fermi distribution approaches a constant in the limit of high temperatures, we posit that the intrinsic Fermi level approaches a constant in this limit as well. Thus in the limit of high temperatures, the slope of the left-hand side must match the slope of the (linear) second term on the right-hand side:

$$\frac{a_c + a_v}{\theta} = k \ln \left(\frac{N_c}{N_v} \right) \quad (6.30)$$

Multiplying both sides by θ ,

$$a_c + a_v = k\theta \ln \left(\frac{N_c}{N_v} \right) \quad (6.31)$$

From Equations 6.22 and 6.31, we can solve for the effective electron-phonon interaction constants for each band:

$$a_v = \frac{1}{2}k\theta \ln\left(\frac{N_c}{N_v}\right) + a_B \quad (6.32)$$

$$a_c = \frac{1}{2}k\theta \ln\left(\frac{N_c}{N_v}\right) - a_B \quad (6.33)$$

Substituting these interaction constants into Equations 6.20 and 6.21, we obtain empirical expressions for the temperature dependence of the band edges from experimental parameters.

$$\Delta\epsilon_v(T) = \frac{\frac{1}{2}k\theta \ln(N_c/N_v) + a_B}{e^{(\theta/T)} - 1} \quad (6.34)$$

$$\Delta\epsilon_c(T) = \frac{\frac{1}{2}k\theta \ln(N_c/N_v) - a_B}{e^{(\theta/T)} - 1} \quad (6.35)$$

Using Equations 6.25 and 6.26, we can alternatively write these expressions in terms of density of states effective masses:

$$\Delta\epsilon_v(T) = \frac{\frac{3}{4}k\theta \ln(m_e^*/m_h^*) + a_B}{e^{(\theta/T)} - 1} \quad (6.36)$$

$$\Delta\epsilon_c(T) = \frac{\frac{3}{4}k\theta \ln(m_e^*/m_h^*) - a_B}{e^{(\theta/T)} - 1} \quad (6.37)$$

For the temperature dependence of the VBM and CBM, we used Equations 6.36 and 6.37 with experimental Bose-Einstein fitting parameters ($\theta = 1000$ K and $a_B = 670$ meV) from Nam *et al.*[Nam04] We computed density of states effective masses ($m_h^* = 1.86m_0$ and $m_e^* = 0.42m_0$) from HSE electronic structure calculations. With these parameters and this empirical model, we found that about 42.8 percent of the reduction in bandgap with increasing temperatures is due to a temperature-dependent increase in the VBM, while the remaining 57.2 percent is due to a temperature-dependent decrease in the CBM.

These temperature dependencies were used only for the change in the band edges as a function of temperature. The value of each band edge at absolute zero was aligned to our theoretical calculations. All energy scales in this paper are defined such that the VBM is 0 eV at absolute zero without ZPR from electron-phonon coupling, as ZPR is not typically assessed in 0 K formation energy prescriptions. The CBM at absolute zero without ZPR is then the same as the calculated bandgap, 6.1 eV (recall that the bandgap is essentially set by the amount of exact exchange). Our electron-phonon coupling calculations predicted a

ZPR of 83 meV for the VBM, and -103 meV for the CBM. Thus we aligned our temperature-dependent VBM and CBM accordingly at absolute zero.

Because we solved for the temperature dependence of each band edge using the temperature dependence of the bandgap from experimental data, the band edges defined in this manner implicitly contain both phonon and thermal strain contributions. To tease out the phonon contributions by themselves, it was necessary to estimate thermal strain contributions from theoretical calculations. Using experimental thermal expansion data, we computed the VBM and CBM in bulk supercells with lattice parameters corresponding to thermal strains from absolute zero to 1500 K in 100 K increments.[Fig09] Using the results, we established an approximate linear relationship between each band edge and each lattice parameter. We exploited this approximate linear relationship to obtain a smooth interpolation of the VBM and CBM as a function of thermal strain at arbitrary temperatures from absolute zero to 1500 K. Finally, we estimated the phonon contributions to the temperature dependence of the VBM and CBM by subtracting these thermal strain contributions from the overall temperature dependencies obtained in the manner described above.

In Section 6.3, we use the phonon contributions to the band edges when discussing formation energies and transition levels computed from phonon contributions alone; and we use the full temperature dependence of the band edges when discussing formation energies and transition levels computed from both phonon and thermal strain contributions. We emphasize again that our approach to the band edge temperature dependencies is not fully *ab initio*; a combination of theoretical and experimental data is used for both the vibrational and thermal strain contributions to the band edges at finite temperatures.

6.3 Results and Discussion

6.3.1 Phonons and Thermodynamic Properties of Bulk AlN

To validate our phonon calculations, we computed phonon frequencies at the Γ point as well as the phonon density of states for bulk AlN. In Table 6.1, we compare our computed phonon frequencies with recent theoretical predictions[Fu15] and experimental measurements[Bic05] from the literature. Our predictions are in good agreement with the values from the literature, especially the theoretical predictions using a GGA functional, which is expected since we are also using a GGA functional. Figure 6.1 is a plot of the phonon density

Table 6.1 Phonon frequencies in cm^{-1} at $\mathbf{q} = \Gamma$ in bulk AlN, compared with recent theoretical predictions[Fu15] and experimental measurements[Bic05] from the literature.

	This Work	Theory (GGA) [Fu15]	Theory (LDA) [Fu15]	Experiment [Bic05]
E_2^l	228	238	241	248
B_1^l	537	538	560	–
$A_1(\text{TO})$	597	599	643	610
E_2^h	639	645	675	657
$E_1(\text{TO})$	651	655	681	670
B_1^h	708	711	749	–

of states as a function of phonon frequency. Our density of states is also in good agreement with other theoretical calculations[Fu15; Sie06] and experimental measurements[Loo95; Per93]. These findings validate our calculated phonon distribution for bulk AlN, which justifies our use of the calculated phonon distribution to compute thermodynamic quantities.

At finite temperatures, phonons provide the most significant contribution to the enthalpy, entropy, and free energy of a material relative to an absolute zero reference. Therefore, assuming the thermal volume change is small (as it usually is for condensed phases), one may estimate the enthalpy of the material relative to 0 K as the internal energy of the phonon distribution (Equation 6.15); the entropy as the entropy of the phonon distribution (Equation 6.11); and the Gibbs free energy relative to 0 K as the Hemholtz free energy of the phonon distribution (Equation 6.10).

We computed these properties for AlN from the Γ -centered phonon distribution in our 96-atom supercells. Figure 6.2 shows the Gibbs free energy, along with the enthalpic and entropic contributions, from the DFT calculations (solid curves) and from experimental data found in JANAF tables (points).[CJ86] The reference enthalpy has been defined such that the enthalpy is zero at absolute zero temperature. Clearly, our prediction provides a good estimate of the experimental measurements. The predicted value is within 0.5% of the experimental value at 1000 K, and within 1.5% at 1500 K. These results indicate that the Γ -centered phonon distribution from the 96-atom bulk supercells captures many phenomenological thermodynamic quantities with sufficient accuracy.

Figure 6.3 shows the molar heat capacity of AlN from our predictions using Equation

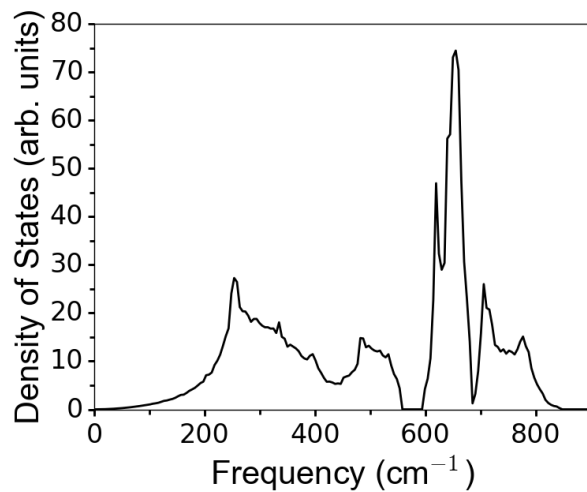


Figure 6.1 Calculated phonon density of states for AlN.

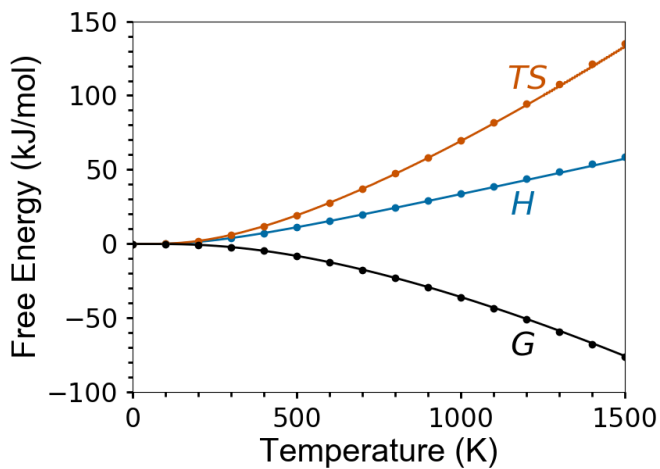


Figure 6.2 Enthalpy, entropy and Gibbs free energy of AlN as predicted from phonon calculations (solid curves), with experimental data from JANAF tables[CJ86] superimposed (points). The enthalpy has been set to zero at absolute zero.

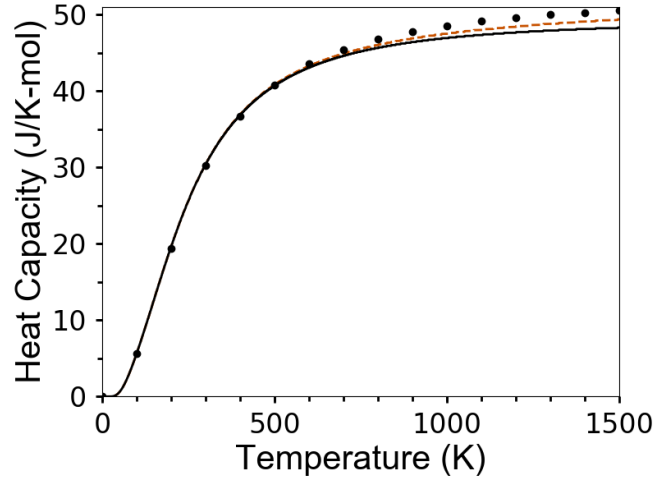


Figure 6.3 Molar heat capacity of AlN at constant volume (C_v) as predicted from phonon calculations (solid curve), with experimental data at constant pressure (C_p) taken from JANAF tables[CJ86] superimposed (points). The dashed curve represents the phonon heat capacity plus the approximate heat capacity due to thermal strain.

6.17 (solid curve) and from experimental data found in JANAF tables (points).[CJ86] Note that Equation 6.17 is a derivative taken at constant volume, so strictly speaking it is related to C_v , the heat capacity at constant volume. The experimental measurements tabulated by JANAF are taken at constant pressure (C_p , the heat capacity at constant pressure). At low temperatures for condensed phases, thermal expansion is negligible, so C_v and C_p should be approximately equivalent. Indeed in Figure 6.3 one observes that the predicted and tabulated heat capacities agree almost perfectly at temperatures up to about 500 K. Even at high temperatures, the discrepancy is small enough that it is impossible for the naked eye to discern the difference in slope in Figure 6.2 between predicted and tabulated values of H .

Thermal strain is one of the primary discrepancies between C_v and C_p at elevated temperatures. If our assumption that phonon and strain effects add orthogonally is valid, we should be able to approximate C_p by adding the heat capacity due to thermal strain to the predicted C_v curve. To determine the heat capacity due to thermal strain, we used experimental thermal expansion data to compute the total energies of bulk supercells with lattice parameters corresponding to thermal strains from absolute zero to 1500 K in 100 K increments.[Fig09] It was observed that the total energy varies quadratically with each lattice parameter, which allowed for the smooth interpolation of the total energy as

a function of thermal strain at arbitrary temperatures. In turn, the derivative of this total energy curve gives the heat capacity due to thermal strain (sans any effect of the thermal strain on the energy of the phonon distribution). While the additional energy due to thermal strain was not enough to noticeably alter the H curve in Figure 6.2, the additional heat capacity due to thermal strain is more significant at higher temperatures. The dashed curve in Figure 6.3 represents the heat capacity of the phonon distribution plus the thermal strain contribution. Thus the dashed curve provides an estimate of C_p under the assumption that phonon and thermal strain contributions add orthogonally.

From this analysis, it is found that the thermal strain contribution accounts for approximately half of the discrepancy between the predicted C_v and the measured C_p . At 1500 K, the measured C_p is 50.5 J/K-mol, whereas the calculated C_p is 49.4 J/K-mol (the thermal strain contribution at this temperature is about 1.1 J/K-mol). To account for the remaining 1.1 J/K-mol, we investigated the effect of thermal strain on the phonon distribution, the $P\Delta V$ contribution to the enthalpy, point defect contributions to the enthalpy, convergence with respect to cell size and number of q-points, and the internal energy of the electronic distribution. In short, it was found that the magnitude of each of these possible contributing effects was too small to fully account for the 1.1 J/K-mol discrepancy. Below, the assessment of these contributing factors as well as others which we were unable to investigate are discussed.

To determine the effect of thermal strain on the heat capacity of the phonon distribution, the phonon distribution for the thermally strained supercell corresponding to 1500 K was calculated. The heat capacity of phonons in the thermally strained supercell was found to be less than 0.1 J/K-mol higher than the heat capacity of phonons in the unstrained (absolute zero) supercell, indicating that the effect of thermal strain on the phonon heat capacity does not account for the 1.1 J/K-mol discrepancy between the predicted and tabulated C_p (at least not within the quasi-harmonic approximation). Incidentally, this result lends support to the approximation that the phonon and thermal strain contributions to thermodynamic quantities are independent of one another.

The $P\Delta V$ term in the bulk enthalpy was also originally neglected in the above results as a function of temperature. However, calculations reveal that the $P\Delta V$ term only contributes about 2.4×10^{-5} J/K-mol to the heat capacity at atmospheric pressure (the pressure at which the JANAF measurements were performed), significantly smaller than the 1.1 J/K-mol discrepancy. The contribution of the $P\Delta V$ term to the total enthalpy is likewise negligible.

Although the data in the JANAF tables has been measured in bulk (undoped) AlN, there is always the possibility of intrinsic defects and unintentional dopants in any given sample. The contribution of isolated point defects to the heat capacity of the system (for a given population of point defects) can be determined from DFT simulations. This falls into two categories. First is the heat capacity associated with the vibrational modes of each defect. Even for high concentrations of point defects (10^{19} cm^{-3} vacancies), this contribution modifies the overall heat capacity on the order of $1 \times 10^{-3} \text{ J/K-mol}$ at 1500 K, which is too small to account for the 1.1 J/K-mol discrepancy. Second is the heat capacity associated with the formation of defects itself (that is, the changing number of defects as a function of temperature effectively stores or releases energy). This effect was approximated by considering a system with intrinsic vacancy defects only. Even for a system with 10^{19} cm^{-3} vacancies at 1500 K, this effect modifies the heat capacity by only 0.04 J/K-mol at 1500 K, and is again too small to account for the 1.1 J/K-mol discrepancy. Moreover, this effect would only contribute to heat capacity measurements if the defect populations have sufficient time to come to equilibrium as the temperature is varied.

The heat capacity of the phonon distribution integrated over a dense grid of q-points is about 0.5 J/K-mol higher at 1500 K than the heat capacity computed from the Γ -point alone. This accounts for some, but not all, of the 1.1 J/K-mol discrepancy. The internal energy of the electronic (Fermi) distribution does not contribute significantly to the heat capacity in such a wide bandgap semiconductor.

There are some possible sources for the 1.1 J/K-mol discrepancy which we were unable to investigate. For instance, extended defects such as dislocations and grain boundaries may have an effect. Phonon-phonon interactions and other anharmonic vibrational effects may contribute to the heat capacity as well, although anharmonic effects are not expected to be significant below 1500 K.[Shu16] The fact that we used experimental data rather than first principles predictions for the thermal strain likely influences our prediction for the thermal strain contribution. Finally, the level of theory (DFT with PBE functionals for phonon effects and HSE functionals for thermal strain effects) may not capture the internal energies with sufficient precision for an accurate prediction of the heat capacity at high temperatures (although we found the heat capacity of the 0 K phonon distribution to differ by only about 0.1 eV at 1500 K when computed with HSE functionals versus PBE).

Of course it is also possible that the 1.1 J/K-mol discrepancy is due to some combination of the possibilities mentioned above. Despite all of this, the approximation of C_p computed

here comes very close to experimental data even at high temperatures, especially for the purpose of extending the computation of defect-related properties to finite temperatures. Moreover, the prediction of the bulk free energy is found to be accurate, which is important because free energy change is the key quantity for predicting the temperature dependence of defect formation energies.

6.3.2 Defect Formation Energies: Impurities

Sections 6.3.2.1-6.3.2.3 will evaluate in detail the temperature dependence of the formation energies of Si, O, and C impurity point defects in AlN. The formation energy diagrams presented in each subsection (Figures 6.5-6.7) represent formation energies with a fixed set of native and impurity chemical potentials at all temperatures (a given set of chemical potentials abstractly represents a specific set of environmental conditions during doping). The chemical potentials have been selected to represent a realistic doping scenario based on the output of a charge-balance solver involving these and other defects in AlN at 1400 K.[Har18] In order to isolate vibrational and thermal strain effects, we do not vary any of the chemical potentials as a function of temperature. Regardless, thermodynamic transition levels (TTLs) and DX transition levels are not affected by changes in chemical potentials. TTLs, which are tied to defect ionization levels, are the Fermi levels at which two charge states of a given defect have equal formation energies; DX transition levels the Fermi levels at which two distinct configurations of the same defect in different charge states have equal formation energies.

Figure 6.4 is a summary plot of the band edges, TTLs, and DX transition levels as a function of temperature for the impurities studied here. The dashed black lines correspond to the VBM and CBM as a function of temperature. The lower and upper boundaries of the plot (at 0 eV and 6.1 eV, respectively) correspond to the VBM and CBM at 0 K without ZPR. Thus the ZPR of the VBM and CBM can be read from the plot by comparing the intercepts of the black dashed lines at 0 K with the plot boundaries. The solid lines of different colors represent various transition levels, including $\text{Si}_{\text{Al}}(+|-)$ on-site to DX transition levels for two distinct DX configurations; the $\text{O}_{\text{N}}(+|-)$ on-site to DX transition level; and the $\text{C}_{\text{N}}(0|-)$, $\text{C}_{\text{N}}(+|0)$, and $\text{C}_{\text{N}}(+2|+)$ TTLs. As discussed previously, all transition levels represented on the plot are independent of chemical potentials. For both band edges and transition levels, the smooth curves represent phonon contributions only, while the discrete states (horizontal lines) at 300 K and 1400 K include phonon and thermal strain contributions. The colored

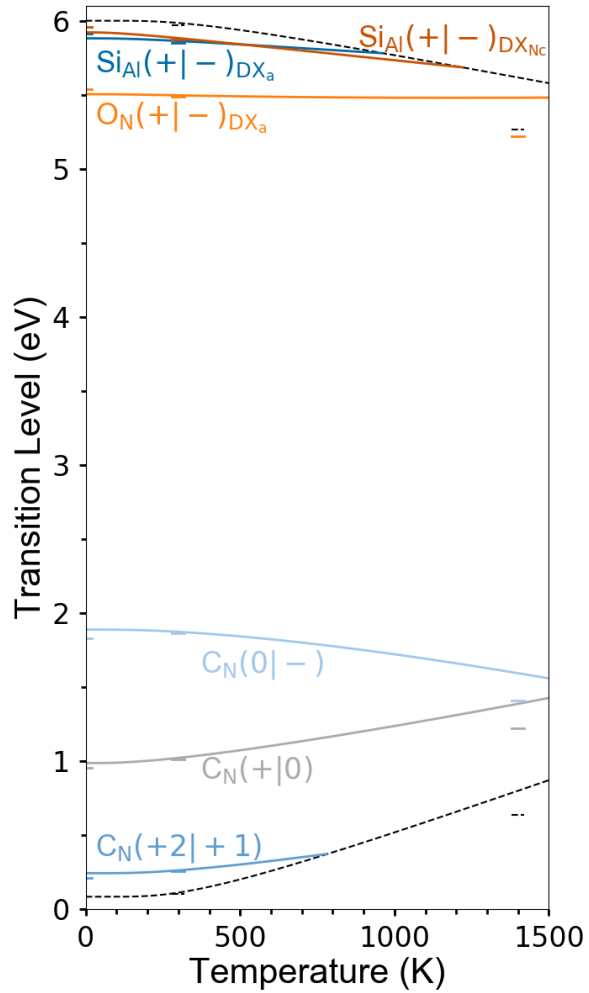


Figure 6.4 Fermi levels corresponding to DX transitions for Si_{Al} and O_{N} , and TTLs for C_{N} , in AlN. Band edges are plotted as dotted lines. The smooth curves represent phonon contributions only, while the discrete states at 300 K and 1400 K include phonon and thermal strain contributions. The notches at 0 K represent the transition levels without ZPR. All energies are defined relative to the calculated VBM without ZPR, which we have set to 0 eV.

notches at 0 K indicate the transition levels without ZPR, so the ZPR for each transition level can be read off of the plot by comparing the intercept of the curve at 0 K with the value of the notch with the same color. From these notches and offsets of the band edges, it can be seen that ZPR may be an important parameter to consider when selecting the amount of exact change to determine the bandgap and to determine the defect transition levels at 0 K.

In Figure 6.4, we have highlighted only a handful of relevant transition levels for point defects in AlN. Our selection is intended to be instructive, not comprehensive. For the sake of simplicity, we focus on common impurity point defects substituting on their predominant lattice sites, and we do not discuss defect complexes. In each of the following subsections, we will focus on a particular defect species, continually referring back to Figure 6.4.

6.3.2.1 Silicon

Silicon is one of the more shallow donors in AlN, often used as an intentional n-type dopant. In the donor state $\text{Si}_{\text{Al}}^{+1}$, the Si atom sits substitutionally on an Al site, and this charge state is the predominant defect for most available Fermi levels. However, the Si defect becomes an acceptor when the Fermi level is near the CBM, in one of two favorable DX configurations (a DX configuration is a distortion of the impurity or a nearby host atom away from the ideal lattice site).[Sil11] In the $\text{Si}_{\text{Al-DX}_a}^{-1}$ state, the Si atom is displaced away from the Al site in a direction roughly perpendicular to the c-axis. In the $\text{Si}_{\text{Al-DX}_{\text{Nc}}}^{-1}$ state, the Si atom sits substitutionally on the Al site, and a nearest-neighbor N atom is displaced away from the defect along the c-axis. We also simulated a third configuration, $\text{Si}_{\text{Al-DX}_c}^{-1}$, in which the Si atom is displaced away from the Al site in a direction parallel to the c-axis, but found it to be unfavorable relative to $\text{Si}_{\text{Al}}^{+1}$ for all Fermi levels within the bandgap (at any temperature), in agreement with previous studies using HSE functionals.[Sil11; Gor14; Har19]

Figure 6.5 shows the formation energies of silicon point defects at absolute zero, at absolute zero with a vibrational ZPE correction, at 300 K and 1400 K, each indicated by a unique color. The vertical dashed lines with corresponding colors represent the CBM at the corresponding temperatures. In 6.5(a), only phonon contributions are considered, while in 6.5(b), phonon and thermal strain contributions are considered at finite temperatures. The defects represented include $\text{Si}_{\text{Al}}^{+1}$ (solid lines), $\text{Si}_{\text{Al-DX}_a}^{-1}$ (dash-dotted lines), and $\text{Si}_{\text{Al-DX}_{\text{Nc}}}^{-1}$ (dotted lines).

At low temperatures, $\text{Si}_{\text{Al-DX}_a}^{-1}$ is found to be more favorable than $\text{Si}_{\text{Al-DX}_{\text{Nc}}}^{-1}$, whereas two previous studies using HSE functionals and 0 K energy surfaces have concluded that $\text{Si}_{\text{Al-DX}_{\text{Nc}}}^{-1}$

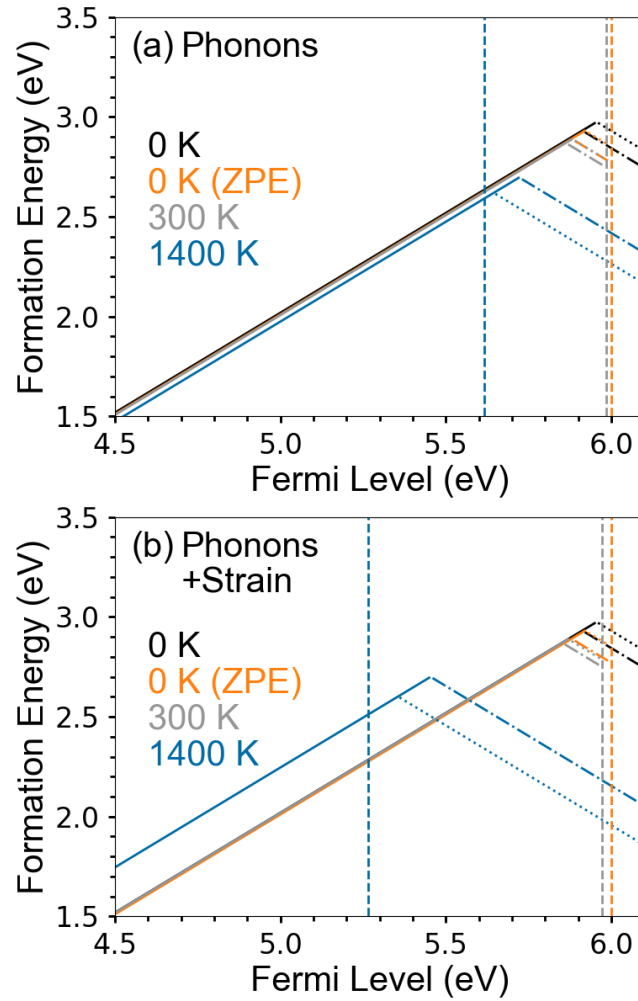


Figure 6.5 Formation energy diagrams for Si_{Al} in the vicinity of the CBM at different temperatures with (a) phonon contributions only and (b) phonon and thermal strain contributions. Vertical dashed lines correspond to the CBM at finite temperatures. Dash-dotted and dotted lines correspond to the DX-a and DX-Nc acceptor states, respectively.

is the more favorable defect configuration.[Sil11; Gor14] However, both of the previous studies use a lower plane-wave energy cutoff, a different amount of exact exchange, and different finite-size corrections, which could easily account for the discrepancy, especially since the formation energies of the two configurations are very close. Because the previous studies did not include finite-temperature effects, their formation energies are most closely comparable to our formation energies at 0 K without ZPE (black lines in Figure 6.5). In our calculations at 0 K without ZPE, the formation energies of the two DX configurations differ by about 0.04 eV. Silvestri *et al.* found the formation energies of the two DX configurations to differ by only 0.11 eV (albeit in the opposite direction).[Sil11] Gordon *et al.* did not directly report information about the $\text{Si}_{\text{Al-DX}_a}^{-1}$ configuration, but did say that their DX transition states differed from those of Silvestri *et al.* by about 0.1-0.2 eV.[Gor14]

Son *et al.* used electron paramagnetic resonance (EPR) to identify a DX transition state about 0.14 eV below the CBM at low temperatures.[Son11] Gordon *et al.* predicts the $\text{Si}_{\text{Al}}(+|-)$ DX_{Nc} transition to be about 0.15 eV below the CBM, identifying it with the state observed by Son *et al.*[Gor14] In fact, we also predict the $\text{Si}_{\text{Al}}(+|-)$ DX_{Nc} transition to be about 0.15 eV below the CBM at 0 K without ZPE. However, even at low temperatures, the energies of the DX transitions and the CBM are influenced by phonon effects. When phonon effects are accounted for, we predict the $\text{Si}_{\text{Al}}(+|-)$ DX_{Nc} transition to be about 0.08-0.10 eV below the CBM in the range from 0-300 K. In the same temperature range, we predict that the $\text{Si}_{\text{Al}}(+|-)$ DX_a transition is about 0.12 eV below the CBM, making it a slightly better candidate for the state observed by Son *et al.*, especially since $\text{Si}_{\text{Al-DX}_a}^{-1}$ is the most favorable DX configuration in our calculations. Thermal strain in this temperature range has a very small effect (on the order of 1 meV), and does not alter this conclusion. Either way, the energies of the two DX transition levels are so close that they may be difficult to distinguish experimentally.

Interesting behavior at finite temperatures is also observed, which could not have been predicted with simulations at absolute zero. In Figure 6.4, it can be seen that the DX-Nc and DX-a transition levels cross each other just above 510 K. At temperatures below this crossing, $\text{Si}_{\text{Al-DX}_a}^{-1}$ is the most favorable configuration; but above it, $\text{Si}_{\text{Al-DX}_{\text{Nc}}}^{-1}$ is the most favorable configuration. We have also highlighted this in Figure 6.3.2.1 by extending the formation energies at 1400 K (blue lines) above the bandgap; at 1400 K, the DX-Nc configuration (dotted line) is clearly lower in formation energy than the DX-a configuration (dash-dotted line). However, at temperatures above about 1220 K, both DX transition levels are above the CBM; that is, both DX configurations are unfavorable at high temperatures within an accessible

range of Fermi levels. In n-type doped AlN, any compensation at such high temperatures must come from other acceptor defects, such as cation vacancy-silicon complexes.[Har18] However, $\text{Si}_{\text{Al-DX}}^{-1}$ defects can still form during re-equilibration at low temperatures; Son *et al.* argue that the energy barrier for an on-site to DX transition is small enough for the transition to occur above about 60 K.[Son11]

There are also some trends in the finite-temperature behavior of these silicon point defects which seem to be generally applicable to all of the defects studied in this paper. The discussion of these more general trends to will be reserved until Section 6.3.4.

6.3.2.2 Oxygen

Oxygen is a common unintentional impurity in AlN. Oxygen and silicon point defects are comparable in many ways; although they prefer to sit on opposite sites, both impurities are donors which can also form compensating DX states when the Fermi level is in the vicinity of the CBM. However, the DX transition is deeper in the bandgap for O than for Si.[Har19; Gor14; McC99] In the donor state O_{N}^{+1} , the oxygen atom sits substitutionally on a N site. In the most favorable DX state $\text{O}_{\text{N-DX}_a}^{-1}$, the O atom is displaced away from the N site in a direction roughly perpendicular to the c-axis. We also simulated the $\text{O}_{\text{N-DX}_c}^{-1}$ configuration, in which the O atom is displaced along the c-axis. At 0 K, we found that the formation energy of $\text{O}_{\text{N-DX}_a}^{-1}$ is about 0.21 eV lower than that of $\text{O}_{\text{N-DX}_c}^{-1}$, in agreement with Gordon *et al.*[Gor14] With increasing temperatures, the difference in formation energies only becomes greater, so that the $\text{O}_{\text{N-DX}_a}^{-1}$ configuration is significantly more favorable than $\text{O}_{\text{N-DX}_c}^{-1}$ at all temperatures; as such, information related to $\text{O}_{\text{N-DX}_c}^{-1}$ is not included on any of the plots.

Figure 6.6 shows the formation energies of oxygen point defects at absolute zero, at 0 K with a ZPE correction, at 300 K and 1400 K, with the same color conventions as in Figure 6.5. Vertical dashed lines represent the CBM at different temperatures, as indicated by the line color. In 6.6(a), only phonon contributions are considered, while in 6.6(b), phonon and thermal strain contributions are both included at finite temperatures. The defects represented include O_{N}^{+1} (solid lines) and $\text{O}_{\text{N-DX}_a}^{-1}$ (dash-dotted lines).

At 0 K without ZPE, we predict the $\text{O}_{\text{N}}(+|-)$ DX_a transition level to be about 0.57 eV below the CBM. Gordon *et al.* predicted the same transition to be 0.64 eV below the CBM, which is quite close to our prediction.[Gor14] As with the $\text{Si}_{\text{Al}}(+|-)$ DX transitions, the slight discrepancy is attributable to different computational settings and a different finite-size correction scheme. When finite-temperature effects are included, the $\text{O}_{\text{N}}(+|-)$ DX_a

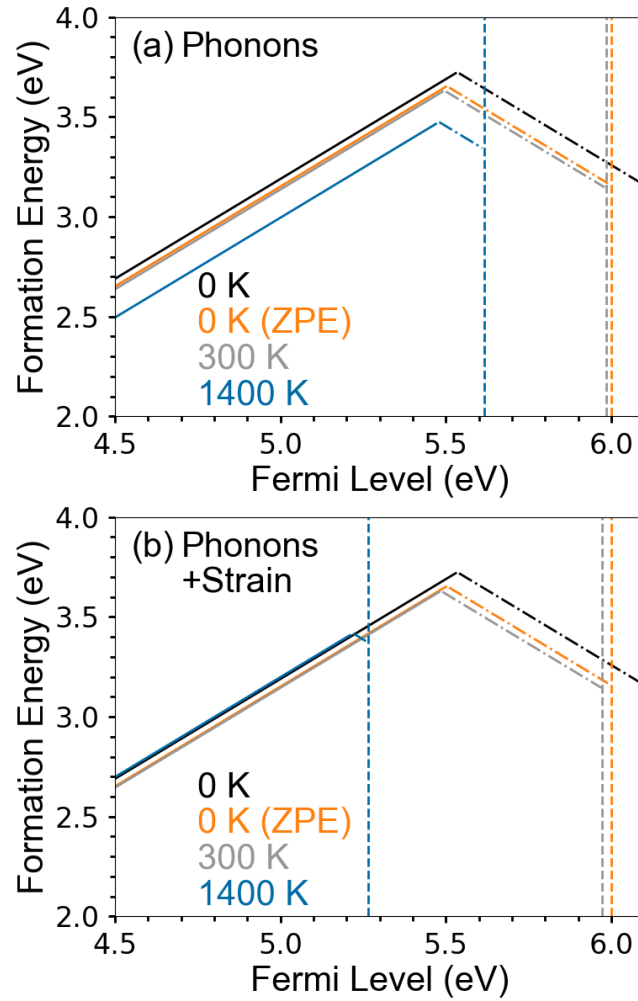


Figure 6.6 Formation energy diagrams for O_N in the vicinity of the CBM at different temperatures with (a) phonon contributions only and (b) phonon and thermal strain contributions. Vertical dashed lines correspond to the CBM at finite temperatures. Dash-dotted lines correspond to the DX-a acceptor state.

transition level shifts to about 0.50-0.49 eV from the CBM in the range from 0-300 K.

Experimental information about the O_{N-DX}^{-1} configurations is limited. Lamprecht *et al.* identify photoluminescence (PL) peaks centered around 2.05 eV and 2.4 eV with transitions from oxygen- and silicon-related DX states, respectively, to the same unknown deep acceptor state.[Lam16; Lam17] They conclude that there must be an $O_N(+|-)$ DX state about 0.35 eV below the $Si_{Al}(+|-)$ DX state. Mason *et al.* used PL in conjunction with optical detection of electron paramagnetic resonance to determine that a PL signature similar to Lamprecht's 2.05 eV peak must be due to a defect with C_{1h} symmetry.[Mas99] As Lamprecht points out, C_{1h} symmetry is compatible with the $O_{N-DX_a}^{-1}$ defect configuration (though not with the $O_{N-DX_c}^{-1}$ configuration). In close agreement with Lamprecht's conclusions, the calculated $O_N(+|-)$ DX_a transition level is found to be about 0.38-0.37 eV below the $Si_{Al}(+|-)$ DX_a transition level in the temperature range from 0-300 K. The calculated $O_N(+|-)$ DX_a level is found to be to be about 0.42-0.39 eV below $Si_{Al}(+|-)$ DX_{Nc} in the same temperature range.

The predicted finite-temperature behavior of O_N differs from the behavior of its cation-site analogue Si_{Al} in a few interesting ways. In Figure 6.4, it can be seen that both $Si_{Al}(+|-)$ DX transitions trend downwards with increasing temperature from phonon effects, whereas the $O_N(+|-)$ DX_a stays almost flat (in fact it decreases by about 0.02 eV from 0-1400 K, but this is indistinguishable in Figure 6.4). This is in part because of the different vibrational characteristics of the Si_{Al}^{+1} and O_N^{+1} donor states, each of which represents the formal charge state of the respective defect. In Figure 6.5(a), it can be seen that the formation energy of Si_{Al}^{+1} hardly changes with temperature from phonon effects alone. By contrast, in Figure 6.6(a) it is found that the formation energy of O_N^{+1} decreases by almost 0.2 eV. Such behavior might be expected if it is assumed that the vibrational properties of these defects in their formal charge states is primarily driven by their atomic mass relative to the bulk atom of the host site. The atomic mass of Si is only 4 percent larger than that of Al, so the vibrational free energy of an on-site defect cell should only be slightly larger than that of the corresponding bulk cell (and therefore the free energy of formation should have a small variation with temperature). However, the atomic mass of O is about 14 percent larger than that of N, so we might expect a much larger vibrational free energy of an on-site defect relative to the bulk (and therefore a larger variation of the formation energy with temperature). The calculations confirm this intuition: O_N^{+1} has a larger ZPE correction and a stronger temperature dependence than Si_{Al}^{+1} . It should be noted that this line of thinking does not apply to the DX configurations, in which the energy landscape around the defect site is

completely different from the host atom site. Both $\text{Si}_{\text{Al-DX}}^{-1}$ configurations are found to have a stronger temperature dependence from vibrational effects than $\text{O}_{\text{N-DX}_a}^{-1}$.

The focus to this point has been on the vibrational influence, and this is because thermal strain affects the $\text{Si}_{\text{Al}}(+|-)$ and $\text{O}_{\text{N}}(+|-)$ DX transitions almost identically. This statement and other general trends will be further discussed in Section 6.3.4.

6.3.2.3 Carbon

Carbon is a common background impurity in AlN. Even in n-type doped AlN, unintentional carbon impurities may be present in concentrations of up to 10^{18}cm^{-3} . [Bry18] Carbon preferentially substitutes on the nitrogen site, and in n-type material forms the deep acceptor C_{N}^{-1} . We also simulated C_{Al} and C_{N} in DX_a and DX_c configurations, but found them to be either unstable or unfavorable at all Fermi levels and realistic chemical potentials; as such, only on-site C_{N} defects are represented on any of the plots.

Figure 6.7 shows the formation energies of carbon point defects at absolute zero, at 0 K with a ZPE correction, and at 300 K and 1400 K, with the same color conventions as in Figures 6.5 and 6.6. Vertical dashed lines represent the VBM at different temperatures, as indicated by the line color. In 6.7(a), only phonon contributions are considered, while in 6.7(b), phonon and thermal strain contributions are both included at finite temperatures. The defects represented include different charge states of on-site C_{N} .

In n-type conditions, the most relevant charge state is C_{N}^{-1} , which is often cited as a possible candidate for an unknown deep acceptor state. [Lam16; Lam17] Knowledge of the energy of the $\text{C}_{\text{N}}(0|-)$ TTL is therefore of significant practical interest for the interpretation of experimental measurements. At 0 K without ZPE, the $\text{C}_{\text{N}}(0|-)$ TTL is calculated to be about 1.83 eV above the VBM, in good agreement with the prediction of 1.88 eV by Lyons *et al.* [Lyo14] When finite-temperature effects are included, the $\text{C}_{\text{N}}(0|-)$ transition level shifts to about 1.80-1.76 eV above the VBM in the range from 0-300 K.

The $\text{C}_{\text{N}}(0|-)$ level shows interesting behavior at finite temperatures. In Figure 6.4, it is apparent that the temperature dependence of $\text{C}_{\text{N}}(0|-)$ closely follows the CBM. At 1400 K, $\text{C}_{\text{N}}(0|-)$ is only 0.25 eV closer to the CBM at 1400 K than at 0 K, and less than 0.09 eV of this variation is due to vibrational contributions. This means that at low temperatures, where thermal strain contributions are negligible, $\text{C}_{\text{N}}(0|-)$ moves almost exactly with the CBM. Therefore, the consequence of this prediction is that measurements of the temperature dependence of $\text{C}_{\text{N}}(0|-)$ relative to the CBM, such as defect-to-band absorption and PL, should

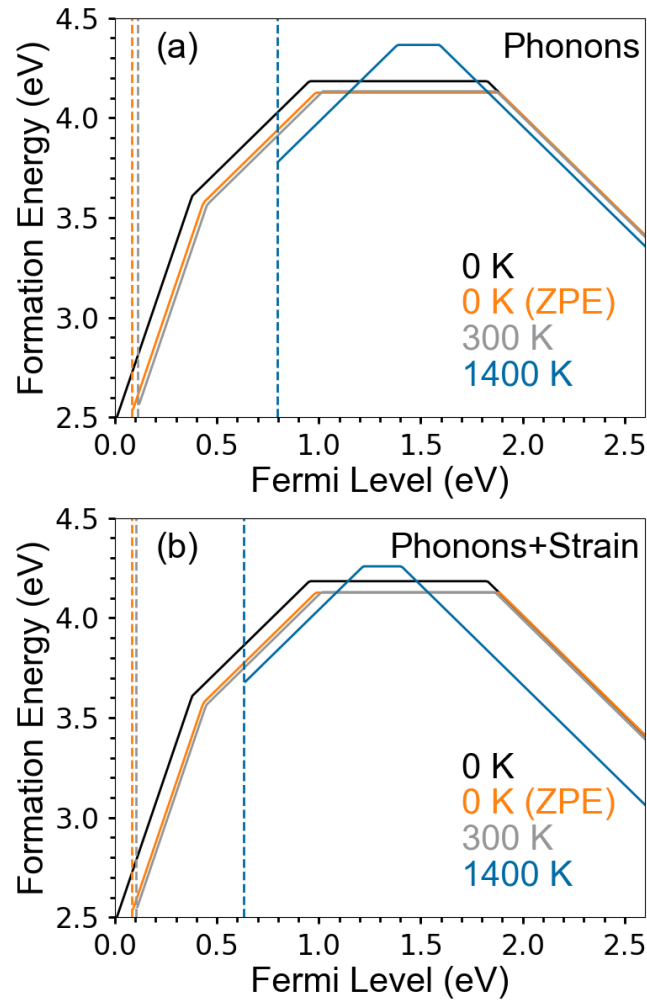


Figure 6.7 Formation energy diagrams for C_N in the vicinity of the VBM at different temperatures with (a) phonon contributions only and (b) phonon and thermal strain contributions. Vertical dashed lines correspond to the VBM at finite temperatures.

be nearly flat up to temperatures of 600 K and then shift slightly at higher temperatures. In addition, it is also worth noting that C_N will act as a deep acceptor in a way predicted by the 0 K formation energy diagrams. While the bandgap contraction needs to be accounted for, the depth of the $C_N(0|-)$ level relative to the CBM is nearly constant, lending credence to interpretation of previous experimental results using 0 K formation energies from the literature.

In a complementary fashion, the ionization energy of $C_N(0|-)$ relative to the VBM decreases rapidly with temperature, as $C_N(0|-)$ decreases and the VBM increases with temperature on an absolute scale. Wickramaratne *et al.* recently computed the temperature dependence of the analogous $C_N(0|-)$ transition level in GaN, and predicted a similar trend relative to the VBM.[Wic18] They account for vibrational contributions to the $C_N(0|-)$ transition, and both vibrational and thermal strain contributions to the VBM. From their calculations, they plot the ionization energy in the temperature range from 0-600 K, showing that $C_N(0|-)$ moves about 0.1 eV closer to the VBM with increasing temperatures in this range. Unfortunately, the calculated temperature dependence of $C_N(0|-)$ and the VBM was not presented separately. However, using methods similar to theirs, we predict the GaN VBM to increase by about 0.035 eV in this same temperature range, which means $C_N(0|-)$ must decrease by about 0.065 eV in GaN (to achieve the total 0.1 eV reduction in the ionization energy). Interestingly, in AlN it is calculated that $C_N(0|-)$ decreases by about 0.066 eV from vibrational contributions in the same temperature range, suggesting that the vibrational behavior of C_N^{-1} and C_N^0 may be very similar in GaN and AlN.

Along with previous DFT studies with HSE functionals, a $C_N(+|0)$ transition is also found within the bandgap.[Lyo14; Gad14; Col12] At 0 K without ZPE, the $C_N(+|0)$ transition is predicted to be about 0.95 eV above the VBM, in good agreement with Lyons *et al.*'s prediction of about 1.07 eV (again, the slight discrepancy can be attributable to different computational settings and finite-size correction schemes).[Lyo14] When finite-temperature effects are included, $C_N(+|0)$ is about 0.90-0.91 eV above the VBM in the temperature range from 0-300 K. Even at higher temperatures, the $C_N(+|0)$ transition tends to follow the VBM as a function of temperature, though not as precisely as the $C_N(0|-)$ transition follows the CBM. Both trends ($C_N(+|0)$ and $C_N(0|-)$) are tied to the temperature dependence of the C_N^0 formation energy, which increases rapidly with temperature from vibrational contributions. This may be observed in Figure 6.7, in which the C_N^0 formation energy is significantly higher at 1400 K (blue line) than at lower temperatures.

A third TTL, $C_N(+2|+)$, is also predicted near the VBM at low temperatures. To our knowledge, $C_N(+2|+)$ has not been predicted in previous computational studies. Experimentally, this state would be difficult to observe, since C_N would not be present in significant concentrations at the relevant Fermi levels. At 0 K without ZPE, it is found that the $C_N(+2|+)$ state is about 0.21 eV above the VBM. When finite-temperature effects are accounted for, the $C_N(+2|+)$ state is about 0.16-0.15 eV above the VBM in the temperature range from 0-300 K. At temperatures above about 780 K, the $C_N(+2|+)$ state moves below the VBM, and the C_N^{+2} charge state is no longer favorable for accessible Fermi levels.

The finite-temperature behavior of C_N also follows some general trends that will be discussed in Section 6.3.4.

6.3.3 Defect Formation Energies: Vacancies

In Sections 6.3.3.1-6.3.3.2, the temperature dependence of the formation energies of vacancy point defects in AlN will be evaluated in detail. The formation energy diagrams presented in this subsection (Figures 6.9 and 6.10) represent formation energies with the same fixed set of native chemical potentials as the formation energy diagrams in Section 6.3.2. As noted before, the chemical potentials are held fixed and are not varied as a function of temperature, in order to isolate the effects of vibrational and thermal strain contributions. For vacancies, chemical potentials may affect the formation energies of v_{Al} relative to v_N , but will not affect the TTLs.

Figure 6.8 is a plot of the band edges and TTLs for v_{Al} (blue) and v_N (red). Figure 6.8 follows the same conventions as Figure 6.4, summarized as follows. The dashed black lines correspond to the VBM and CBM as a function of temperature. The lower and upper boundaries of the plot (at 0 eV and 6.1 eV) correspond to the VBM and CBM at 0 K without ZPR. The solid lines represent vacancy TTLs, as labeled on the plot. For band edges and TTLs, the smooth curves represent phonon contributions only, while the discrete states (horizontal lines) at 300 K and 1400 K include phonon and thermal expansion contributions. The colored notches at 0 K indicate the TTLs without ZPR. In Figure 6.8, all favorable TTLs for vacancies inside the bandgap are plotted, with the associated charge states labeled on the plot. As discussed previously, all TTLs represented on the plot are independent of chemical potentials. For simplicity, the focus is only on vacancy point defects, and we do not discuss defect complexes. In each of the following subsections, the focus will be on a particular vacancy defect, with continual reference to Figure 6.8 for TTL trends.

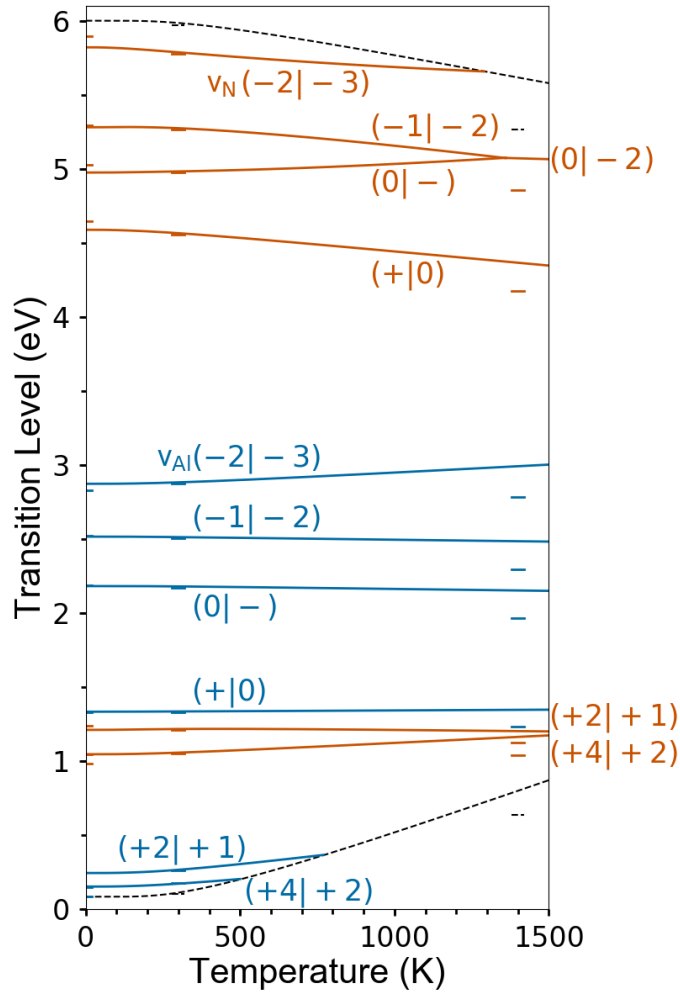


Figure 6.8 Fermi levels corresponding to TTLs for native vacancies (v_{Al} and v_N) in AlN. Band edges are plotted as dotted lines. The smooth curves represent phonon contributions only, while the discrete states at 300 K and 1400 K include phonon and thermal strain contributions. The notches at 0 K represent the transition levels without ZPR. All energies are defined relative to the calculated VBM without ZPR, which we have set to 0 eV.

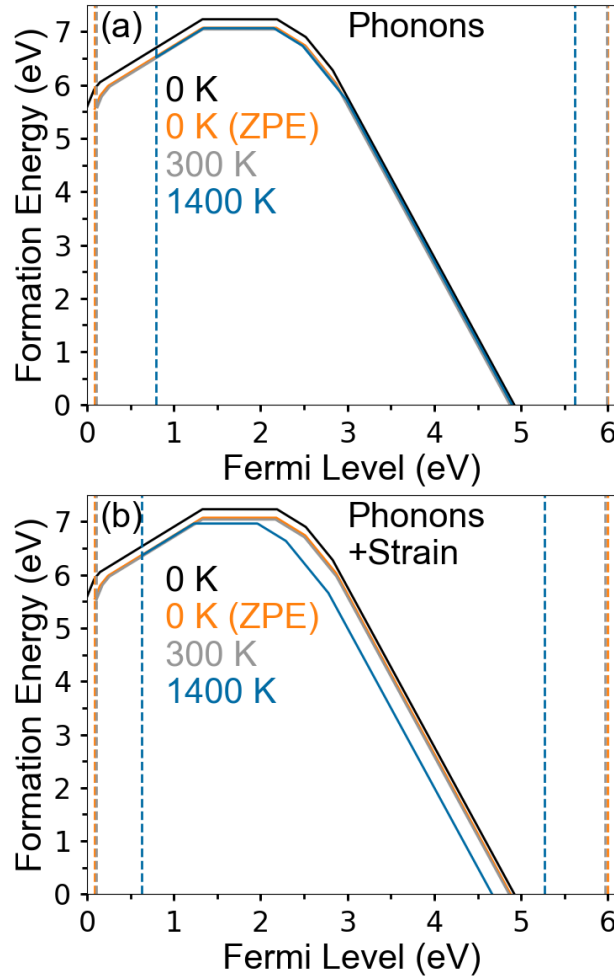


Figure 6.9 Formation energy diagrams for v_{Al} at different temperatures with (a) phonon contributions only and (b) phonon and thermal strain contributions. Vertical dashed lines correspond to the VBM and CBM at finite temperatures.

6.3.3.1 Aluminum Vacancies

Aluminum vacancies are the most ubiquitous intrinsic point defects in n-type AlN. Depending on chemical potentials and impurity concentrations, v_{Al} may form complexes with impurities such as O and Si.[Nam05; Sed12; Ued09; Chi13; Har18] Still, we have predicted elsewhere that isolated v_{Al}^{-3} point defects may be present in significant concentrations in n-type AlN even when defect complexes are accounted for.[Har18] Many experimental studies refer to v_{Al}^{-3} as a candidate deep acceptor for observed donor-acceptor pair transitions.[Nam05; Sed12; Sch11; Lam16; Lam17]

Figure 6.9 shows the formation energies of aluminum vacancies at absolute zero, at 0 K with a vibrational ZPE correction, and at 300 K and 1400 K, with the same color conventions as in Figures 6.5-6.7. Vertical dashed lines represent the VBM and CBM at different temperatures, as indicated by the line color. In 6.9(a), only phonon contributions are considered, while in 6.9(b), phonon and thermal strain contributions are both included at finite temperatures.

Because of the high formation energies at Fermi levels far from the CBM, experimental information about isolated cation vacancies in AlN is limited to the v_{Al}^{-3} deep acceptor and the corresponding $v_{\text{Al}}(-2|-3)$ transition state. From room temperature PL spectra, Nam *et al.* deduce the $v_{\text{Al}}(-2|-3)$ transition level to be about 2.6 eV above the VBM, while Sedhain *et al.* estimate it at about 2.78 eV above the VBM.[Nam05; Sed12] Meanwhile, Bickermann *et al.* observed a room temperature cathodoluminescence (CL) band around 3.3 eV which they ascribe to a transition between $v_{\text{Al}}(-2|-3)$ and either the CBM or an unknown shallow donor.[Bic09] At 300 K with phonon and thermal strain accounted for, we predict $v_{\text{Al}}(-2|-3)$ to be about 2.77 eV above the VBM and 3.10 eV below the CBM, in fairly good agreement with these experimental observations.

We note that our predicted $v_{\text{Al}}(-2|-3)$ level at 0 K without ZPE is about 2.83 eV above the VBM, which differs from an earlier prediction by Yan *et al.* of about 3.11 eV.[Yan14] Since they use the same DFT simulation package (VASP) with similar parameters, the discrepancy is likely attributable to the use of different finite-size correction schemes, which can lead to differences in formation energies on the order of 0.1 eV. Regardless, the phonon contribution to the finite-temperature behavior of $v_{\text{Al}}(-2|-3)$ (including the ZPE correction) is unaffected by the finite-size correction scheme. A finite-size correction is applied to the charged defects in thermally strained supercells, so the thermal strain contribution is sensitive to the finite-size correction scheme.

From Figure 6.8, it can be seen that the phonon and thermal strain contributions to the $v_{\text{Al}}(-2|-3)$ level roughly cancel one another, so that $v_{\text{Al}}(-2|-3)$ remains roughly flat at temperatures from 0-1400 K on an absolute energy scale (it is about 0.09 eV lower at 1400 K than at 0 K). This suggests that the temperature dependence of other energy levels can be approximately determined if they are measured relative to $v_{\text{Al}}(-2|-3)$. For instance, the temperature dependence of band edge-to- $v_{\text{Al}}(-2|-3)$ transitions should approximately follow the temperature dependence of the band edges individually. Likewise, donor-acceptor pair transitions involving $v_{\text{Al}}(-2|-3)$ will approximately follow the temperature dependence of

the donor state.

In Figure 6.8, it can be seen that the $v_{\text{Al}}(-2|-3)$, $v_{\text{Al}}(-|-2)$, and $v_{\text{Al}}(0|-)$ transition states are all clustered within about 1 eV of each other, with the $v_{\text{Al}}(+|0)$ state nearly 1 eV below these. Although they do not report exact numbers, Yan *et al.* predict the same cluster of states within about 1 eV of one another, with the $v_{\text{Al}}(+|0)$ state about 1 eV below them.[Yan14] In addition, two states are found near the VBM, $v_{\text{Al}}(+2|+)$ and $v_{\text{Al}}(+4|+2)$, which were not predicted by Yan *et al.* (v_{Al}^{+3} is not favorable at any Fermi level). Both of these states curve slightly with the VBM as a function of temperature, but pass below the VBM at high temperatures. However, it is notoriously difficult to push the Fermi level close to the VBM in AlN; and even then, v_{Al} has very high formation energies at Fermi levels near the VBM. Thus, $v_{\text{Al}}(+2|+)$ and $v_{\text{Al}}(+4|+2)$ would be difficult to observe experimentally (although not impossible in non-equilibrium conditions).

The finite-temperature behavior of v_{Al} also follows some general trends which will be discussed in Section 6.3.4.

6.3.3.2 Nitrogen Vacancies

Nitrogen vacancies are most favorable when the Fermi level is below midgap. While true p-type character has been difficult to achieve, the nitrogen vacancy was found as the major compensator to the carbon acceptor in physical vapor transport grown AlN.[Gad13] Other experimental studies have managed to probe the properties of v_{N} by non-equilibrium techniques, such as ion implantation[Nep04] or x-ray irradiation[Sol11b; Sol11a]. There has also been recent interest in v_{N} and v_{N} -transition metal complexes as single-spin centers which may be useful as optically addressable qubits.[Var16; Seo16]

Figure 6.10 shows the formation energies of nitrogen vacancies at absolute zero, at 0 K with a vibrational ZPE correction, and at 300 K and 1400 K, with the same color conventions as in Figures 6.5-6.9. Vertical dashed lines represent the VBM and CBM at different temperatures, as indicated by the line color. In 6.10(a), only phonon contributions are considered, while in 6.10(b), phonon and thermal strain contributions are both included at finite temperatures.

From PL peaks in cobalt-implanted AlN, Nepal *et al.* deduce an energy level about 0.26 eV below the CBM at low temperatures, which they associate with nitrogen vacancies induced by the ion implantation.[Nep04] Their conclusion is consistent with the $v_{\text{N}}(-2|-3)$ level, which is predicted to be about 0.18-0.20 eV below the CBM in the temperature range

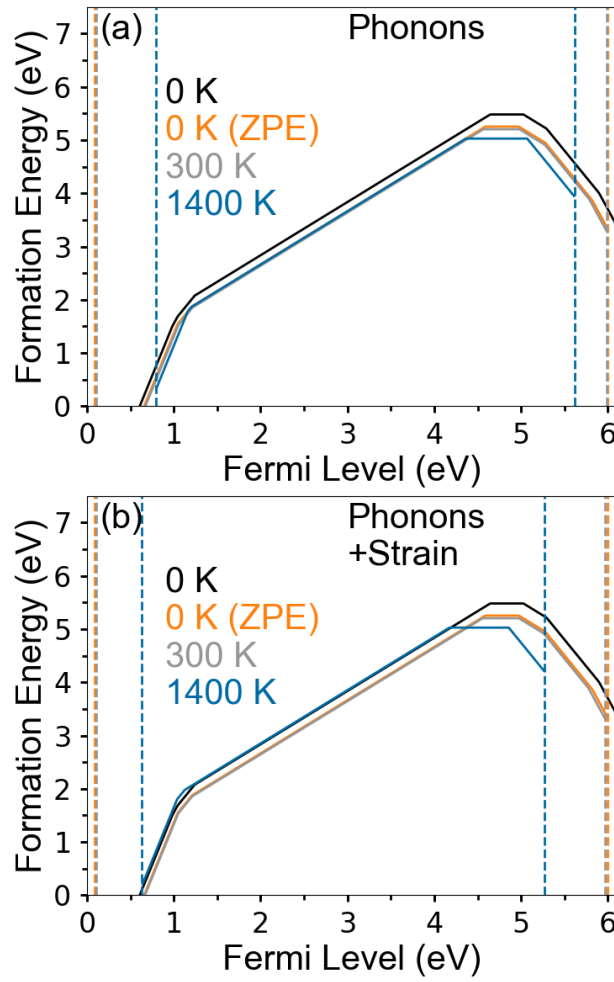


Figure 6.10 Formation energy diagrams for v_N at different temperatures with (a) phonon contributions only and (b) phonon and thermal strain contributions. Vertical dashed lines correspond to the VBM and CBM at finite temperatures.

from 0-300 K when phonon and thermal strain effects are included.

Soltamov *et al.* used thermoluminescence to deduce electron trap states in AlN after x-ray irradiation at 77 K and 300 K.[Sol11a] After low-temperature irradiation, they calculate an activation energy of about 0.32 eV, which may arise from the combined influence of multiple trap states, as they note. It is plausible that the $v_N(-2|-3)$ level may contribute to their observed activation energy. After high-temperature irradiation, they calculate an activation energy of about 0.75 eV, which they explicitly associate with nitrogen vacancies, owing to a suppression of other thermoluminescence bands. This is consistent with the $v_N(-1|-2)$ level, which we predict to be about 0.72-0.71 eV below the CBM in the temperature range from 0-300 K when phonon and thermal strain effects are included.

Using DFT simulations with hybrid functionals, Varley *et al.* predict the $v_N(0|-)$ and $v_N(-1|-2)$ transition levels to be 0.95 eV and 0.62 eV below the CBM, respectively.[Var16] Their predictions are slightly lower than our predicted values of 1.08 eV and 0.81 eV below the CBM for the same respective transitions at 0 K without ZPE. Again, we attribute the discrepancy to the use of different finite-size correction schemes. Although no other v_N transition levels are reported explicitly by other DFT studies using hybrid functionals, our formation energy plots at 0 K without ZPE roughly agree with those found in Varley *et al.* and Yan *et al.*, with two exceptions: we predict a v_N^{+4} charge state at Fermi levels near the VBM, which makes the v_N^{+3} charge state unfavorable at any Fermi level; and we predict a v_N^{-3} charge state at Fermi levels near the CBM.[Var16; Yan14]

Two interesting phenomena are observed when finite-temperature effects are included. First, when looking at Figure 6.8, it is obvious that the $v_N(0|-2)$ transition level becomes favorable at temperatures above about 1350 K, at the expense of the $v_N(0|-1)$ and $v_N(-1|-2)$ transitions. This happens because the v_N^{-1} charge state becomes unfavorable at all Fermi levels at high temperatures, as can be observed in Figure 6.10. Second, a favorable v_N^{+3} charge state is predicted within a narrow range of Fermi levels (about 0.06 eV wide) at 0 K without ZPE. However, when phonon effects are included, the v_N^{+3} charge state becomes unfavorable at all Fermi levels, even at 0 K. This highlights the potential importance of vibration in the determination of levels at 0 K.

General trends in the finite-temperature behavior of v_N , along with the rest of the point defects studied here, will be discussed in Section 6.3.4.

6.3.4 Defect Formation Energies: General Trends

In Figures 6.4 and 6.8, several trends may be observed that are common to all or many of the defects studied here. The trends in the ZPE shift of the transition levels at 0 K, as well as trends in the phonon and thermal strain contributions to the transition levels at finite temperatures, will be discussed separately in this section.

In Figures 6.4 and 6.8, the discrete notches at 0 K represent transition levels at 0 K without a ZPE correction. Thus, the ZPE shift of a given transition level can be read from the plot by comparing the notch with the continuous curve of the corresponding color at 0 K. It is found that the ZPE correction tends to shift transition states near the VBM to higher energies (the same direction as the VBM), while transition states near the CBM tend to shift to lower energies (the same direction as the CBM). For a given defect, the magnitude of the ZPE shift of its formation energy turns out to be minimal in its formal charge state (the charge state where the defect has the same number of valence electrons as the host atom, i.e. $\text{Si}_{\text{Al}}^{+1}$, O_{N}^{+1} , C_{N}^{-1} , $\text{v}_{\text{Al}}^{-3}$, and v_{N}^{+3}). For instance, the magnitude of the ZPE shift is smaller for C_{N}^{-1} than for any other charge state of C_{N} . Moreover, the ZPE shift tends to increase in magnitude as the charge state of the defect gets farther from its formal charge state. In effect, this makes the ZPE shift positive for transition levels involving charge states higher than the defect's formal charge, and negative for transition levels lower than the formal charge. Since higher charge states are favorable near the VBM and lower charge states are favorable near the CBM, states near the VBM tend to have a positive ZPE shift while states near the CBM tend to have a negative ZPE shift.

In general, vibrational contributions cause transition levels at finite temperatures to trend in the same direction as the ZPE shift, with the exception of $\text{C}_{\text{N}}(0|-)$ and $\text{v}_{\text{N}}(0|-)$. These exceptions are caused by an unusually strong temperature dependence of the free energy of formation of the neutral charge states C_{N}^0 and v_{N}^0 . This behavior is ultimately related to the distribution of vibrational mode energies of the defect, which results from the difference between phonon energy distributions computed for the defect and bulk supercells. If the vibrational energies of a given defect follow a tight distribution, the free energy of formation will generally be monotonic with increasing temperature and in the same direction as the ZPE shift. However, for defects with a broad phonon distribution, the formation energy is not necessarily monotonic with temperature, and may trend in the opposite direction from the ZPE at high temperatures.

A general trend in the influence of thermal strain on the transition levels is also readily

apparent in Figures 6.4 and 6.8. Thermal strain tends to shift all energy levels, including the band edges, to lower energies on an absolute scale. Moreover, the magnitude of the shift of the transition level due to thermal strain is roughly a function of the position of the state within the bandgap. That is, thermal strain causes states near the VBM to shift down by approximately the same amount as the VBM, and states closer to the CBM shift down by an amount similar to the CBM. The origin of this is that thermal strain causes the formation energy of a given defect to shift down by a magnitude which increases monotonically as the charge state of the defect decreases. This is perhaps a confinement effect: increasing the crystal volume reduces the formation energy of a given defect by effectively increasing the volume within which electrons are localized around the defect site; the more electrons, the greater the reduction in formation energy relative to the unstrained system. At any rate, this general trend in the influence of thermal strain has an important implication for finite-temperature simulations. Although thermal strain reduces all energy levels on an absolute scale, it has a minimal influence on the energies of defect transition levels *relative to the nearest band edge*. This implies that the influence of vibrational contributions may be sufficient for determining the temperature dependence of defect states relative to the band edges (though not on an absolute scale). On the other hand, one must be careful to treat the band edges and the defects with the same level of detail: if thermal strain contributions are not accounted for in the defect levels, they should not be included in the temperature dependence of the band edges either, even if that leads to an incorrect description of the temperature dependence of the overall bandgap.

6.4 Conclusions

Defect formation energies are routinely computed using bulk and defect simulations at absolute zero. These 0 K formation energies are then used to draw conclusions about finite-temperature systems and processes, such as doping in semiconductors. We have demonstrated that vibrational and thermal strain contributions can have an impact on defect formation energies and transition levels.

For instance, we predict that the $\text{Si}_{\text{Al}}(+|-)$ DX transition levels shift above the CBM at doping temperatures, suggesting that any presence of $\text{Si}_{\text{Al}}(+|-)$ DX states at low temperatures must result from low-temperature re-equilibration. We also predict that the temperature dependence of the $\text{C}_{\text{N}}(0|-)$ state closely follows the temperature dependence of the CBM,

so that transitions observed between $C_N(0|-)$ and the CBM should appear nearly independent of temperature. Similarly, $C_N(+|0)$ shifts approximately with the VBM as a function of temperature. The reason for the difference in the bending of the $(0|-)$ and $(+|0)$ charge states for C_N stems back to vibrational mode differences of the neutral state with those of the neighboring charge states.

In general, ZPE corrections shift TTLs to lower energies for states near the CBM, and higher energies for states near the VBM. At finite temperatures, vibrational contributions tend to shift states near the band edges in the same direction as the band edges, though not necessarily with the same magnitudes. On an absolute scale, deep defect levels are sometimes relatively flat as a function of temperature, but not necessarily so. In fact, the temperature dependence of a particular defect state does not always follow from intuitive ideas, and may be difficult to predict without explicit simulation (or experimental observation).

Thermal strain contributions tend to shift all states (including the band edges) to lower energies with increasing temperature. Because of this general trend, thermal strain has only a minimal effect on the energies of transition levels *relative to the nearest band edge*, although the shift on an absolute scale is significant at high temperatures. This means that thermal strain could probably be neglected for simulations concerned with the energies of transition levels relative to the band edges, so long as the band edges are treated in the same way.

All in all, we predict that vibrational and thermal strain contributions can have an impact on defect formation energies and transition levels at finite temperatures (and a small impact even at 0 K, because of ZPE corrections). In some cases, our finite-temperature calculations have revealed interesting physics at elevated temperatures which would have been difficult to predict without explicit simulation. Nevertheless, we stress that this does not invalidate most conclusions drawn from ground state DFT studies, but does provide an avenue to probe finite-temperature observations with theoretical models.

6.5 Acknowledgements

The authors acknowledge financial support from the AFOSR grant FA9550-17-1-0225, and computer time from the DoD HPCMP. Preston Bowes was supported by the Department of Defense through the National Defense Science and Engineering Graduate Fellowship

program. Professor Ramón Collazo of North Carolina State University and Dr. Pramod Reddy of Adroit Materials are thanked for their comments and discussion on the paper.

CHAPTER

7

CONCLUSIONS AND FUTURE WORK

The work in this dissertation has furthered the understanding of the behavior of point defects in AlN and Al-rich AlGaN. In three separate studies, the following conclusions have been reached:

(1) From modeling Si and O point defects in a pseudorandom $\text{Al}_{0.65}\text{Ga}_{0.35}\text{N}$ alloy, a strong dependence of the defect formation energies on the chemistry of first-nearest neighbors was revealed. The detailed behavior of this local chemistry dependence was explained by appealing to a relatively simple bonding picture. It was also demonstrated that O_N defects in $\text{Al}_{0.65}\text{Ga}_{0.35}\text{N}$ should be associated with multiple thermodynamic transition levels, a conclusion which could not be reached by interpolating between the results of simulations in the end members GaN and AlN.

(2) A mechanistic picture of the manner in which the formation of $\text{V}_\text{Al} + n\text{Si}_\text{Al}$ complexes leads to the Si-compensation knee in AlN was developed. In low-Si doping conditions, the Si_Al^{+1} donor is the dominant Si-containing defect, so that free carrier concentration increases with Si concentration. However, in high-Si doping conditions, the $\text{V}_\text{Al} + n\text{Si}_\text{Al}$ (acceptor and neutral) complexes with $n > 1$ become more favorable due to the higher Si

chemical potential, so that free carrier concentration decreases with Si concentration. This mechanistic model was validated by the results of a numerical charge balance solver, which qualitatively reproduced the compensation knee when $V_{\text{Al}} + n\text{Si}_{\text{Al}}$ complexes were included (whether or not C and O background impurities were included). In addition, predicted optical emissions for defects present in low-Si and high-Si doping conditions agreed well with photoluminescence measurements from samples doping in corresponding conditions.

(3) Finite-temperature properties of Si, O, and C impurities as well as Al and N vacancies were computed from the results of phonon simulations and static thermal strain simulations. It was demonstrated that vibrational and thermal strain contributions can have an impact on defect formation energies and transition levels. In general, zero-point energy (ZPE) corrections were found to shift thermodynamic transitions levels (TTLs) and DX transition levels in the same direction as the nearest band edge (to lower energies for states near the CBM, and to higher energies for states near the VBM). At finite temperatures, vibrational contributions were found to have a tendency to shift states near a band edge in the same direction as that band edge, though not necessarily with the same magnitudes. Some deep defect levels were found to have very little temperature dependence on an absolute scale, while some were found to move similar to one of the band edges. In particular, the temperature dependence of the $C_{\text{N}}(0|-)$ level is very similar to that of the CBM. Thermal strain was found to shift all states (including the band edges) to lower energies with increasing temperature. As a result, thermal strain has only a small impact on the energies of transition levels relative to the nearest band edge, although it has a more significant impact on an absolute energy scale.

Each of these studies is a potentially fruitful branching point for future investigations. Modeling defects in alloys from first principles is a challenging but intriguing area of study which still holds many open avenues for research. In AlGaN in particular, point defects and complexes may be simulated in a range of compositions between GaN and AlN, in order to determine the influence of composition on point defect properties. Another important area of focus for future research is the extension of the results of ground-state simulations to finite temperatures. DFT can be used to calculate the temperature dependence of electronic band structures (including the VBM, CBM and bandgap), and some avenues to this are currently being explored. In addition, temperature-dependent formation energies may be incorporated in to the charge-balance defect solver, in order to make high-temperature doping simulations more quantitative. This approach will be used to extend the analysis

of the Si-compensation knee in AlN. Finite-temperature effects can also be incorporated into simulations based on the Franck-Condon principle. This can be used for predictions of optical emission bands (corresponding to photoluminescence intensity distributions) rather than just discrete optical emission energies, as well as the temperature dependence of optical emissions. New approaches to the finite-size correction for charged defects in periodic supercells have also been explored. Finally, a number of powerful software tool sets have been developed, and large data sets have been developed for AlN and AlGaN as a part of this research. For the bulk, these data sets include electronic structure calculations, phonon calculations, strained bulk calculations, simulations with different AlGaN alloy configurations, and simulations with different functionals and other convergence criteria. For the defects, hundreds of different charge states and configurations have been simulated, each with HSE and PBE total energies (including two sets in thermally strained cells at 300 K and 1400 K), HSE simulations of Franck-Condon optical transitions, and PBE phonon distributions. It is the author's expectation that these tools and data sets will be useful to many future researchers interested in nitride materials, point defects, and DFT simulations in general.

BIBLIOGRAPHY

- [AMN03] Al-Mushadani, O. K. & Needs, R. J. “Free-energy calculations of intrinsic point defects in silicon”. *Physical Review B* **68**.23 (2003), p. 235205.
- [Ald18] Alden, D et al. “Point-Defect Nature of the Ultraviolet Absorption Band in AlN”. *Physical Review Applied* **9**.5 (2018), p. 054036.
- [Ald16] Alden, D. et al. “On the origin of the 4.7 eV absorption and 2.8 eV emission bands in bulk AlN substrates”. *ECS Transactions* **72**.5 (2016), pp. 31–40.
- [Bak18a] Baker, J. N. “Point defects in strontium and barium titanate from first principles: Properties and thermodynamics”. PhD thesis. North Carolina State University, 2018.
- [Bak17] Baker, J. N. et al. “Defect mechanisms of coloration in Fe-doped SrTiO₃ from first principles”. *Applied Physics Letters* **110**.12 (2017), p. 122903.
- [Bak18b] Baker, J. N. et al. “Mechanisms governing metal vacancy formation in BaTiO₃ and SrTiO₃”. *Journal of Applied Physics* **124**.11 (2018), p. 114101.
- [Bak18c] Baker, J. N. et al. “Mechanisms governing metal vacancy formation in BaTiO₃ and SrTiO₃”. *Journal of Applied Physics* **124**.11 (2018), p. 114101.
- [Bak19] Baker, J. N. et al. “An Informatics Software Stack for Point Defect-Derived Opto-Electronic Properties: The Asphalt Project”. *arXiv e-prints* (2019). arXiv: 1906.02776.
- [BJI73] Barker Jr, A. & Ilegems, M. “Infrared lattice vibrations and free-electron dispersion in GaN”. *Physical Review B* **7**.2 (1973), p. 743.
- [Bar01] Baroni, S. et al. “Phonons and related crystal properties from density-functional perturbation theory”. *Reviews of Modern Physics* **73**.2 (2001), p. 515.
- [Bic05] Bickermann, M et al. “Orientation-dependent phonon observation in single-crystalline aluminum nitride”. *Applied Physics Letters* **86**.13 (2005), p. 131904.
- [Bic09] Bickermann, M. et al. “Point defect content and optical transitions in bulk aluminum nitride crystals”. *Physica Status Solidi B* **246**.6 (2009), pp. 1181–1183.
- [Bic10] Bickermann, M. et al. “Deep-UV transparent bulk single-crystalline AlN substrates”. *Physica Status Solidi C* **7**.7-8 (2010), pp. 1743–1745.

- [BB97] Bogusławski, P & Bernholc, J. “Doping properties of C, Si, and Ge impurities in GaN and AlN”. *Physical Review B* **56.15** (1997), p. 9496.
- [Bow18a] Bowes, P. C. et al. “Influence of impurities on the high temperature conductivity of SrTiO₃”. *Applied Physics Letters* **112.2** (2018), p. 022902.
- [Bow18b] Bowes, P. C. et al. “Influence of impurities on the high temperature conductivity of SrTiO₃ Influence of impurities on the high temperature conductivity of SrTiO₃”. *Applied Physics Letters* **112.2** (2018), p. 022902.
- [Bry15] Bryan, I. “Al-rich AlGa_N and AlN growth on bulk AlN single crystal substrates”. PhD thesis. North Carolina State University, 2015.
- [Bry18] Bryan, I. et al. “Doping and compensation in Al-rich AlGa_N grown on single crystal AlN and sapphire by MOCVD”. *Applied Physics Letters* **112.6** (2018), p. 062102.
- [Bry14] Bryan, Z. et al. “Fermi level control of compensating point defects during metalorganic chemical vapor deposition growth of Si-doped AlGa_N”. *Applied Physics Letters* **105.22** (2014), p. 222101.
- [BW13] Burke, K. & Wagner, L. O. “DFT in a nutshell”. *International Journal of Quantum Chemistry* **113.2** (2013), pp. 96–101.
- [Cap06] Capelle, K. “A bird’s-eye view of density-functional theory”. *Brazilian Journal of Physics* **36.4A** (2006), pp. 1318–1343.
- [CJ86] Chase Jr., M. W. et al. *NIST Standard Reference Database 13*. U.S. Department of Commerce, 1986.
- [Chi13] Chichibu, S. et al. “Impacts of Si-doping and resultant cation vacancy formation on the luminescence dynamics for the near-band-edge emission of Al_{0.6}Ga_{0.4}N films grown on AlN templates by metalorganic vapor phase epitaxy”. *Journal of Applied Physics* **113.21** (2013), p. 213506.
- [Col11] Collazo, R. et al. “Progress on n-type doping of AlGa_N alloys on AlN single crystal substrates for UV optoelectronic applications”. *Physica Status Solidi C* **8.7-8** (2011), pp. 2031–2033.
- [Col12] Collazo, R. et al. “On the origin of the 265 nm absorption band in AlN bulk crystals”. *Applied Physics Letters* **100.19** (2012), p. 191914.

- [Col67] Collins, A. et al. "Lattice vibration spectra of aluminum nitride". *Physical Review* **158.3** (1967), p. 833.
- [Dal11] Dalmau, R et al. "Growth and characterization of AlN and AlGaN epitaxial films on AlN single crystal substrates". *Journal of The Electrochemical Society* **158.5** (2011), H530–H535.
- [Dar70] Darwent, B. d. *Bond Dissociation Energies in Simple Molecules*. Gaithersburg, MD, USA: National Bureau of Standards NSRDS, 1970.
- [DK04] Dubay, O & Kresse, G. "Erratum: Accurate density functional calculations for the phonon dispersion relations of graphite layer and carbon nanotubes [Phys. Rev. B 67, 035401 (2003)]". *Physical Review B* **69.8** (2004), p. 089906.
- [DK03] Dubay, O. & Kresse, G. "Accurate density functional calculations for the phonon dispersion relations of graphite layer and carbon nanotubes". *Physical Review B* **67.3** (2003), p. 035401.
- [Dyc15] Dycus, J. H. et al. "Accurate nanoscale crystallography in real-space using scanning transmission electron microscopy". *Microscopy and Microanalysis* **21.4** (2015), pp. 946–952.
- [Dyc18] Dycus, J. H. et al. "Structure of Ultrathin Native Oxides on III–Nitride Surfaces". *ACS Applied Materials & Interfaces* **10.13** (2018), pp. 10607–10611.
- [Est09] Estreicher, S. K. et al. "Vibrational properties of impurities in semiconductors". *Modelling and Simulation in Materials Science and Engineering* **17.8** (2009), p. 084006.
- [Fig09] Figge, S. et al. "Temperature dependence of the thermal expansion of AlN". *Applied Physics Letters* **94.10** (2009), p. 101915.
- [Fio03] Fiolhais, C. et al. *A primer in density functional theory*. Vol. 620. Springer Science & Business Media, 2003.
- [Fre14] Freysoldt, C. et al. "First-principles calculations for point defects in solids". *Reviews of Modern Physics* **86.1** (2014), p. 253.
- [Fu15] Fu, J. Q. et al. "First-principle studies of phonons and thermal properties of AlN in wurtzite structure". *Journal of Physics: Conference Series*. Vol. 574. 1. IOP Publishing. 2015, p. 012046.

- [Gad13] Gaddy, B. E. et al. “Vacancy compensation and related donor-acceptor pair recombination in bulk AlN”. *Applied Physics Letters* **103**.16 (2013), p. 161901.
- [Gad14] Gaddy, B. E. et al. “The role of the carbon-silicon complex in eliminating deep ultraviolet absorption in AlN”. *Applied Physics Letters* **104**.20 (2014), p. 202106.
- [Gle14] Glensk, A. et al. “Breakdown of the Arrhenius law in describing vacancy formation energies: The importance of local anharmonicity revealed by ab initio thermodynamics”. *Physical Review X* **4**.1 (2014), p. 011018.
- [Goe01] Goennenwein, S. et al. “Generation–recombination noise of DX centers in AlN: Si”. *Applied Physics Letters* **79**.15 (2001), pp. 2396–2398.
- [Gor14] Gordon, L et al. “Hybrid functional calculations of DX centers in AlN and GaN”. *Physical Review B* **89**.8 (2014), p. 085204.
- [Göt96] Götz, W et al. “Activation energies of Si donors in GaN”. *Applied Physics Letters* **68**.22 (1996), pp. 3144–3146.
- [Gra11a] Grabowski, B et al. “Temperature-driven phase transitions from first principles including all relevant excitations: The fcc-to-bcc transition in Ca”. *Physical Review B* **84**.21 (2011), p. 214107.
- [Gra07] Grabowski, B. et al. “Ab initio study of the thermodynamic properties of non-magnetic elementary fcc metals: Exchange-correlation-related error bars and chemical trends”. *Physical Review B* **76**.2 (2007), p. 024309.
- [Gra09] Grabowski, B. et al. “Ab initio up to the melting point: Anharmonicity and vacancies in aluminum”. *Physical Review B* **79**.13 (2009), p. 134106.
- [Gra11b] Grabowski, B. et al. “Formation energies of point defects at finite temperatures”. *Physica Status Solidi B* **248**.6 (2011), pp. 1295–1308.
- [Gra11c] Grandusky, J. R. et al. “High output power from 260 nm pseudomorphic ultraviolet light-emitting diodes with improved thermal performance”. *Applied Physics Express* **4**.8 (2011), p. 082101.
- [HB13] Han, P. & Bester, G. “Large nuclear zero-point motion effect in semiconductor nanoclusters”. *Physical Review B* **88**.16 (2013), p. 165311.
- [Har18] Harris, J. S. et al. “On compensation in Si-doped AlN”. *Applied Physics Letters* **112**.15 (2018), p. 152101.

- [Har19] Harris, J. S. et al. “Oxygen and silicon point defects in Al_{0.65}Ga_{0.35}N”. *Physical Review Materials* **3.5** (2019), p. 054604.
- [Hey03] Heyd, J. et al. “Hybrid functionals based on a screened Coulomb potential”. *The Journal of Chemical Physics* **118.18** (2003), pp. 8207–8215.
- [Hey06] Heyd, J. et al. “Erratum: Hybrid functionals based on a screened Coulomb potential [J. Chem. Phys. 118, 8207 (2003)]”. *The Journal of Chemical Physics* **124.21** (2006), p. 219906.
- [HK64] Hohenberg, P. & Kohn, W. “Inhomogeneous electron gas”. *Physical review* **136.3B** (1964), B864.
- [Jon68] Jones, J. B. “Al–O and Si–O tetrahedral distances in aluminosilicate framework structures”. *Acta Crystallographica Section B* **24.3** (1968), pp. 355–358.
- [Jon15] Jones, K. et al. “AlGaN devices and growth of device structures”. *Journal of Materials Science* **50.9** (2015), pp. 3267–3307.
- [KS65] Kohn, W. & Sham, L. J. “Self-consistent equations including exchange and correlation effects”. *Physical review* **140.4A** (1965), A1133.
- [KH94] Kresse, G & Hafner, J. “Ab initio molecular-dynamics simulation of the liquid-metal–amorphous-semiconductor transition in germanium”. *Physical Review B* **49.20** (1994), p. 14251.
- [KF96a] Kresse, G. & Furthmüller, J. “Efficiency of ab-initio total energy calculations for metals and semiconductors using a plane-wave basis set”. *Computational Materials Science* **6.1** (1996), pp. 15–50.
- [KF96b] Kresse, G. & Furthmüller, J. “Efficient iterative schemes for ab initio total-energy calculations using a plane-wave basis set”. *Physical Review B* **54.16** (1996), p. 11169.
- [KH93] Kresse, G. & Hafner, J. “Ab initio molecular dynamics for liquid metals”. *Physical Review B* **47.1** (1993), p. 558.
- [KO14] Kumagai, Y. & Oba, F. “Electrostatics-based finite-size corrections for first-principles point defect calculations”. *Physical Review B* **89.19** (2014), p. 195205.
- [Lam16] Lamprecht, M et al. “Very slow decay of a defect related emission band at 2.4 eV in AlN: Signatures of the Si related shallow DX state”. *Journal of Applied Physics* **119.15** (2016), p. 155701.

- [Lam17] Lamprecht, M. et al. “Slow decay of a defect-related emission band at 2.05 eV in AlN: Signatures of oxygen-related DX states”. *Physica Status Solidi B* **254.5** (2017), p. 1600338.
- [Lan79] Lang, D. et al. “Trapping characteristics and a donor-complex (DX) model for the persistent-photoconductivity trapping center in Te-doped Al_xGa_{1-x}As”. *Physical Review B* **19.2** (1979), p. 1015.
- [Lev01] Levinshtein, M. E. et al. *Properties of Advanced Semiconductor Materials: GaN, AlN, InN, BN, SiC, SiGe*. Hoboken, NJ, USA: John Wiley & Sons, 2001.
- [Loo95] Loong, C.-K. “The Phonon Densities of States of AlN and ZrN”. *MRS Online Proceedings Library Archive* **395** (1995).
- [LS09] Lucas, G & Schäublin, R. “Vibrational contributions to the stability of point defects in bcc iron: A first-principles study”. *Nuclear Instruments and Methods in Physics Research Section B: Beam Interactions with Materials and Atoms* **267.18** (2009), pp. 3009–3012.
- [Lyo10] Lyons, J. L. et al. “Carbon impurities and the yellow luminescence in GaN”. *Applied Physics Letters* **97.15** (2010), p. 152108.
- [Lyo14] Lyons, J. L. et al. “Effects of carbon on the electrical and optical properties of InN, GaN, and AlN”. *Physical Review B* **89.3** (2014), p. 035204.
- [Mas99] Mason, P. M. et al. “Optically detected electron paramagnetic resonance of AlN single crystals”. *Physical Review B* **59.3** (1999), p. 1937.
- [MN97] Mattila, T & Nieminen, R. M. “Point-defect complexes and broadband luminescence in GaN and AlN”. *Physical Review B* **55.15** (1997), p. 9571.
- [McC98] McCluskey, M. et al. “Metastability of oxygen donors in AlGaN”. *Physical Review Letters* **80.18** (1998), p. 4008.
- [McC99] McCluskey, M. et al. “DX centers in AlGaN”. *International Journal of Modern Physics B* **13.11** (1999), pp. 1363–1378.
- [Meh13] Mehnke, F. et al. “Highly conductive n-Al_xGa_{1-x}N layers with aluminum mole fractions above 80%”. *Applied Physics Letters* **103.21** (2013), p. 212109.
- [MI11] Momma, K. & Izumi, F. “VESTA 3 for three-dimensional visualization of crystal, volumetric and morphology data”. *Journal of Applied Crystallography* **44.6** (2011), pp. 1272–1276.

- [Mor86] Morgan, T. N. “Theory of the DX center in $\text{Al}_x\text{Ga}_{1-x}\text{As}$ and GaAs crystals”. *Physical Review B* **34.4** (1986), p. 2664.
- [Nam04] Nam, K. B. et al. “Optical properties of AlN and GaN in elevated temperatures”. *Applied Physics Letters* **85.16** (2004), pp. 3489–3491.
- [Nam05] Nam, K. B. et al. “Deep impurity transitions involving cation vacancies and complexes in AlGaN alloys”. *Applied Physics Letters* **86.22** (2005), p. 222108.
- [Nep04] Nepal, N et al. “Optical properties of the nitrogen vacancy in AlN epilayers”. *Applied Physics Letters* **84.7** (2004), pp. 1090–1092.
- [PC97] Park, C. & Chadi, D. “Stability of deep donor and acceptor centers in GaN, AlN, and BN”. *Physical Review B* **55.19** (1997), p. 12995.
- [PR10] Perdew, J. P. & Ruzsinszky, A. “Fourteen easy lessons in density functional theory”. *International Journal of Quantum Chemistry* **110.15** (2010), pp. 2801–2807.
- [Per96] Perdew, J. P. et al. “Generalized gradient approximation made simple”. *Physical review letters* **77.18** (1996), p. 3865.
- [Per93] Perlin, P. et al. “Raman-scattering studies of aluminum nitride at high pressure”. *Physical Review B* **47.5** (1993), p. 2874.
- [Pol98] Polyakov, A. et al. “Properties of Si donors and persistent photoconductivity in AlGaN”. *Solid-State Electronics* **42.4** (1998), pp. 627–635.
- [Red16] Reddy, P et al. “Point defect reduction in wide bandgap semiconductors by defect quasi Fermi level control”. *Journal of Applied Physics* **120.18** (2016), p. 185704.
- [Red17] Reddy, P. et al. “Point defect reduction in MOCVD (Al) GaN by chemical potential control and a comprehensive model of C incorporation in GaN”. *Journal of Applied Physics* **122.24** (2017), p. 245702.
- [Ric10] Rice, A et al. “Surface preparation and homoepitaxial deposition of AlN on (0001)-oriented AlN substrates by metalorganic chemical vapor deposition”. *Journal of Applied Physics* **108** (2010), p. 043510.
- [Sac15] Sachet, E. et al. “Dysprosium-doped cadmium oxide as a gateway material for mid-infrared plasmonics”. *Nature Materials* **14.4** (2015), pp. 414–420.

- [Sch11] Schulz, T et al. “Ultraviolet luminescence in AlN”. *Physica Status Solidi B* **248.6** (2011), pp. 1513–1518.
- [Sed12] Sedhain, A et al. “Nature of optical transitions involving cation vacancies and complexes in AlN and AlGaN”. *Applied Physics Letters* **100.22** (2012), p. 221107.
- [Seo16] Seo, H. et al. “Design of defect spins in piezoelectric aluminum nitride for solid-state hybrid quantum technologies”. *Scientific Reports* **6** (2016), p. 20803.
- [Shi11] Shimahara, Y. et al. “Growth of high-quality Si-doped AlGaN by low-pressure metalorganic vapor phase epitaxy”. *Japanese Journal of Applied Physics* **50.9R** (2011), p. 095502.
- [Shu16] Shulumba, N. et al. “Impact of anharmonic effects on the phase stability, thermal transport, and electronic properties of AlN”. *Physical Review B* **94.10** (2016), p. 104305.
- [Sie06] Siegel, A et al. “Ab initio calculation of structural phase transitions in AlN crystal”. *Physical Review B* **74.10** (2006), p. 104116.
- [Sil11] Silvestri, L. et al. “Hybrid functional study of Si and O donors in wurtzite AlN”. *Applied Physics Letters* **99.12** (2011), p. 122109.
- [Sil12] Silvestri, L. et al. “Concentration of point defects in wurtzite AlN: A hybrid functional study”. *Europhysics Letters* **98.3** (2012), p. 36003.
- [Ski99] Skierbiszewski, C et al. “Evidence for localized Si-donor state and its metastable properties in AlGaN”. *Applied Physics Letters* **74.25** (1999), pp. 3833–3835.
- [Sol11a] Soltamov, V. A. et al. “Identification of nitrogen vacancies in an AlN single crystal: EPR and thermoluminescence investigations”. *Physics of the Solid State* **53.6** (2011), pp. 1186–1190.
- [Sol10] Soltamov, V. et al. “Identification of the deep level defects in AlN single crystals by electron paramagnetic resonance”. *Journal of Applied Physics* **107.11** (2010), p. 113515.
- [Sol11b] Soltamov, V. et al. “Identification of the deep-level defects in AlN single crystals: EPR and TL studies”. *Diamond and Related Materials* **20.7** (2011), pp. 1085–1089.
- [Son11] Son, N. et al. “Shallow donor and DX states of Si in AlN”. *Applied Physics Letters* **98.9** (2011), p. 092104.

- [SW02] Stampfl, C & Walle, C. G. Van de. “Theoretical investigation of native defects, impurities, and complexes in aluminum nitride”. *Physical Review B* **65**.15 (2002), p. 155212.
- [SW98] Stampfl, C & Walle, C. G. Van de. “Doping of Al_xGa_{1-x}N”. *Applied Physics Letters* **72**.4 (1998), pp. 459–461.
- [Sta99] Stampfl, C. et al. “Doping of Al_xGa_{1-x}N alloys”. *Materials Science and Engineering B* **59**.1 (1999), pp. 253–257.
- [Tan02] Taniyasu, Y. et al. “Intentional control of n-type conduction for Si-doped AlN and Al_xGa_{1-x}N (0.42 ≤ x < 1)”. *Applied Physics Letters* **81**.7 (2002), pp. 1255–1257.
- [Tia17] Tian, L.-Y. et al. “Alloying effect on the elastic properties of refractory high-entropy alloys”. *Materials & Design* **114** (2017), pp. 243–252.
- [Tsa17] Tsao, J. Y. et al. “Ultrawide-bandgap semiconductors: Research opportunities and challenges”. *Advanced Electronic Materials* **4**.1 (2017), p. 1600501.
- [Tsa18] Tsao, J. Y. et al. “Ultrawide-Bandgap Semiconductors : Research Opportunities and Challenges”. *Advanced Electronic Materials* **4** (2018), p. 1600501.
- [Ued09] Uedono, A et al. “Vacancy-oxygen complexes and their optical properties in AlN epitaxial films studied by positron annihilation”. *Journal of Applied Physics* **105**.5 (2009), p. 054501.
- [Ued12] Uedono, A et al. “Native cation vacancies in Si-doped AlGa_N studied by monoenergetic positron beams”. *Journal of Applied Physics* **111**.1 (2012), p. 013512.
- [Var16] Varley, J. B. et al. “Defects in AlN as candidates for solid-state qubits”. *Physical Review B* **93**.16 (2016), p. 161201.
- [Wag03] Wagener, M. et al. “Intrinsic compensation of silicon-doped AlGa_N”. *Applied Physics Letters* **83**.20 (2003), pp. 4193–4195.
- [Wal98a] Walle, C. G. Van de. “DX-center formation in wurtzite and zinc-blende Al_xGa_{1-x}N”. *Physical Review B* **57**.4 (1998), R2033.
- [WN04] Walle, C. G. Van de & Neugebauer, J. “First-principles calculations for defects and impurities: Applications to III-nitrides”. *Journal of Applied Physics* **95**.8 (2004), pp. 3851–3879.

- [Wal98b] Walle, C. G. Van de et al. “Theory of doping and defects in III–V nitrides”. *Journal of Crystal Growth* **189** (1998), pp. 505–510.
- [Wic18] Wickramaratne, D. et al. “Defect identification based on first-principles calculations for deep level transient spectroscopy”. *Applied Physics Letters* **113**.19 (2018), p. 192106.
- [Xie13] Xie, J. et al. “Lasing and longitudinal cavity modes in photo-pumped deep ultraviolet AlGa_N heterostructures”. *Applied Physics Letters* **102**.17 (2013), p. 171102.
- [XC93] Xu, Y.-N. & Ching, W. “Electronic, optical, and structural properties of some wurtzite crystals”. *Physical Review B* **48**.7 (1993), p. 4335.
- [Yan14] Yan, Q. et al. “Origins of optical absorption and emission lines in AlN”. *Applied Physics Letters* **105**.11 (2014), p. 111104.
- [Zei00] Zeisel, R et al. “DX-behavior of Si in AlN”. *Physical Review B* **61**.24 (2000), R16283.
- [Zha18] Zhang, X. et al. “Calculating free energies of point defects from ab initio”. *Computational Materials Science* **148** (2018), pp. 249–259.

APPENDIX

APPENDIX

A

SUPPLEMENTAL MATERIAL

A.1 Supplement for Chapter 5

Table A.1 is a list of all defects simulated for the study presented in Chapter 5, the number of unique configurations simulated (not including degenerate configurations), and the number of charge states simulated. This list comprises all starting geometries we explored. The appearance of a given defect on this list does not mean it is stable, and in some cases the starting geometry relaxed into another geometry (e.g. an unstable DX configuration may relax back to an on-site geometry). Unstable geometries are nonetheless included in Table A.1 for the sake of completion. All stable and metastable defects listed in Table A.1 were included in the charge balance doping simulations, even if they did not contribute significantly to the physics (i.e. if their formation energies were prohibitively high).

Table A.1 List of simulated defects, the number of unique configurations simulated (does not include degenerate configurations), and the range of charge states simulated for the study in Chapter 5. The subscript indicates the site on which the defect substitutes, and the suffix -DX appearing in the subscript indicates an off-site (DX) configuration.

Defect	Config	Charge	Defect	Config	Charge	Defect	Config	Charge
Al_N	1	-4..4	$\text{Si}_{\text{Al-DX}}$	3	-2..2	$\text{V}_{\text{Al}} + 2\text{O}_\text{N}$	2	-3..3
C_{Al}	1	-4..4	Si_N	1	-4..4	$\text{V}_{\text{Al}} + 3\text{O}_\text{N}$	2	-3..3
$\text{C}_{\text{Al-DX}}$	2	-2..2	$\text{Si}_{\text{N-DX}}$	2	-2..2	$\text{V}_{\text{Al}} + 4\text{O}_\text{N}$	2	-3..3
C_N	1	-4..4	V_{Al}	1	-4..4	$\text{V}_{\text{Al}} + \text{C}_\text{N}$	2	-3..3
$\text{C}_{\text{N-DX}}$	2	-2..2	V_N	1	-4..4	$\text{V}_{\text{Al}} + \text{Si}_{\text{Al}}$	3	-2..1
N_{Al}	1	-4..4	$\text{C}_\text{N} + \text{C}_{\text{Al}}$	2	-3..3	$\text{V}_{\text{Al}} + 2\text{Si}_{\text{Al}}$	13	-1..2
O_{Al}	1	-4..4	$\text{O}_\text{N} + \text{O}_{\text{N-DX}}$	1	-1..1	$\text{V}_{\text{Al}} + 3\text{Si}_{\text{Al}}$	42	0..3
$\text{O}_{\text{Al-DX}}$	2	-2..2	$\text{Si}_{\text{Al}} + \text{C}_\text{N}$	2	-3..3	$\text{V}_{\text{Al}} + \text{V}_\text{N}$	2	-3..3
O_N	1	-4..4	$\text{Si}_{\text{Al}} + \text{O}_\text{N}$	2	-3..3	$\text{V}_\text{N} + \text{C}_\text{N}$	3	-2..2
$\text{O}_{\text{N-DX}}$	2	-2..2	$\text{Si}_{\text{Al}} + \text{V}_\text{N}$	2	-3..3			
Si_{Al}	1	-4..4	$\text{V}_{\text{Al}} + \text{O}_\text{N}$	2	-3..3			